# New Frontiers for Perovskite Solar Cells: From Adhesion to Interfacial Fracture and Processing Effects on Device Performances

*Reisya Ichwani*

A Dissertation
Submitted to the Faculty
of the
WORCESTER POLYTECHNIC INSTITUTE
in partial fulfillment of the requirements for the
Degree of Doctor of Philosophy
in
Mechanical & Materials Engineering
May 2022

APPROVED:

_____

Prof. Winston Soboyejo, Primary Advisor, Senior Vice President, Provost and Professor of Mechanical & Materials Engineering, WPI

_____

Prof. Brajendra Mishra, Program Director of Materials and Manufacturing Engineering, WPI

_____

Prof. Danielle Lynn Cote, Professor of Mechanical & Materials Engineering, WPI

_____

Prof. Lyubov Titova, Professor of Physics, WPI

_____

Prof. Oluwaseun Kehinde Oyewole, Professor of Mechanical & Materials Engineering, WPI

# Abstract

Perovskites are promising alternative materials to the silicon counterparts for making solar cells. Photovoltaic community has been focused on improving the power conversion efficiency and stability of perovskite solar cells (PSCs) over a decade. On the way from lab to market, highly efficient and stable of perovskite solar cells is not enough for PSCs to be realized. Reliability and scalability are important factors to be improved to bring a mature technology to the market. Interfaces of PSCs multilayer stack are one of problematic issues that can reduce the performance and durability of PSCs. The interfacial reliability of PSCs will be discussed with the results of adhesion interactions in nanoscale and interfacial fracture toughness in macroscale, and its associated toughening mechanisms as the effect of different processing of perovskite active layers.

In terms of scalability, PSCs have potentials to be commercially grown using spray fabrication method that involves various parameters: nozzle speed, head-substrate spacing distance, substrate temperature, and applied pressure after spraying to produce a compact structure of perovskite active layer. Those various parameters are suitable for a data science framework for enabling process optimization with purpose of PSCs manufacturing with shorter timescale and lower experimental cost that was previously made. The results of optimization of spray-deposited perovskites conditions, interfacial properties, and toughening mechanism at interfaces of perovskite and charge transport layers, as well as machine learning model development of spray parameters optimization will be discussed as they relate to spray-assisted PSCs performances.

# Dedication

*To Adri Huda,*

*for your endless pray, love, understanding, and support*

*To Aidan Abdurrahman Huda,*

*for your smile*

# Acknowledgments

I would like to first say Alhamdulillah to Allah for his countless blessings.

I would like to express my special gratitude to my advisor, Prof. Wole Soboyejo, for his guidance and encouragement, over the past four years throughout my graduate school. His academic and moral motivations have contributed tremendously to the completion of this dissertation. I would also like to extend my gratitude for the committee members: Prof. Danielle Cote, Prof. Lyubov Titova, Prof. Brajendra Mishra, Dr. Oluwaseun Kehinde Oyewole for your time to provide suggestion and recommendation throughout the dissertation.

I would also like to acknowledge Professor Richard Sisson and Professor Terri Camesano for their guidance in pursuing academic goal in early time in WPI, Professor Shivkumar for his support during my time as a teaching assistant, Professor Pratap Rao for his support during my early research in solar cells, and Professor Ronald Grimm for some discussions and characterizations. I am also grateful to Professor Rodica Neamtu and her student, Stephen, in Data Science Program for guiding me in an independent study to apply a machine learning approach to perovskite processing problems. I would also like to acknowledge Professor Jing Du in Penn State University for some technical discussions on adhesion work.

My sincere gratitude also goes to my current and previous teammates: Tofunmi Ogunfunmi, Jaya Cromwell, Ridwan Ahmed, Vanessa Uzonwanne, Dr. Deborah Oyewole, Dr. Richard Koech, Trevor Bond, and Yusuf Olannrewaju, for advice and discussions in various technical problems and data analysis. I would also like to thank professors in our research group- Dr.

Oluwaseun Kehinde Oyewole, Dr. John Obayemi, and Dr. Ali Salifu for their supports in many aspects of the work.

I would like to appreciate the support I received from my sponsors- Fulbright scholarship and fellowships from WPI for funding that support years of my journey in US.

I would like to express the deepest gratitude to my family. Mama, Papa, Atok, Bunda, and my siblings you have provided all support, encouragement, and interest in my dissertation work. Thanks for listening to my problems and providing perspectives. Finally, I would like to thank my husband Adri. He has been continually supportive in this journey. He is my best friend, my most enthusiastic cheerleader, an amazing husband, and a best father for my son. Thank you for believing in me when I doubted myself.

# Table of Contents

# List of Figures

# List of Tables

# Chapter 1

# Introduction

### 1.1 Motivation and Unresolved Issues

#### 1.1.1 Global Energy Demand

The energy consumption worldwide is anticipated to increase to 25 TW by 2040. Increasing the population and the industrial growth has contributed to this increment in energy demand. All different countries strategize different plans, policies, and controls to provide accessible energies that are sufficient for people which is one the most casual issues of the 21$^{st}$ century [1]. The dependency on fossil fuel is also a huge challenge as the fossil fuels deplete over time and the environmental impacts caused by the fossil fuel exploitation [2]. This has stimulated efforts in research, development and commercialization of technology that can utilize renewable and eco-friendly energies such as solar, wind, biomass, geothermal and hydropower to compete with fossil fuels [3].

Solar is the most abundant energy source in universe. It provides approximately 1.7 x $10^5$ TW of energy reaching the surface of earth each second. If only 600 TW of this solar energy is practically harvestable at around 10% efficiency, this could provide 60 TW of energy that can be used to provide more than enough energy to meet global energy needs with no cost [4]. Solar energy is also not exhaustible as it produces solid and increasing output efficiencies compared to the other energy sources as long as the area have good solar radiation [5]. It is obviously seen in Figure 1-1 that a three-quarter of the world has sufficient intensity of solar intensity. Moreover, as an affordable and applicable energy sources, solar systems can be effectively utilized for many sectors such as villages, industrial operations,

and homes [6]. This suggests that a sustained effort on solar energy research could pave the way to a renewable energy future in which solar energy could address many of the global energy needs.

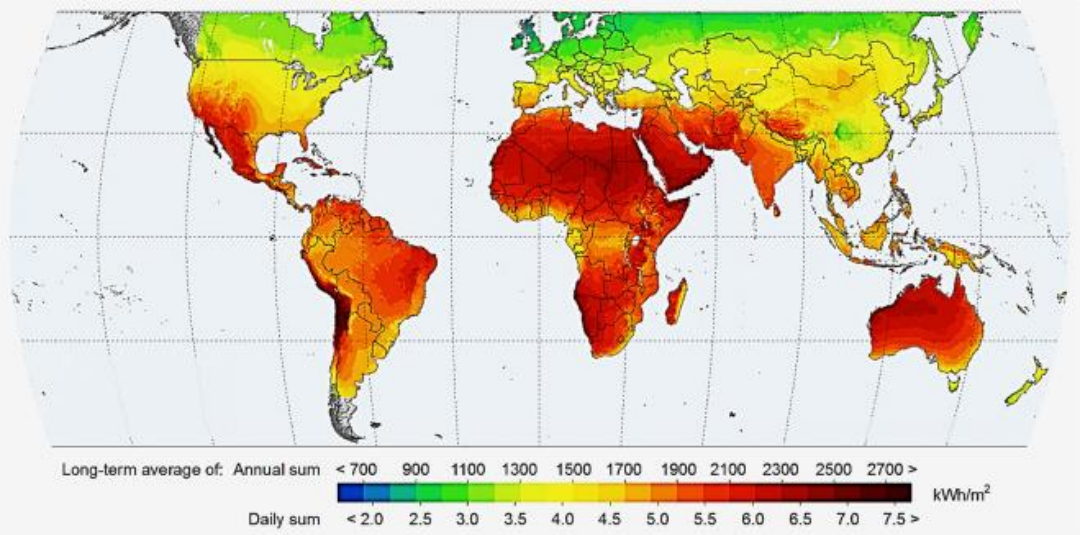


Figure 1-1 Global horizontal irradiation maps, Adapted from Ref [1]

### 1.1.2 Reliability of Multilayer Electronic Devices

Electronic devices such as solar cells [7], batteries [8], micro-electro-mechanical system (MEMS) micro-switches [9], and printed circuit boards consist of sophisticated stacks of different functional materials in their structures. Features such as thermal expansion mismatch of materials and weakly bonded interfaces often induces deformation or delamination in the device structures, impacting the viability and long term-processability of the technologies [10]. Other stresses such as deformation-induced by in-service thermal excursions for those devices operating various weather conditions, fractures during manufacturing, installation, maintenance, and services, an additional stress of stretchable and flexible technology also impact the reliability of the multilayer devices, attracting the

manufacturer's concerns [11]. The mechanisms related to the failure of multilayer electronic devices must be understood towards their commercialization.

Some of observed deformations caused by build-up stresses in multilayer electronic devices are shown in Figure 1-2. In energy harvesting devices, silicon solar cells often have an encapsulant as a protection layer. Delamination could occur around the interconnect ribbons and metallization during services with high possibility of current leakage and fluxing cycle issue (Figure 1-2 (a)) [12]. Delamination failures was also observed on the silicon PV modules during service. The infrared thermal images of minimodules that experienced corrosion, bubbles, and delamination under thermal cycles are shown in Figure 1-2 (b).

In the next generation of perovskite solar cells (PSCs), stress at interfaces can be developed between bulk absorber layer and the adjacent transporting layer during thermal cycling. The delamination (Figure 1-2 (c)) between absorber layer to the neighboring transport layers can induce a barrier of electron/hole transfer to the electrode. Furthermore, robust and reliable flexible transparent electrode materials have been actively reported, to realize PSCs with balanced excellency in mechanical flexibility and high efficiency. Additional stresses from high bending cycles produces linear cracks on the metal electrodes due to the weak adhesion between graphene and the metal surfaces illustrated in Figure 1-2 (d)). Moreover, the deformation-induced stresses are also observed in solid-state lithium-ion batteries due to the intensive volumetric expansion during operation. Solid electrolyte in the structures is required to resist diffusion of Li dendrites during ion transports, resulting a build-up stress towards an interfacial cracking and a catastrophic short-circuit failure in the structures (Figure 1-2 (e)).

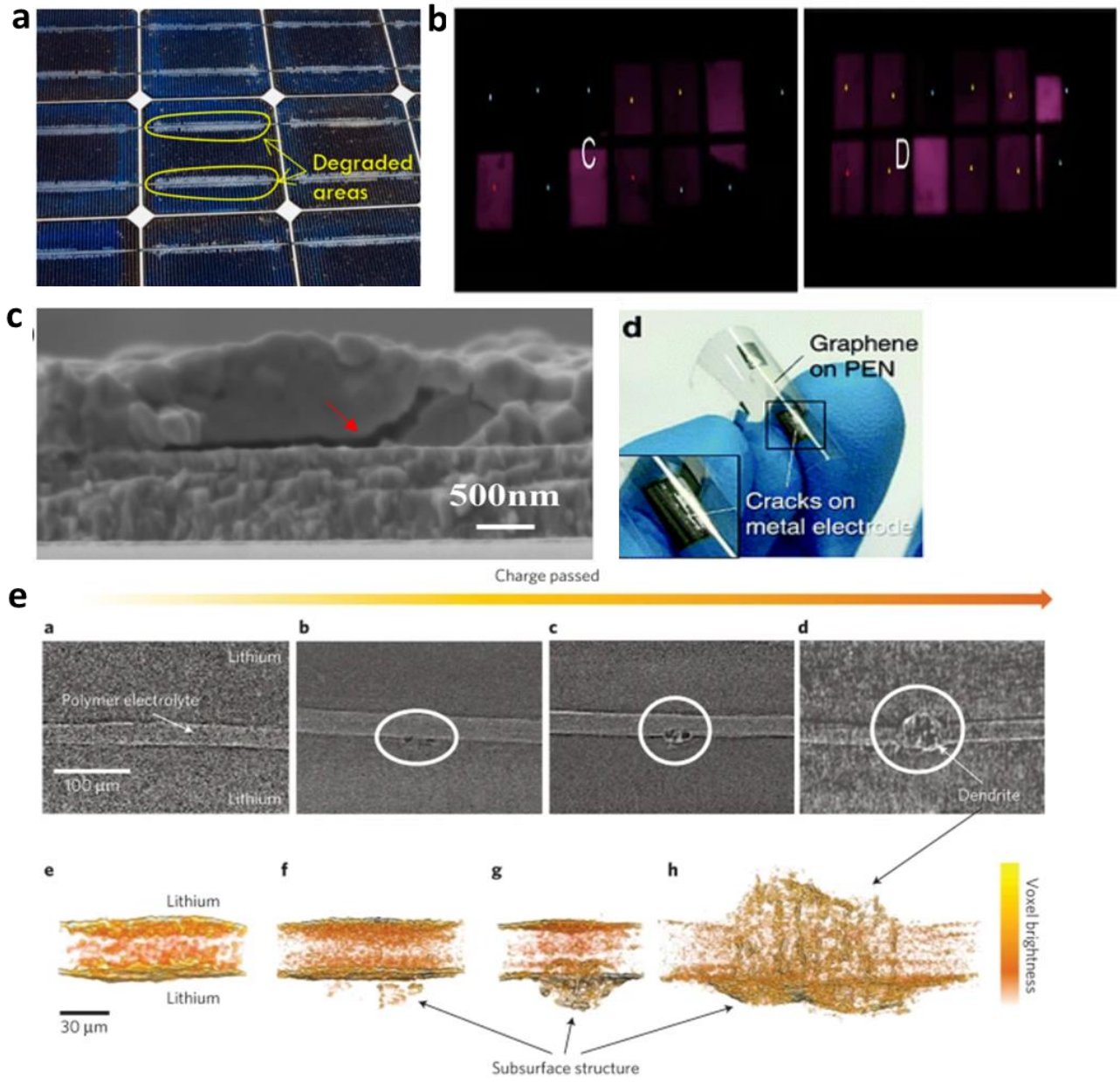


Figure 1-2 The deformation phenomena from in electronic devices: (a) Delamination between silicon solar cells and the encapsulants. Adapted from Ref. [12], (b) Failures in silicon minimodules. Adapted from Ref [13], (c) Layer detachment in perovskite solar cells, Adapted from Ref [14]. (d) cracks generated during bending in flexible solar cells, Adapted from Ref [15]. and (e) Evolution of dendritic deformation in multilayer stack lithium batteries, Adapted from Ref [16].

Determination of adhesion and fracture energy, $G_c$, in multilayer devices is perhaps the most crucial indicator to evaluate the weakest interface in the systems that can link to the mechanical reliability of electronic devices. Particularly in PSCs, an understanding of devices stability, scalability and reliability together is very crucial to have an efficient operation of PCSs. To date, most of PSC research has focused on pursuing efficiency increases and prolonged stability period, but PSCs will also need to mechanically reliable to efficiently operate under harsh condition of air and sun exposure. Thus, a critical need exists for better understanding of the interfacial adhesion and the fracture toughness to elucidate the reliability of multilayer stack of perovskite solar cells.

### 1.1.3 Scalability of Solar Cells Technologies

Perovskite materials are potential to be absorbers in the next-generation solar cells due to their excellent intrinsic electro-optical properties, namely broad optical absorption coefficients [17,18], long electron-hole diffusion lengths [17-19], high charge carrier mobilities [20,21], and low-cost solution processable costs [22,23]. The combination works on the structural design, material chemistry, process engineering and device physics contributes to the fast evolution in PSCs performances [24]. Improvement in PSCs performances has been progressively made starting from 3.8% of photoconversion efficiencies (PCEs) in 2009 [25], to above 25.1% in 2020 [26], which is a game-changer in a photovoltaic performance race.

Solution processability of PSCs at low temperature has been an attractive feature of PSC photovoltaic (PV) technology. It enables devices to be fabricated quickly with cheaper cost unlike the traditional silicon PV devices. However, challenges for transitioning from the laboratory scale to the factory scale of PSCs are remained. Developing scalable deposition technologies for the uniform coating, achieving better control of film formation across the device stack at large scale, and understanding the impact of device architectures on the reliability, stability and performances of perovskites modules, are factors that would need to

be addressed towards PSC commercialization [27]. Currently, spin-coating is the widely used solution-based method to develop lab-scale PSCs. While this method can produce high efficiency of devices, spin-coating technique suffers from low nonuniformity in thickness, poor reproducibility, and small coating area [28,29].

A remarkable progress on large-scale fabrication technique has been rapidly seen over years in Figure 1-3 (a), showing that there is an improvement over years in the PSCs performances with the area increasing. The plot shows PSCs with small-area cells (~0.1 $cm^2$), large-area cells (~1 $cm^2$) and modules (>10 $cm^2$). However, losses in efficiency are inevitable as the area increases for most types of solar cells (Figure 1-3 (b)), because of non-uniform coating over large area, higher series resistance, the presence of dead area of interconnections and bus bars, and so on. PSCs performances are notably lag behind those other solar cells when the device area increases [27]. This suggests that the existing efforts in scaling up the solution-based PSCs needs to be thoroughly investigated from the microstructures, processability and interfacial reliability to limit the losses of their efficiency over areas.

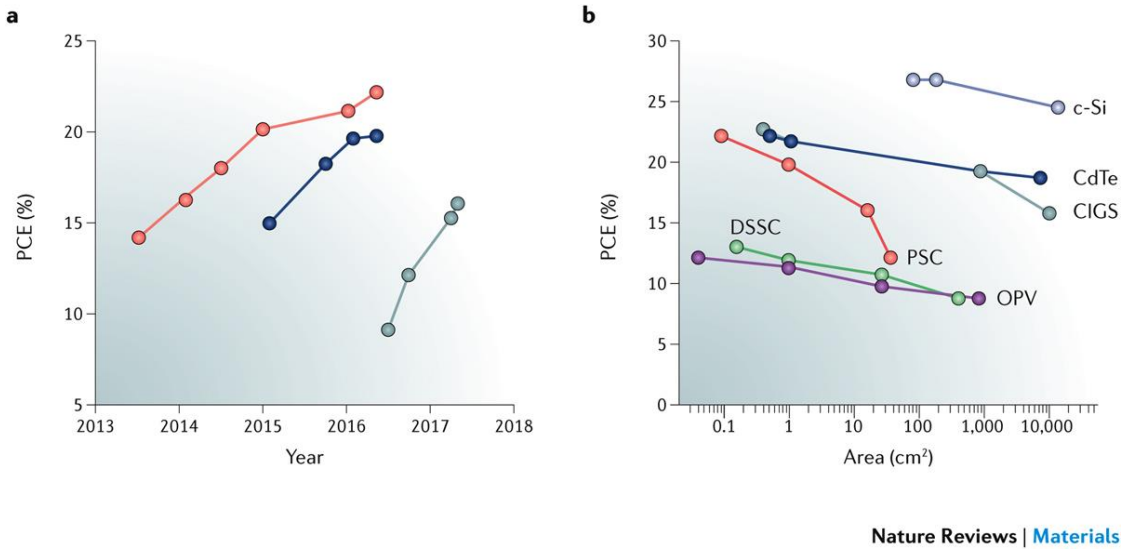


Figure 1-3 The improvements of the photoconversion efficiency (PCE) of PSCs in few years for small-area cells (orange), large-area cells (blue) and modules (grey)(a). The plot between PCE and the areas for different types of solar cells, including crystalline silicone (c-Si),

cadmium telluride (CdTe), copper indium gallium selenide (CIGS, dye-sensitized solar cells (DSSC), organic photovoltaic (OPV). Adapted from Ref [27].

### 1.2 Research Objectives

The objectives of this work are:

(i) To study the mechanical reliability of multilayer stack perovskite solar cells at different processing, including solution (spin-coating, spray-coating) and vapor deposition.

(ii) To elucidate the toughening mechanisms at interfaces of perovskite solar cells

(iii) To optimize the scalable spray fabrication technique of perovskite solar cells

(iv) To develop machine learning guided framework in finding the optimum configurations of spray deposition technique for shorter timescale and cheaper experimental budget.

### 1.3 Scope of the Dissertation

A brief description of the preceding chapter of this dissertation is given below:

Chapter 2 will provide the background information of the progress in PSCs developments. First, the photovoltaic technology is briefly reviewed. Second, the PSCs are introduced including the physics behind the operating principles and the efficiency measurement in solar cells. Third, the mechanical testing adopted in this study is explained including adhesion and interfacial fracture toughness in multilayer stack electronic structures. Finally, the scalable processing in PSCs technology is introduced, and spray coating for scalable option for PSCs manufacturing are contrasted to other methods, and machine learning for spray process optimization in photovoltaic area is also reviewed.

Chapter 3 and 4 will provide the reliability aspect of PSCs. Chapter 3 will include the nanoscale study of adhesion between layers in the multilayer stack PSCs using atomic force microscopy technique. This study includes the correlation of interfacial adhesions, perovskite fabrication method, and the charge carrier dynamics in PSCs. The results will be

useful in designing PSCs, not only for yielding high photovoltaic performances, but also for having high interfacial reliability of multilayer structures. The resulted adhesions are then ranked, and these rankings are crucial in the selection of appropriate functional layers and processing techniques for the fabrication of layers in PSCs.

After the study of interfacial interactions in nanoscale, Chapter 4 will subsequently capture the interfacial micro-scale examination through a fracture test called *Brazilian disk* test that is allow us to quantify the interfacial fracture energy between bi-materials in vapor and solution-processed PSCs with different loading conditions. The combination of processing and microstructure of PSCs will also relate to engineer the solar cell performances. The fracture energy is also predicted using theoretical zone model and compare it to the experimental results. The toughening mechanism that contributes to the crack-tip shielding is also characterized. The measured interfacial fracture energies will also provide useful measurements that can be incorporated into simulations of crack growth along the interfaces of model PSCs structures.

Chapter 5 and 6 will provide an insight of scalability of PSCs. Chapter 5 will optimize the perovskite fabrication using spray coating. Some parameters of spray systems such as substrate temperature, automated nozzle speed and height between spray and substrate, are selected to search the optimum conditions of perovskite absorber layers. This study will also explore the interfacial reliability of perovskites and the neighboring transport layers and compare those interfaces integrity to the widely used spin coating processes. The effects of external applied pressure after spraying will also be discussed to further optimize the spray-assisted PSCs.

Chapter 6 will describe the machine learning approach to identify the hidden relationships and analyze the impact on the efficiency of the solar cells of functional parameters such as temperature, speed, distance of the nozzle, and pressure added after spraying. Two regression model- multivariate linear and polynomial regression will be compared. This study will offer an insight of the use of machine learning techniques,

allowing us to collect a much-reduced dataset that can be augmented to provide insights and generalize the relationship between functional parameters and PSCs efficiency. The optimization of the resulted model will provide a guidance in a new design of experiment (DOE) for future experiments.

**References**


[1] Kannan, N.; Vakeesan, D. Solar Energy for Future World: - A Review. *Renew. Sustain. Energy Rev.* **2016**, *62*, 1092–1105. https://doi.org/10.1016/j.rser.2016.05.022.

[2] US Energy Information Administration. International Energy Outlook 2017 https://www.eia.gov/outlooks/ieo/.

[3] Lau, K. K. S.; Soroush, M. *Overview of Dye-Sensitized Solar Cells*; Elsevier Inc., 2019. https://doi.org/10.1016/B978-0-12-814541-8.00001-X.

[4] Hagfeldt, A., Boschloo, G., Sun, L., Kloo, L. and Pettersson, H. Dye-Sensitized Solar Cells. *Chem. Rev.* **2010**, 6595–6663. https://doi.org/http://dx.doi.org/10.1021/cr900356p.

[5] Nozik, A. J. Photoelectrochemistry: Applications to Solar Energy Conversion. *Annu. Rev. Phys. Chem.* **1978**, *29* (1), 189–222. https://doi.org/10.1146/annurev.pc.29.100178.001201.

[6] Schlamadinger, B.; Apps, M.; Bohlin, F.; Gustavsson, L.; Jungmeier, G.; Marland, G.; Pingoud, K.; Savolainen, I. Towards a Standard Methodology for Greenhouse Gas Balances of Bioenergy Systems in Comparison with Fossil Energy Systems. *Biomass and Bioenergy* **1997**, *13* (6), 359–375. https://doi.org/10.1016/S0961-9534(97)10032-0.

[7] Modi, M. B.; Sitaraman, S. K. Interfacial Fracture Toughness Measurement for Thin Film Interfaces. *Eng. Fract. Mech.* **2004**, *71* (9–10), 1219–1234. https://doi.org/10.1016/S0013-7944(03)00210-8.

[8] Ahmed, R. A.; Ebechidi, N.; Reisya, I.; Orisekeh, K.; Huda, A.; Bello, A.; Oyewole, O. K.; Soboyejo, W. O. Pressure-Induced Interfacial Contacts and the Deformation in All Solid-State Li-Ion Batteries. *J. Power Sources* **2022**, *521*, 230939. https://doi.org/10.1016/j.jpowsour.2021.230939.

[9] Cao, Y.; Nankivil, D. D.; Allameh, S.; Soboyejo, W. O. Mechanical Properties of Au Films on Silicon Substrates. *Mater. Manuf. Process.* **2007**, *22* (2), 187–194. https://doi.org/10.1080/10426910601062271.

[10] De Bastiani, M.; Armaroli, G.; Jalmood, R.; Ferlauto, L.; Li, X.; Tao, R.; Harrison, G. T.;

Eswaran, M. K.; Azmi, R.; Babics, M.; Subbiah, A. S.; Aydin, E.; Allen, T. G.; Combe, C.; Cramer, T.; Baran, D.; Schwingenschlögl, U.; Lubineau, G.; Cavalcoli, D.; De Wolf, S. Mechanical Reliability of Fullerene/Tin Oxide Interfaces in Monolithic Perovskite/Silicon Tandem Cells. *ACS Energy Lett.* **2022**, *7* (2), 827–833. https://doi.org/10.1021/acsenergylett.1c02148.

[11] Dai, Z.; Yadavalli, S. K.; Chen, M.; Abbaspourtamijani, A.; Qi, Y.; Padture, N. P. Interfacial Toughening with Self-Assembled Monolayers Enhances Perovskite Solar Cell Reliability. *Science (80-. ).* **2021**, *372* (6542), 618–622. https://doi.org/10.1126/science.abf5602.

[12] Hasan, A. A. Q.; Ahmed Alkahtani, A.; Shahahmadi, S. A.; Nur E. Alam, M.; Islam, M. A.; Amin, N. Delamination-and Electromigration-Related Failures in Solar Panels—A Review. *Sustainability* **2021**, *13* (12), 6882. https://doi.org/10.3390/su13126882.

[13] Faye, I.; Ndiaye, A.; Gecke, R.; Blieske, U.; Kobor, D.; Camara, M. Experimental Study of Observed Defects in Mini-Modules Based on Crystalline Silicone Solar Cell under Damp Heat and Thermal Cycle Testing. *Sol. Energy* **2019**, *191*, 161–166. https://doi.org/10.1016/j.solener.2019.08.054.

[14] Olanrewaju, Y. A.; Orisekeh, K.; Oyelade, O. V.; Koech, R. K.; Ichwani, R.; Ebunu, A. I.; Amune, D. I.; Bello, A.; Anye, V. C.; Oyewole, O. K.; Soboyejo, W. O. Effects of Temperature-Dependent Burn-in Decay on the Performance of Triple Cation Mixed Halide Perovskite Solar Cells. *AIP Adv.* **2022**, *12* (1), 015122. https://doi.org/10.1063/5.0078821.

[15] Yoon, J.; Sung, H.; Lee, G.; Cho, W.; Ahn, N.; Jung, H. S.; Choi, M. Superflexible, High-Efficiency Perovskite Solar Cells Utilizing Graphene Electrodes: Towards Future Foldable Power Sources. *Energy Environ. Sci.* **2017**, *10* (1), 337–345. https://doi.org/10.1039/C6EE02650H.

[16] Harry, K. J.; Hallinan, D. T.; Parkinson, D. Y.; MacDowell, A. A.; Balsara, N. P. Detection of Subsurface Structures underneath Dendrites Formed on Cycled Lithium

Metal Electrodes. *Nat. Mater.* **2014**, *13* (1), 69–73. https://doi.org/10.1038/nmat3793.

[17] Shi, D.; Adinolfi, V.; Comin, R.; Yuan, M.; Alarousu, E.; Buin, A.; Chen, Y.; Hoogland, S.; Rothenberger, A.; Katsiev, K.; Losovyj, Y.; Zhang, X.; Dowben, P. A.; Mohammed, O. F.; Sargent, E. H.; Bakr, O. M. Low Trap-State Density and Long Carrier Diffusion in Organolead Trihalide Perovskite Single Crystals. *Science (80-. ).* **2015**, *347* (6221), 519–522. https://doi.org/10.1126/science.aaa2725.

[18] Xing, G.; Mathews, N.; Sun, S.; Lim, S. S.; Lam, Y. M.; Gratzel, M.; Mhaisalkar, S.; Sum, T. C. Long-Range Balanced Electron- and Hole-Transport Lengths in Organic-Inorganic CH3NH3PbI3. *Science (80-. ).* **2013**, *342* (6156), 344–347. https://doi.org/10.1126/science.1243167.

[19] Stranks, S. D.; Eperon, G. E.; Grancini, G.; Menelaou, C.; Alcocer, M. J. P.; Leijtens, T.; Herz, L. M.; Petrozza, A.; Snaith, H. J. Electron-Hole Diffusion Lengths Exceeding 1 Micrometer in an Organometal Trihalide Perovskite Absorber. *Science (80-. ).* **2013**, *342* (6156), 341–344. https://doi.org/10.1126/science.1243982.

[20] Conings, B.; Drijkoningen, J.; Gauquelin, N.; Babayigit, A.; Haen, J. D.; Olieslaeger, L. D.; Ethirajan, A.; Verbeeck, J.; Manca, J.; Mosconi, E.; Angelis, F. De; Boyen, H. Intrinsic Thermal Instability of Methylammonium Lead Trihalide Perovskite. **2020**, 1–8. https://doi.org/10.1002/aenm.201500477.

[21] Wehrenfennig, C.; Eperon, G. E.; Johnston, M. B.; Snaith, H. J.; Herz, L. M. High Charge Carrier Mobilities and Lifetimes in Organolead Trihalide Perovskites. *Adv. Mater.* **2014**, *26* (10), 1584–1589. https://doi.org/10.1002/adma.201305172.

[22] Wang, Z.; McMeekin, D. P.; Sakai, N.; van Reenen, S.; Wojciechowski, K.; Patel, J. B.; Johnston, M. B.; Snaith, H. J. Efficient and Air-Stable Mixed-Cation Lead Mixed-Halide Perovskite Solar Cells with n-Doped Organic Electron Extraction Layers. *Adv. Mater.* **2017**, *29* (5), 1604186. https://doi.org/10.1002/adma.201604186.

[23] Meng, L.; You, J.; Yang, Y. Addressing the Stability Issue of Perovskite Solar Cells for Commercial Applications. *Nat. Commun.* **2018**, *9* (1), 5265.

https://doi.org/10.1038/s41467-018-07255-1.

[24] Kim, J. Y.; Lee, J.-W.; Jung, H. S.; Shin, H.; Park, N.-G. High-Efficiency Perovskite Solar Cells. *Chem. Rev.* **2020**, *120* (15), 7867–7918. https://doi.org/10.1021/acs.chemrev.0c00107.

[25] Kojima, A.; Teshima, K.; Shirai, Y.; Miyasaka, T. Organometal Halide Perovskites as Visible-Light Sensitizers for Photovoltaic Cells. *J. Am. Chem. Soc.* **2009**, *131* (17), 6050–6051. https://doi.org/10.1021/ja809598r.

[26] Ono, L. K.; Juarez-Perez, E. J.; Qi, Y. Progress on Perovskite Materials and Solar Cells with Mixed Cations and Halide Anions. *ACS Appl. Mater. Interfaces* **2017**, *9* (36), 30197–30246. https://doi.org/10.1021/acsami.7b06001.

[27] Li, Z.; Klein, T. R.; Kim, D. H.; Yang, M.; Berry, J. J.; van Hest, M. F. A. M.; Zhu, K. Scalable Fabrication of Perovskite Solar Cells. *Nat. Rev. Mater.* **2018**, *3* (4), 18017. https://doi.org/10.1038/natrevmats.2018.17.

[28] Bishop, J. E.; Routledge, T. J.; Lidzey, D. G. Advances in Spray-Cast Perovskite Solar Cells. *J. Phys. Chem. Lett.* **2018**, *9* (8), 1977–1984. https://doi.org/10.1021/acs.jpclett.8b00311.

[29] Bishop, J. E.; Smith, J. A.; Lidzey, D. G. Development of Spray-Coated Perovskite Solar Cells. *ACS Appl. Mater. Interfaces* **2020**, *12* (43), 48237–48245. https://doi.org/10.1021/acsami.0c14540.

# Chapter 2

# Literature Review

### 2.1 Solar Cells

In 1839, Alexandre Edmond Becquerel found the photovoltaic (PV) effect via a brass electrodes immersed in a conductive solution exposed in light. C.E. Fritts, in few years later, discovered a continuous and constant current with sunlight exposure when a placed of amorphous selenium on a metal backing and covered the selenium with a gold leaf film with photoconversion efficiency (PCE) less than 1% confirmed by Siemens at that time. After quantum mechanics was discovered around 75 years passed, the use of single-crystal semiconductor and p/n junction behavior was first recognized. Chapin et al. [1] invented the silicon single-crystal solar cell with 6% of PCE and the progress of silicon as solar cells has been improved until today [2]. Silicon has been a favored PV material with high efficiency that made it difficult to displace in PV community. However, a new generation of halide perovskites have attracted intense attention in the photovoltaic community owing to their efficiency and low-cost fabrication, compared to silicon counterparts [3].

#### 2.1.1 Perovskite Solar Cells (PSCs)

Perovskite is basically a crystal structures named after a Russian mineralogist, L. A. Perovski, described with general $ABX_3$ structures (Figure 2-1 (a)), in which A is a monovalent cation (such as methylammonium ($MA^+$), formamidium ($FA^+$) or Cesium ($Cs^+$)), B is divalent metallic cation (such as $Pb^{2+}$, $Sn^{2+}$, $Ge^{2+}$), and X is a halogen ($I^-$, $Br^-$, $Cl^-$) [4]. Perovskite materials has a strong optical absorption which reduce the required thickness for solar cells and solves challenges of collecting photogenerated carriers. Absorption measurements of perovskites

(Figure 2-1 (b)) are compared to other solar cells and shows an outstanding optical absorption that is one order of magnitude greater than that of GaAs) [5]. Perovskites also have a small effective mass for both carriers, low exciton binding energy, long carrier diffusion lengths (>1 μm), and long carrier lifetimes (273 ns) [6]. Perovskite materials have been widely for decades, but the use for sensitizers in solar cells, called perovskite solar cells, was first realized by Kojima *et al*. [7] in 2009 with PCE of 3.8%. An impressive progress has been made to achieve high performances PSCs such as controlling perovskite crystallization, compositional engineering, additive engineering, resulted of power conversion efficiencies of 25% in a decade [8].

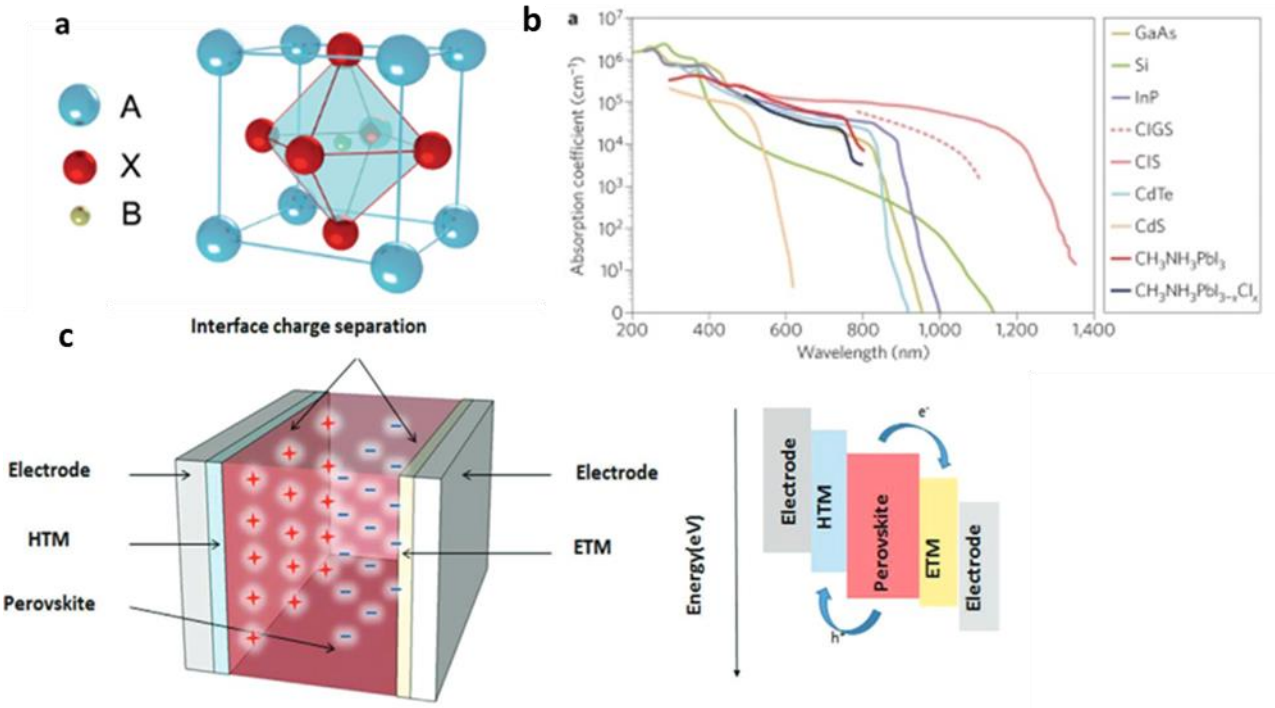


Figure 2-1. (a). $ABX_3$ perovskite structure. Adapted from Ref. [4], (b). Absorption Coefficient of $CH_3NH_3PbI_3$ perovskites compared to other solar cell materials. Adapted from Ref. [5], and (c). A working principle of PSCs and the associated energy alignment. Adapted from Ref. [9].

### 2.1.2 Operating Principles of PSCs

The structure of PSCs is a multilayered structure that consists of perovskite as the active layers sandwiched between a n-type electron transport layer (ETL) and a p-type electron transport layer (HTL) with the top electrode contacts on both sides [5]. (b) shows the general operating principle of PSCs. There are several processes occurred when light illuminated from the transparent conductive substrate. First, pairs of electron and hole are generated in perovskite layers once incident light is absorbed. Second, it produces a splitting of the electrons and holes called the charge separation. A driving force from energy level difference pushes electron to the ETL and holes to HTL. Third, the ETL collect the photogenerated electrons and transport it to the anode which is a transparent conductive oxide (TCO), while the HTL collect the photogenerated holes and transport it to the cathode (usually Au or Ag). Fourth, the electrons migrate to the external circuit via TCO, and the electric current is finally collected at the Au or Ag electrodes to complete photocurrent conversion process. Energy alignment among all functional layers in PSCs should carefully engineered to guarantee an efficiency charge separation and process completion [10,11].

### 2.1.3 Efficiency Measurements of PSCs

The current-voltage (*J-V*) characteristics is a main characterization to assess the performance of solar cells. Bias voltage is applied, and the corresponding photocurrent is measured. Figure 2-2 represents the resulted dark and illuminated *J-V* curves from a typical solar cell.

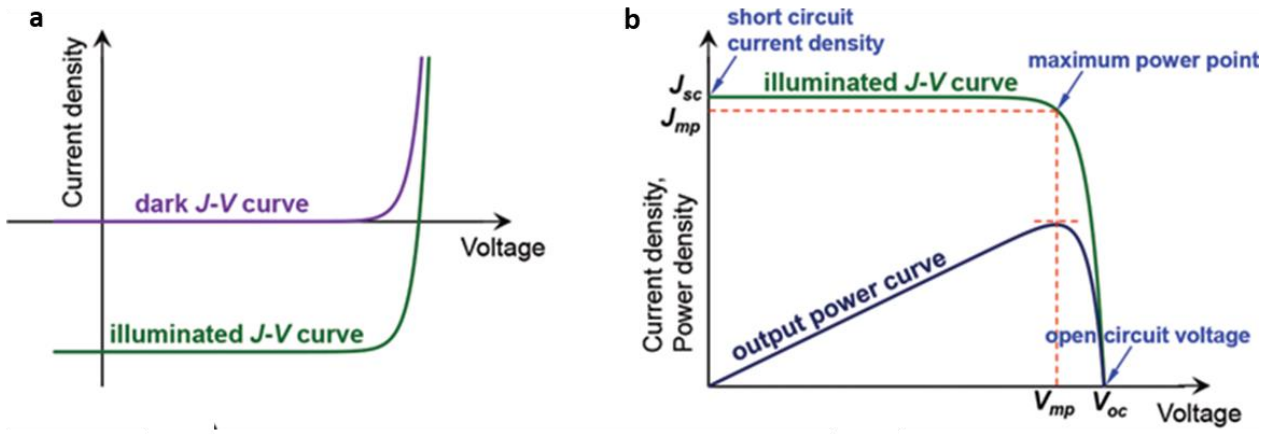


Figure 2-2. Dark and illuminated typical *J-V* characteristics of solar cells. (a) The difference between dark and illuminated *J-V* curve with output power density as a function of voltage. (b). The curve with detail label of the short-circuit point (0, $J_{sc}$), the open-circuit point ($V_{oc}$, 0), and the maximum power point ($V_{mp}$, $J_{mp}$). Adapted from Ref [12].

Through this test, there are some key parameters of solar cells that can be evaluated, including short-circuit current ($I_{sc}$), current density ($J_{sc}$), open-circuit voltage ($V_{oc}$), fill factor (*FF*), and photoconversion efficiency (PCE). The formula of the relationship given by

$$PCE, \eta\ (\%) = \frac{P_m}{P_{in}} = \frac{I_{sc}V_{oc}FF}{P_{in}A_{aperature}} = \frac{J_{sc}V_{oc}FF}{P_{in}} \quad (2.1)$$

where $P_{in}$ is the irradiance of the incident light, and $P_m$ is the maximum power output from the cells, and $A_{aperature}$is the area of the PSCs. Fill factor (FF) often explains the degree of internal losses of PSCs to see how realistically achieved performances compared to the ideally achievable performances.

$$FF = \frac{V_{mp}J_{mp}}{V_{oc}J_{sc}} \quad (2.2)$$

## 2.2 Mechanical Reliability of Multilayered Electronic Devices

Once an electronic device technology (e.g., perovskite solar cells) is established, some strategies to control force of adhesion between materials in multilayer stack structures are important to enable the functionality of the devices and to ensure that the devices can withstand the mechanical wear and tear for long time service. A mechanical integrity can be thought as the best predictor of the overall robustness of multilayer electronic devices. The reliability of multilayer devices can be evaluated on the macro and nanoscale level because physical separation in multilayer stack structures is strongly related to the electrical contact of devices. At this level, voids, cracks, and delamination due to internal and external stressors dictate the root of causes of failure in the multilayer devices. There are number of theories and techniques that can be used to quantify the interfacial adhesion and resistance for fracture at macro and nanoscale.

### 2.2.1 Adhesion in Electronic Structures

All surfaces have different level of roughness. A contact between surfaces is carried by different asperities on the surfaces. Due to the inter-atomic attractions, the asperities contact results in the adhesive contact. Surfaces that have a multitude of asperities are difficult to form a very flat contact to other surfaces. A much smaller of the real contact is always observed compared to the apparent contact area [10]. Adhesion is common phenomena in miniaturized devices, not limited to micro/nano-mechanical systems (MEMS) and magnetic storage devices. Adhesion can critically influence the efficiency or power output of those devices[11].

Atomic Force microscope (AFM) has been used to study the adhesion forces and surface structures over many of materials. AFM utilizes the sharp tip to make interactions with sample surfaces at a distance of atomic dimensions. The tip will sense the interaction forces over a surface and capture it as surface images. The interaction will be affected by the morphology and the roughness of the surfaces, tip materials, the environment when the

AFM testing being done. The forces made between tip and the surfaces are mainly due to the *van der Walls* and capillary interactions because of water meniscus formed the end of the tip. Therefore, a controlled humidity environment is important in conducting any experiments using AFM.

Prior works by Wolf *et al*.[12] has been evaluated the adhesion between the constituent layer of coating, and between coating and the substrates in a drug-eluting stent (DES). by using AFM. Coated AFM tips and two-dimensional coupons acting as surrogates to the substrate were interacted to evaluate the adhesion between all possible interfaces. Similar AFM work has also been done by Obayemi e*t al*.[13] for interaction between conjugated magnetite nanoparticle systems and the specific targeting of triple negative breast cancer to improve the selectivity in cancer detection and treatments. In the cases of electronic devices, AFM has also been used by Tong *et al*. [14] to quantify the adhesion between different functional layers in organic photovoltaic (OPV) systems and incorporated the surface parameter to analytically calculated the adhesion energy for designing robust structures of OPVs. Therefore, adhesion is a very useful predictor to understanding the nanoscale interfacial interaction between two dissimilar surfaces in many systems.

### 2.2.2 Contact Theories

Theory of Hertz has been modelled for elastic adhesion, while theory such as JKR and DMT model has been modelled adhesion with taking account the surface energy[15] and cohesive forces at the contact periphery[16], respectively. The model of *Johnson-Kendal-Roberts* (JKR) describes adhesion in "soft" elastic materials, strong adhesion forces, and large tip radii, where adhesion forces outside the contact area are neglected. In contrast, the *Derjaguin-Muller-Toporov* (DMT) approximation is valid for "hard" materials, weak adhesion forces, and small tip radii. The *Maugis-Dugdale* (MD) model has developed for molecular smooth surfaces for any materials with high and low adhesions, which was being regime between the limitations of JKR and DMT model)[17].

Contact mechanics can be used to extract the value of the adhesion energy from the measured pull-off forces. This can be done using adhesion models that have been developed for different ranges of attractive forces and surface geometries[18]. The relationship of JKR model between the adhesion energy ($\gamma$) and the adhesive force ($F$) is given by [19]:

$$F = \frac{3}{2}\pi\gamma R \tag{2.3}$$

For DMT approximation, the equation is given by:

$$F = 2\pi\gamma R \tag{2.4}$$

where $R$ is the effective radius of curvature that is given by

$$R = \left(\frac{1}{R_{tip}} + \frac{1}{R_{rms}}\right)^{-1} \tag{2.5}$$

where $R_{rms}$ and $R_{tip}$ are the average roughness of the coated surface and radius of coated probing tip[14,20].

For MD model, an analytical method must be used to approximate the relationship between adhesion force and energy. However, the model has been simplified through iteration approach by Carpick *et al*.[21] and further generalized by Pietrement and Troyon [22]. A non-dimensionalized parameter ($\lambda$) was used to determine the applicable models in the specific cases. The DMT model is applied when $\lambda < 0.1$, the JKR applied is when $\lambda > 5$, and MD model is between those two-limiting cases. The calculation of $\lambda$ can be done using the knowledge of material and geometric properties of surfaces, given by:

$$\lambda = 2\sigma_o \left(\frac{R}{\pi K^2 \gamma}\right)^{\frac{1}{3}} = -0.913\ln\left(1 - 1.018\alpha\right) \tag{2.6}$$

where the $K$ constant can be calculated from:

$$= \frac{4}{3}\left(\frac{R}{\pi K^2 \gamma}\right)^{\frac{1}{3}} = -0.913\ln(1 - 1.018\alpha) \quad (2.7)$$

where $v_i$ is the Poisson's ration for layer i=1,2 and $E_i$ is the elastic modulus of those layers.

### 2.2.3 Interfacial Fracture Testing

Fracture energy, *G*, is an important predictor in preserving the functionality of devices. Once fracture is induced in multilayer electronic devices, surface separation is induced, and electron transfer will be disturbed due to the lack of physical pathway for the charge transportation. The critical energy release rate, *G*, required to develop interfacial crack growth between materials can be determined by fracture mechanics measurements. *G* defines as the rate of potential energy changes with the respect to the crack area for a linear elastic material [23]. Fracture will be induced when *G* reaches the critical threshold $G_c$ ($G=G_c$). In atomic level, this is equivalent when external forces reach the cohesive bonding between two atoms.

*Brazilian Disk*

Brazilian test is a technique in fracture mechanics used to evaluate the mechanical properties of brittle materials such as concrete or rocks[24], dental cement composites [25,26], marble/adhesive interfaces [27], and organic electronic structures [28]. The Brazil disk experiment consists of compressing a circular disk that can be oriented over ranges of mode mixity to initiate fracture along the deposited samples. The loading phase was controlled by varying the inclination angle, $\theta$. The stress intensity factors for modes I and II are given by Equations (2.8-2.9)[28].

$$K_I = f_I \sigma(\pi l)^{-1/2} \quad (2.8)$$

$$K_{II} = f_{II} \sigma(\pi l)^{-1/2} \quad (2.9)$$

In Equations (2.8-2.9), $l$ is the crack length, $f_I$ and $f_I$ are the non-dimensional calibration factors which a function of the loading angle, $\theta$, and relative crack length, $l/a$. Equation (2.10) yields the stress, $\sigma$, where $F_{\max}$ is the maximum applied load to induce fracture from the compressive testing, $a$ is the disk radius and $t$ is the disk thickness.

$$\sigma = \frac{F_{\max}}{\pi a t} \tag{2.10}$$

The overall energy release rate can be calculated as in Equation (2.11) where $E^*$ is the plane strain Young's modulus for bi-material pairs[26].

$$G = G_I + G_{II} = \frac{1}{E^*}\left({K_I}^2 + {K_{II}}^2\right) \tag{2.11}$$

The mode mixities can be expressed as in Equation (2.12).

$$\psi = tan^{-1}\left(\frac{K_I}{K_{II}}\right) + \omega + \varepsilon\, ln\left(\frac{\hat{L}}{h}\right) \tag{2.12}$$

In Equation (2.11), $\hat{L}$ is a fixed length to define the loading phase and $h$ is the layer thickness.

*Toughening mechanism*

Toughening is the improvement of the fracture resistance of a given material. Evans and Hutchinson [29] introduced the dependence of interfacial fracture toughness using a simple model of connecting facets along the crack surface. Mixed mode, mode I (crack opening) and mode II (in-plane shear), and non-planarity of the interface are involved in the interfacial fracture problems. Figure 2-3**Error! Reference source not found.** (a) shows the $G$ trend with the phase angle of loading toughened by crack/kink mechanism, consisting of kinks along

the crack surface. The stress intensity at the crack front differs from the applied stress due to the kink angle, kink amplitude and the friction coefficient. In contrast, the zone model stress intensity is simulated by a continuous linear spring model ((b)). Zone model (Figure 2-3 (b)) model idealizes the bridged crack as a distribution of equivalent microcracks or equivalent bridges.

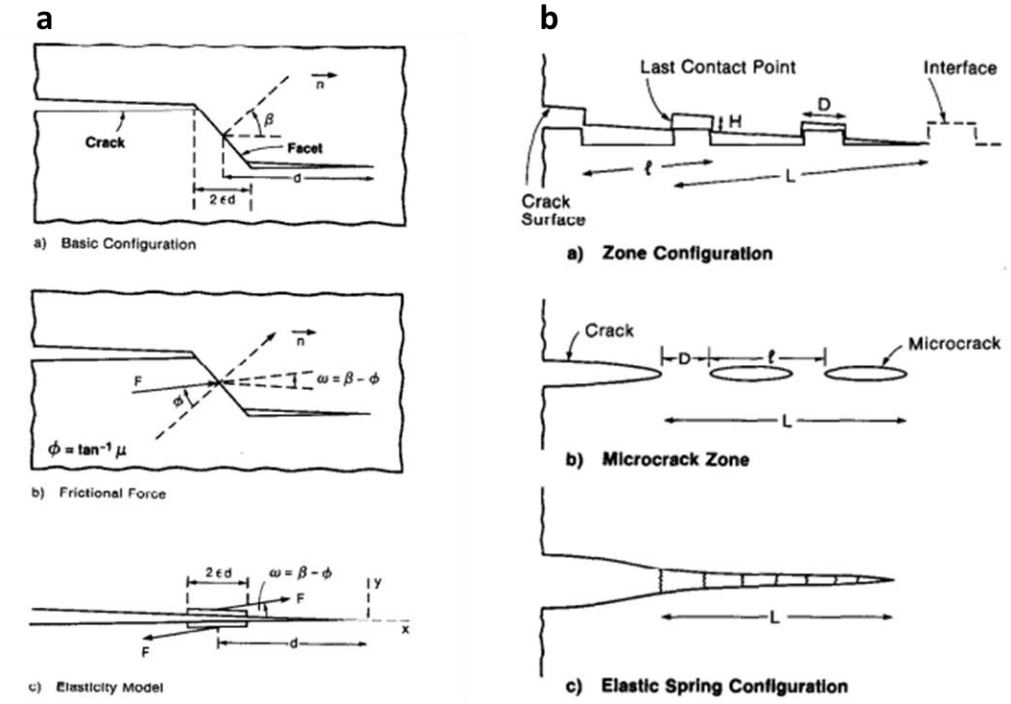


Figure 2-3.The illustration of crack/kink model used to analyze crack surface contact effect (a), and the zone model used to determine *G* with phase angle of loading (b). Adapted from Ref[29].

The crack-tip shielding associated with the zone model of Evans and Hutchinson that can be determined from Ref. [30] to be:

$$\frac{\Delta G}{G} = \frac{tan^2\psi\left\{1-k\left[\alpha_o\left(1+tan^2\psi\right)\left(\frac{\Delta G}{G}+1\right)\right]\right\}}{1+\ tan^2\psi} \tag{2.13}$$

where the function $k(\alpha)$ is given in Table 1 (as $1/\lambda$) in Ref. [30] and $\alpha_o$ is a material parameter that can be calculated from Equation (2.14), which gives:

$$\alpha_o = \frac{\pi E H^2 / l G_o}{32(1-\nu^2)\ln\left(1/\sin\frac{\pi D}{2l}\right)} \tag{2.14}$$

As defined in Equation (2.14), a parameter $\chi$ contains basic information of contact zone dimension where large value of $\chi$ (~10) associates to maximum contact and small value of $\chi$ (~0.10) associates to lack of contact.

$$\chi = \frac{EH}{G_o} \tag{2.15}$$

In the case of large $\chi$ values, the contact forces have maximum level of crack tip shielding and $K_{II} \sim 0$. Hence, the toughening can be simplified based on the pure mode I energy release rate, $G_o$, as in Equation (2.16).

$$G = G_o\,(1 + tan^2\psi) \tag{2.16}$$

## 2.3 Scalability of Perovskite Solar Cells

### 2.3.1 Scalable Processing for PSCs technology

The progress towards the scalable perovskites has been impressive in the past few years. A widely used spin-coating technique has only limited to the 10x10 cm area substrates where the large portion of the solution is being wasted during spinning. However, the resulted 10x10 cm spin-coated PSCs show a significant loss in PCE compared to the small area devices, due to the difficulty to obtain smooth and thin wet-solution through the continuous centrifugal force for large-scale cells. Fabricating uniform coverage and pinhole-free perovskite films on large scales remained a challenge in PSCs scalability. Therefore, PV

community has explored some possible scalable fabrication techniques, including doctor-blade coating, slot-die coating, spray coating, inkjet and screen printing (Figure 2-4) [31–33]. The state-of-art development of all techniques are compared in Table 2.1.

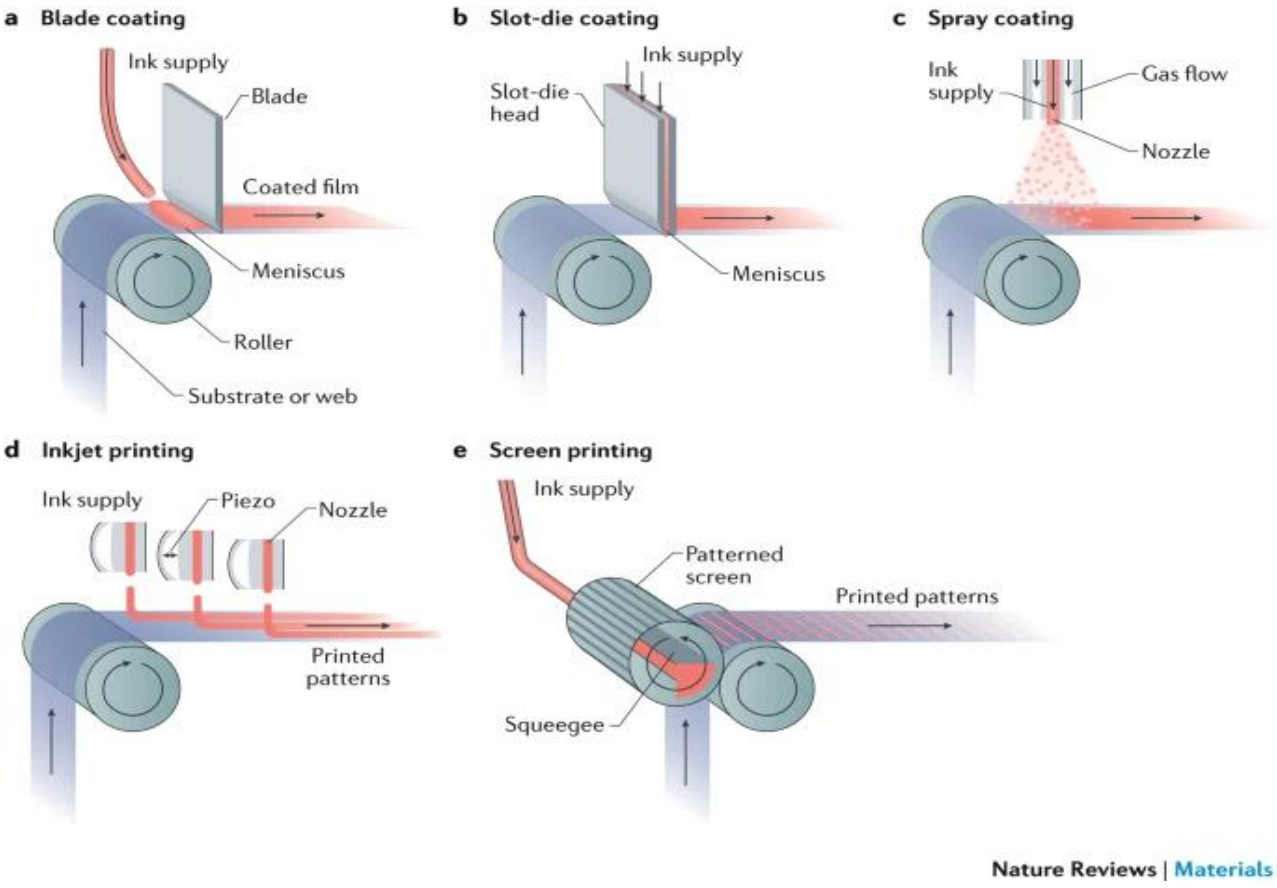


Figure 2-4. Common scalable method for perovskite deposition, namely blade coating (a), slot-die coating (b), spray coating (c), inkjet printing (d), and screen printing (e). Adapted from Ref.[32]

Table 2.1 The progress of scalable PSCs fabrication techniques [32]

| Fabrication Method | Demonstration in device stack | State-of-the-art PCE cells (%) | |
|---|---|---|---|
| | | Single | Module |

| | | | |
|---|---|---|---|
| **(a) Blade coating**<br>*A technique to spread precursor solution on substrate to form wet thin films* | Perovskite<br>ETL and HTL | 19.5 [34] | 14.1 [35] |
| **(b) Slot-die coating**<br>*A similar technique as blade coating that uses an ink reservoir with a thin slit to apply ink over the substrate* | Perovskite<br>ETL and HTL | 14.7 [36] | - |
| **(c) Spray coating**<br>*A technique includes the dispersion of tiny liquid droplets onto substrates* | Perovskite, ETL, HTL | 18.3 [37] | 15.5 [37] |
| **(d) Inkjet printing**<br>*A technique that uses a nozzle to disperse the ink with fine control of the droplet size and trajectory* | Perovskite | 12.3 [38] | - |
| **(e) Screen printing**<br>*A technique that utilizes a patterned mesh screen to hold and transfer ink to the substrates* | ETL<br>HTL | 15.6 [39] | 10.8[40] |

### 2.3.2 Spray Coating

Spray coating has been extensively explored for thin film PV technology such as organic and perovskite solar cells. Spray coating is solution-based coating technique that utilizes the nozzle to disperse liquid microdroplet onto a substrate. There are some types of spray coating depending on the method use for droplet generation, namely pneumatic spray using the fast gas flow, ultrasonic spray using ultrasonic vibration on the nozzle, and electro spraying using electrical repulsion [32].

Spray coating has some advantages such as a fast deposition time where a spray head can move across the substrate at 5 m/s which is twice than the speeds for slot-die coating. Another benefit is that spray coating is able to coat nonplanar substrates as spray head is not in close contact to the substrates [41]. However, new droplets in spray processing can dissolved the already formed films. Some treatments such keeping the substrate at elevated temperature, tuning the solvent composition are useful to limit the material dissolution [37]. In the perovskites case, controlling the substrate temperature is very important during spray because of the fast growth of perovskite, forming thin film with dendritic structures (Figure 2-5).

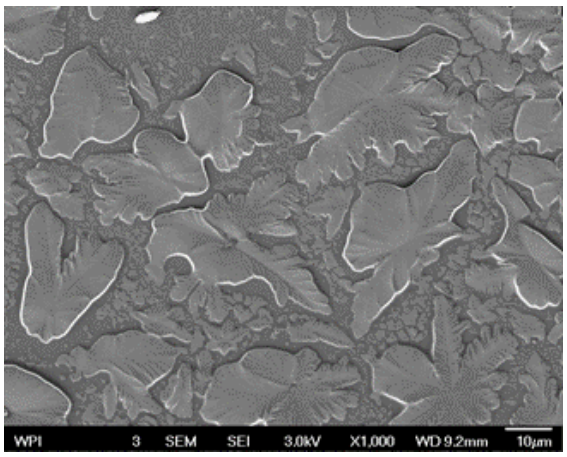


Figure 2-5. Perovskite morphology via spray-assisted technique with uncontrolled drying process

### 2.3.3 Machine Learning for Process Optimization

Machine learning (ML) is an approach which allows computers to learn from data. ML approach is very applicable in domains of studies such as face recognition, image processing, manufacturing, medical and other areas [45]. ML is found to be useful in improvement of quality control optimization and extracting implicit relationship from of high-dimensional variables data [46], predicting material properties [47], and speeding material discovery [48], which have drawn attention in photovoltaic community.

In this fast-faced era, the ease of large amount of data processing provided by data science tool should help scientist in designing more systematic experiments, data collection and methodology analysis. ML can guide scientists in experimental planning, which leverage a comprehensive in data analysis or crating new ideas, rather than going through tedious and poorly reproducible laboratory experiments[49].

Spray coating is potentially used to enable scalable production of PSCs, though the system has a high-dimensional space for optimization which adds more complexity to the process. Optimization of variables in spray coating systems is often challenging as it is not economically friendly in time and budget. Paulson *et al*. [50] has been implemented statistical methods such as Latin hypercube design of experiments, machine learning surrogate modeling, and Bayesian optimization to optimize input variables in the flame spray pyrolysis, enabling a desirable particle size distribution.

P-type transparent conducting materials (p-TCMs) such as Cu-Zn-S film is a crucial component in solar cells that has also been explored using machine learning (ML) approach. A regression model was used to strategize design of experiments (DOE) of multidimensional p-TCMs synthesis conditions via chemical bath deposition (CBD) that relies on precursor depositions, temperature, pH, complexing agents. Wei, *et al*. [51] used a vector regression-based model with a radial basis function. After the *first-round* experiment, the predicted ranges in the parameter space with optimum figure of merit (FOM) related to the film conductivity and optical transmission as a target variable were suggested to have better DOE for the *next-round* of experiments. These examples suggest that machine learning allows us to stimulate different scenarios and adjust the control parameter of a fabrication method in leveraging the improvement of spray-assisted PSCs.

**References**


[1] D.M. Chapin, C.S. Fuller, G.L. Pearson, A New Silicon p-n Junction Photocell for Converting Solar Radiation into Electrical Power, J. Appl. Phys. 25 (1954) 676–677. https://doi.org/10.1063/1.1721711.

[2] L. Fraas, L. Partain, SOlar Cells and Their Applications, Wiley, 2010.

[3] M.A. Green, A. Ho-Baillie, H.J. Snaith, The emergence of perovskite solar cells, Nat. Photonics. 8 (2014) 506–514. https://doi.org/10.1038/nphoton.2014.134.

[4] Y. Chen, L. Zhang, Y. Zhang, H. Gao, H. Yan, Large-area perovskite solar cells – a review of recent progress and issues, RSC Adv. 8 (2018) 10489–10508. https://doi.org/10.1039/C8RA00384J.

[5] M.A. Green, A. Ho-Baillie, H.J. Snaith, The emergence of perovskite solar cells, Nat. Photonics. 8 (2014) 506–514. https://doi.org/10.1038/nphoton.2014.134.

[6] H.-S. Kim, A. Hagfeldt, N.-G. Park, Morphological and compositional progress in halide perovskite solar cells, Chem. Commun. 55 (2019) 1192–1200. https://doi.org/10.1039/C8CC08653B.

[7] A. Kojima, K. Teshima, Y. Shirai, T. Miyasaka, Organometal halide perovskites as visible-light sensitizers for photovoltaic cells, J. Am. Chem. Soc. 131 (2009) 6050–6051. https://doi.org/10.1021/ja809598r.

[8] N.R.E.L. (NREL), Best Research-Cell Efficiency Chart, (n.d.). https://www.nrel.gov/pv/cell-efficiency.html.

[9] Y. Wang, X. Liu, Z. Zhou, P. Ru, H. Chen, X. Yang, L. Han, Reliable Measurement of Perovskite Solar Cells, Adv. Mater. 31 (2019) 1803231. https://doi.org/10.1002/adma.201803231.

[10] P. Gao, D. Konrad, S. Aghazada, M.K. Nazeeruddin, Molecular Engineering of Functional Materials for Energy and Opto-Electronic Applications, Chimia (Aarau). 69 (2015) 253. https://doi.org/10.2533/chimia.2015.253.

[11] P. Liu, W. Wang, S. Liu, H. Yang, Z. Shao, Fundamental Understanding of Photocurrent Hysteresis in Perovskite Solar Cells, Adv. Energy Mater. 9 (2019) 1803017. https://doi.org/10.1002/aenm.201803017.

[12] Y. Tao, Screen-Printed Front Junction n-Type Silicon Solar Cells, in: Print. Electron. - Curr. Trends Appl., InTech, 2016. https://doi.org/10.5772/63198.

[13] P. Prokopovich, S. Perni, Comparison of JKR- and DMT-based multi-asperity adhesion model: Theory and experiment, Colloids Surfaces A Physicochem. Eng. Asp. 383 (2011) 95–101. https://doi.org/10.1016/j.colsurfa.2011.01.011.

[14] R. Maboudian, Critical Review: Adhesion in surface micromechanical structures, J. Vac. Sci. Technol. B Microelectron. Nanom. Struct. 15 (1997) 1. https://doi.org/10.1116/1.589247.

[15] K. V. Wolf, Z. Zong, J. Meng, A. Orana, N. Rahbar, K.M. Balss, G. Papandreou, C.A. Maryanoff, W. Soboyejo, An investigation of adhesion in drug-eluting stent layers, J. Biomed. Mater. Res. Part A. 87A (2008) 272–281. https://doi.org/10.1002/jbm.a.31860.

[16] J.D. Obayemi, J. Hu, V.O. Uzonwanne, O.S. Odusanya, K. Malatesta, N. Anuku, W.O. Soboyejo, Adhesion of ligand-conjugated biosynthesized magnetite nanoparticles to triple negative breast cancer cells, J. Mech. Behav. Biomed. Mater. 68 (2017) 276–286. https://doi.org/10.1016/j.jmbbm.2017.02.004.

[17] T. Tong, B. Babatope, S. Admassie, J. Meng, O. Akwogu, W. Akande, W.O. Soboyejo, Adhesion in organic electronic structures, J. Appl. Phys. 106 (2009) 083708. https://doi.org/10.1063/1.3246786.

[18] Surface energy and the contact of elastic solids, Proc. R. Soc. London. A. Math. Phys. Sci. 324 (1971) 301–313. https://doi.org/10.1098/rspa.1971.0141.

[19] B.. Derjaguin, V.. Muller, Y.. Toporov, Effect of contact deformations on the adhesion of particles, J. Colloid Interface Sci. 53 (1975) 314–326. https://doi.org/10.1016/0021-9797(75)90018-1.

[20] D. Maugis, Adhesion of spheres: The JKR-DMT transition using a dugdale model, J. Colloid Interface Sci. 150 (1992) 243–269. https://doi.org/10.1016/0021-9797(92)90285-T.

[21] R.C. Thomas, J.E. Houston, R.M. Crooks, T. Kim, T.A. Michalske, Probing Adhesion Forces at the Molecular Scale, J. Am. Chem. Soc. 117 (1995) 3830–3834. https://doi.org/10.1021/ja00118a019.

[22] D.S. Grierson, E.E. Flater, R.W. Carpick, Accounting for the JKR–DMT transition in adhesion and friction measurements with atomic force microscopy, J. Adhes. Sci. Technol. 19 (2005) 291–311. https://doi.org/10.1163/1568561054352685.

[23] D. Yu, O.K. Oyewole, D. Kwabi, T. Tong, V.C. Anye, J. Asare, E. Rwenyagila, A. Fashina, O. Akogwu, J. Du, W.O. Soboyejo, Adhesion in flexible organic and hybrid organic/inorganic light emitting device and solar cells, J. Appl. Phys. 116 (2014) 074506. https://doi.org/10.1063/1.4892393.

[24] R.W. Carpick, D.F. Ogletree, M. Salmeron, A General Equation for Fitting Contact Area and Friction vs Load Measurements, J. Colloid Interface Sci. 211 (1999) 395–400. https://doi.org/10.1006/jcis.1998.6027.

[25] O. Piétrement, M. Troyon, General Equations Describing Elastic Indentation Depth and Normal Contact Stiffness versus Load, J. Colloid Interface Sci. 226 (2000) 166–171. https://doi.org/10.1006/jcis.2000.6808.

[26] T.L. Anderson, Fracture Mechanics, CRC Press, 2017.

https://doi.org/10.1201/9781315370293.

[27] E. Sgambitterra, C. Lamuta, S. Candamano, L. Pagnotta, Brazilian disk test and digital image correlation: a methodology for the mechanical characterization of brittle materials, Mater. Struct. 51 (2018) 19. https://doi.org/10.1617/s11527-018-1145-8.

[28] J. Zhou, M. Huang, F. Sagnang, W.O. Soboyejo, Interfacial failure of a dental cement composite bonded to glass substrates, Dent. Mater. 22 (2006) 585–591. https://doi.org/10.1016/j.dental.2005.06.007.

[29] N. Rahbar, Y. Yang, W. Soboyejo, Mixed mode fracture of dental interfaces, Mater. Sci. Eng. A. 488 (2008) 381–388. https://doi.org/10.1016/j.msea.2007.11.038.

[30] N. Rahbar, M. Jorjani, C. Riccardelli, G. Wheeler, I. Yakub, T. Tan, W.O. Soboyejo, Mixed mode fracture of marble/adhesive interfaces, Mater. Sci. Eng. A. 527 (2010) 4939–4946. https://doi.org/10.1016/j.msea.2010.04.029.

[31] T.M. Tong, Ting Tan, N. Rahbar, W.O. Soboyejo, Mode Mixity Dependence of Interfacial Fracture Toughness in Organic Electronic Structures, IEEE Trans. Device Mater. Reliab. 14 (2014) 291–299. https://doi.org/10.1109/TDMR.2013.2256788.

[32] A.. Evans, J.. Hutchinson, Effects of non-planarity on the mixed mode fracture resistance of bimaterial interfaces, Acta Metall. 37 (1989) 909–916. https://doi.org/10.1016/0001-6160(89)90017-5.

[33] B. Budiansky, J.C. Amazigo, A.G. Evans, Small-scale crack bridging and the fracture toughness of particulate-reinforced ceramics, J. Mech. Phys. Solids. 36 (1988) 167–187. https://doi.org/10.1016/S0022-5096(98)90003-5.

[34] J. Seo, S. Park, Y. Chan Kim, N.J. Jeon, J.H. Noh, S.C. Yoon, S. Il Seok, Benefits of very thin PCBM and LiF layers for solution-processed p–i–n perovskite solar cells, Energy Environ. Sci. 7 (2014) 2642–2646. https://doi.org/10.1039/C4EE01216J.

[35] Z. Li, T.R. Klein, D.H. Kim, M. Yang, J.J. Berry, M.F.A.M. van Hest, K. Zhu, Scalable fabrication of perovskite solar cells, Nat. Rev. Mater. 3 (2018) 18017. https://doi.org/10.1038/natrevmats.2018.17.

[36] H. Yao, S. Shi, Z. Li, Z. Ci, G. Zhu, L. Ding, Z. Jin, Strategies from small-area to scalable fabrication for perovskite solar cells, J. Energy Chem. 57 (2021) 567–586. https://doi.org/10.1016/j.jechem.2020.08.033.

[37] S. Tang, Y. Deng, X. Zheng, Y. Bai, Y. Fang, Q. Dong, H. Wei, J. Huang, Composition Engineering in Doctor-Blading of Perovskite Solar Cells, Adv. Energy Mater. 7 (2017) 1700302. https://doi.org/10.1002/aenm.201700302.

[38] J. Su, H. Cai, J. Yang, X. Ye, R. Han, J. Ni, J. Li, J. Zhang, Perovskite Ink with an Ultrawide Processing Window for Efficient and Scalable Perovskite Solar Cells in Ambient Air, ACS Appl. Mater. Interfaces. 12 (2020) 3531–3538. https://doi.org/10.1021/acsami.9b17141.

[39] T. Qin, W. Huang, J.-E. Kim, D. Vak, C. Forsyth, C.R. McNeill, Y.-B. Cheng, Amorphous hole-transporting layer in slot-die coated perovskite solar cells, Nano Energy. 31 (2017) 210–217. https://doi.org/10.1016/j.nanoen.2016.11.022.

[40] J.H. Heo, M.H. Lee, M.H. Jang, S.H. Im, Highly efficient CH 3 NH 3 PbI 3−x Cl x mixed halide perovskite solar cells prepared by re-dissolution and crystal grain growth via spray coating, J. Mater. Chem. A. 4 (2016) 17636–17642. https://doi.org/10.1039/C6TA06718B.

[41] S.-G. Li, K.-J. Jiang, M.-J. Su, X.-P. Cui, J.-H. Huang, Q.-Q. Zhang, X.-Q. Zhou, L.-M. Yang, Y.-L. Song, Inkjet printing of CH 3 NH 3 PbI 3 on a mesoscopic TiO 2 film for highly efficient perovskite solar cells, J. Mater. Chem. A. 3 (2015) 9092–9097. https://doi.org/10.1039/C4TA05675B.

[42] Y. Rong, X. Hou, Y. Hu, A. Mei, L. Liu, P. Wang, H. Han, Synergy of ammonium chloride and moisture on perovskite crystallization for efficient printable mesoscopic solar cells, Nat. Commun. 8 (2017) 14555. https://doi.org/10.1038/ncomms14555.

[43] A. Priyadarshi, L.J. Haur, P. Murray, D. Fu, S. Kulkarni, G. Xing, T.C. Sum, N. Mathews, S.G. Mhaisalkar, A large area (70 cm 2 ) monolithic perovskite solar module with a high efficiency and stability, Energy Environ. Sci. 9 (2016) 3687–3692. https://doi.org/10.1039/C6EE02693A.

[44] J.E. Bishop, J.A. Smith, D.G. Lidzey, Development of Spray-Coated Perovskite Solar Cells, ACS Appl. Mater. Interfaces. 12 (2020) 48237–48245. https://doi.org/10.1021/acsami.0c14540.

[45] T. Nasir, M. Asmael, Q. Zeeshan, D. Solyali, Applications of Machine Learning to Friction Stir Welding Process Optimization, J. Kejuruter. (2020) 171–186. https://doi.org/https://doi.org/10.17576/jkukm-2020-32(2)-01.

[46] G. Köksal, İ. Batmaz, M.C. Testik, A review of data mining applications for quality improvement in manufacturing industry, Expert Syst. Appl. 38 (2011) 13448–13467. https://doi.org/10.1016/j.eswa.2011.04.063.

[47] L. Wilbraham, R.S. Sprick, K.E. Jelfs, M.A. Zwijnenburg, Mapping binary copolymer property space with neural networks, Chem. Sci. 10 (2019) 4973–4984. https://doi.org/10.1039/C8SC05710A.

[48] F. Häse, L.M. Roch, A. Aspuru-Guzik, Next-Generation Experimentation with Self-Driving Laboratories, Trends Chem. 1 (2019) 282–291. https://doi.org/10.1016/j.trechm.2019.02.007.

[49] V.M. Le Corre, T.S. Sherkar, M. Koopmans, L.J.A. Koster, Identification of the dominant recombination process for perovskite solar cells based on machine learning,

Cell Reports Phys. Sci. 2 (2021) 100346. https://doi.org/10.1016/j.xcrp.2021.100346.

[50] N.H. Paulson, J.A. Libera, M. Stan, Flame spray pyrolysis optimization via statistics and machine learning, Mater. Des. 196 (2020) 108972. https://doi.org/10.1016/j.matdes.2020.108972.

[51] L. Wei, X. Xu, Gurudayal, J. Bullock, J.W. Ager, Machine Learning Optimization of p-Type Transparent Conducting Films, Chem. Mater. 31 (2019) 7340–7350. https://doi.org/10.1021/acs.chemmater.9b01953.

# Chapter 3

# Adhesion in Perovskite Solar Cell Multilayer Structures

### 3.1 Introduction

Lead-based halide perovskite solar cells (PSCs) have received considerable attention in recent years due to their attractive combinations of high power conversion efficiencies (up to 25%) and the potential for low cost manufacturing[1–5]. To date, most of photoactive active layers in PSCs have been fabricated through solution processing method. Although efficient cells have been made, some challenges are related to large area film formation, poor reproducibility of film morphology, stability and difficulties of constructing patterned multilayer devices, which are hindering the future commercialization of perovskite solar cells [6]. Therefore, vapor deposition of perovskite films has attracted significant interest to overcome some of the problems. Vapor deposition are expected to grow perovskite with high chemical purity due to the control of deposition parameters and vacuum environment, as well as with large area devices [7,8].

Lead-based halide perovskites such as $MAPbI_3$, have moderate mechanical properties measured by nanoindentation of the single crystals. These include: Young's moduli of ~17.8 GPa, hardness values of ~0.58 GPa, and toughness values of ~2.7 $J/m^{-2}$ [9–11]. Brittle interfaces between perovskite films and the adjacent layer in planar PSCs have also been reported with interfacial toughness ($G_c$) of less than 1.5 $J/m^{-2}$ [12]. Since perovskite solar cells consist of multiple functional layers, interfacial robustness at each interface can have a significant effect on charge carrier transport across the interfaces. Prior work on the interfacial robustness of

perovskite solar cells has explored the mode mixity dependence of interfacial fracture toughness[13]. The studies showed that the interfacial fracture toughness values vary significantly with surface chemistry and the underlying toughening mechanisms. However, these authors are unaware of prior measurements of the adhesion between layers that are relevant to PSCs. Therefore, there is a need for fundamental understanding of the adhesion at interfaces of layered PSC structures.

Thus, in this work, we explore the adhesion between layers that are relevant to PSCs which are produced using different deposition techniques (Figure 1a). Interfacial adhesive forces between layers that are associated with the different PSC structures are measured using atomic force microscopy (AFM) technique. This study utilizes methylammonium lead iodide ($MAPbI_3$) that are crystallized through vapor and solution methods, as well as solution-processed mixed-cations mixed-halides (FA-MA-Br-I) photoactive absorbers (FA-rich perovskite). The charge carrier dynamics and photoconversion characteristics of all PSC cells are characterized and correlated to the measured interfacial adhesive forces. The implications of results are discussed for improved fabrication of robust PSC structures.

### 3.2 Theory

To determine the pull-off forces between two adjacent surfaces that are relevant to PSC, the adhesion forces were measured between coated AFM tips and the relevant surfaces that were deposited on similar substrates to those of the PSC structures (Figure 3-1 (a)). Figure 3-1 (b) shows cross-sectional SEM images of PSCs with colors associated to the functional layer of the cell in Figure 3-1 (a).

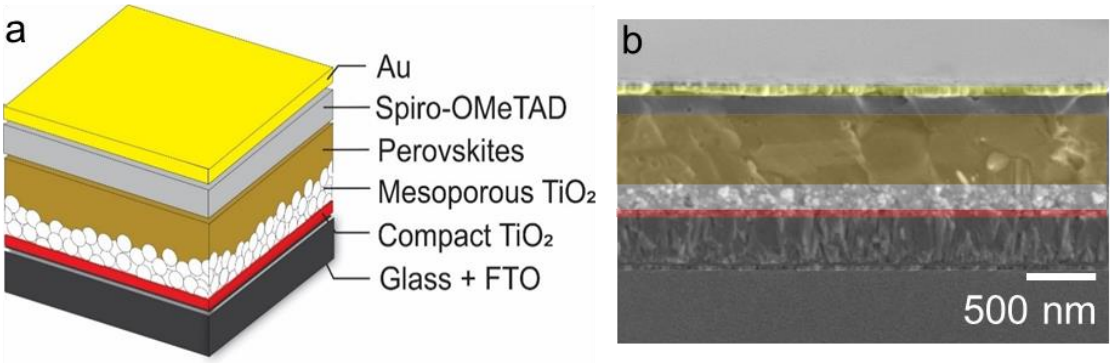


Figure 3-1 (a) Mesoscopic Architecture of Perovskite Solar Cells, and (b) Representative cross-sectional SEM image of perovskite solar cells used in this study

A schematic of a typical force-displacement curve obtained via force microscopy is presented in Figure 3-2. Figure 3-2 (a) corresponds to the initial position, where the cantilever is placed above the substrate. The AFM tip approaches the surface but has not yet reached the surface. However, as the tip approaches the surfaces, it jumps to contact, because of adhesive interactions. The contact is followed by cantilever bending, as shown in Figure 3-2 (b). Figure 3-2 (c) corresponds to the regime in which the cantilever is in contact with the substrate and AFM scanner continues to move down vertically. If the cantilever is sufficiently stiff and the material is soft, the tip will indent the surface as the tip bends elastically. Subsequently, the cantilever is withdrawn (Figure 3-2 (d)). However, due to the effects of adhesion, the tip does not detach from the substrate at zero force. Thus, the retraction continues until the tip pulls off from the substrate at a negative force (Figure 3-2 (e)) that corresponds to the adhesion force ($F$). The cantilever then returns back the initial position at A [14,15].

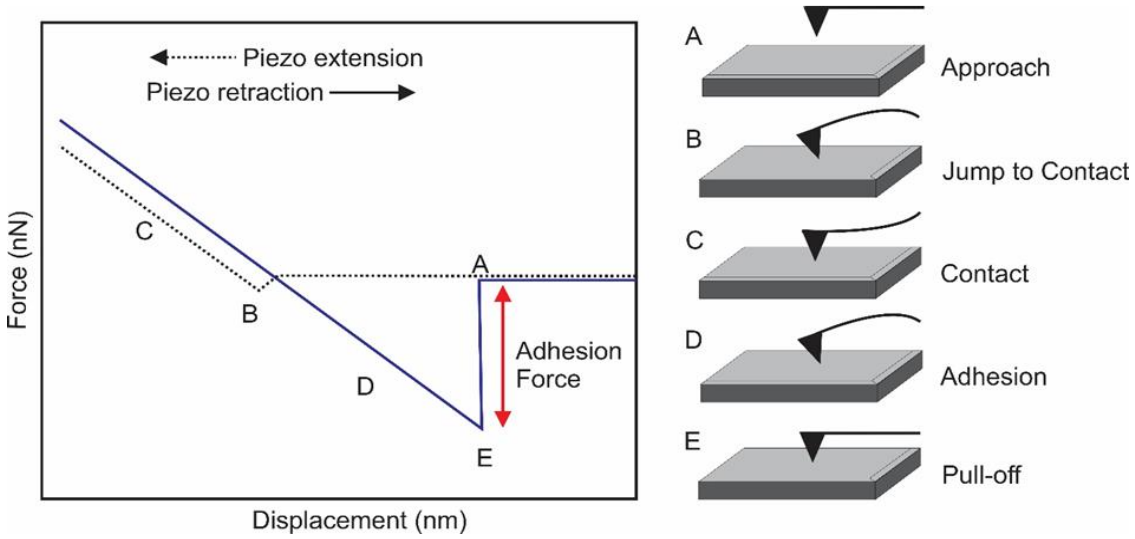


Figure 3-2 Schematic of a typical force-displacement plot with corresponding steps of force-displacement behavior (a-e)

The adhesion/pull-off force can be calculated using Hooke's law (Equation (3.1)) if the spring constant of coated cantilever is known/measured. This gives:

$$F = -kx \tag{3.1}$$

where $F$ is adhesion (pull-off) force, $k$ is the spring constant of the AFM tip and $x$ is the tip displacement. It is important to note that the stiffnesses, $k$, of coated and uncoated tips were determined experimentally using a thermal tuning method [15–17].

### 3.3 Experimental Section

#### 3.3.1 Device Fabrication

Organic-inorganic perovskite solar cells were fabricated using mesoscopic structure (glass/FTO/cTiO$_2$/mTiO$_2$/Perovskites/SpiroOMeTAD/Au), as presented in Figure 3-1 (a-b). The chemicals that were used in this work were purchased from Sigma-Aldrich (St. Louis, MO). To remove residuals, pre-etched FTO-coated (~7 Ω/sq) glass slides (MSE Supplies, AZ) were cleaned successively in Decon-90, deionized water, acetone, and isopropyl alcohol for

15 min each and treated under UV-ozone exposure (Novascan, IA, USA). A compact $TiO_2$ ($cTiO_2$) electron transport layer (ETL, thickness of ~100nm) was formed using 0.15 M and 0.3 M $TiO_2$ solutions as described elsewhere [13,18]. A mesoporous $TiO_2$ ($mTiO_2$) layer was subsequently spin coated at 4000 rpm for 30 s with titania paste in ethanol (1:5, v/v) and calcined at 500 °C for 30 min [19].

$PbI_2$ (99.999% trace metal basis) was thermally evaporated onto as-fabricated glass/FTO/$TiO_2$ substrates using a thermal evaporator (Edward, E306A, Easton PA, USA). This was done under $10^{-4}$ Torr of vacuum pressure with a deposition rate of 0.1 nm/s. The $PbI_2$ film was homogeneously transformed to $MAPbI_3$ inside low vacuum oven at 160 °C with the $PbI_2$-coated glass/FTO/$TiO_2$ placed on underlying methylammonium iodide (MAI) for 8h. The $MAPbI_3$ films were further annealed at 150°C for 10 min. For the solution-processed PSCs, a mixture of 599.3 mg $PbI_2$ in 1 ml of DMF:DMSO (9.5:0.5 of volume ratio) was spun on as-fabricated glass/FTO/$TiO_2$ substrates at 1500 rpm for 30s and was dried at 70 °C for 1 min. To obtain $MAPbI_3$ active layer, a solution of methylammonium iodide (MAI) (40 mg in 1ml of IPA) was spin coated onto $PbI_2$ layer at 1300 rpm for 30 s before annealing at 100 °C for 20 min. For FA-rich PSC, on the other hand, a formamidium (FA)-rich mixed organic cation precursor solution was prepared by mixing 60 mg FAI, 6 mg of MABr and 6 mg of MACl in 1ml of IPA. The solution was then spin coated onto on the $PbI_2$ layer at 1300 rpm, followed by annealing at 130 °C for 15 min to form FA-rich perovskite layer.

For all devices, hole transport layer (HTL) (SpiroOMeTAD) was prepared by dissolving 72 mg of SpiroOMeTAD, 17.5 μl of lithium *bis* (trifluoromethylsulphony) imide (Li-FTSI) (500mg in 1ml of acetonitrile) and 28.2 μl of 4-*tert*-butylpyridine (TBP) in 1 ml of chlorobenzene. The solution of SpiroOMeTAD was then spun at 4000 rpm at 30 s.[20] Finally, an 80 nm-thick gold (Au) (99.999%, Lesker) back contact was thermally evaporated using a thermal evaporator (Edward, E306A, Easton PA, USA) under ~$10^{-6}$ Torr vacuum pressure at 0.1 nm/s deposition rate.

### 3.3.2 AFM Pull-off Force Measurements

A graphic of an AFM set-up is displayed in Figure 3-3 (a). Pull-off forces between two materials were acquired using atomic force microscope (Park systems NX 20, Santa Clara, CA). The tip approached and contacted the surface; subsequently an attractive force was measured during the retraction phase for adhesion force between tip and substrates. This contact AFM experiments was performed in ambient environment with relative humidity of ~20-30%.

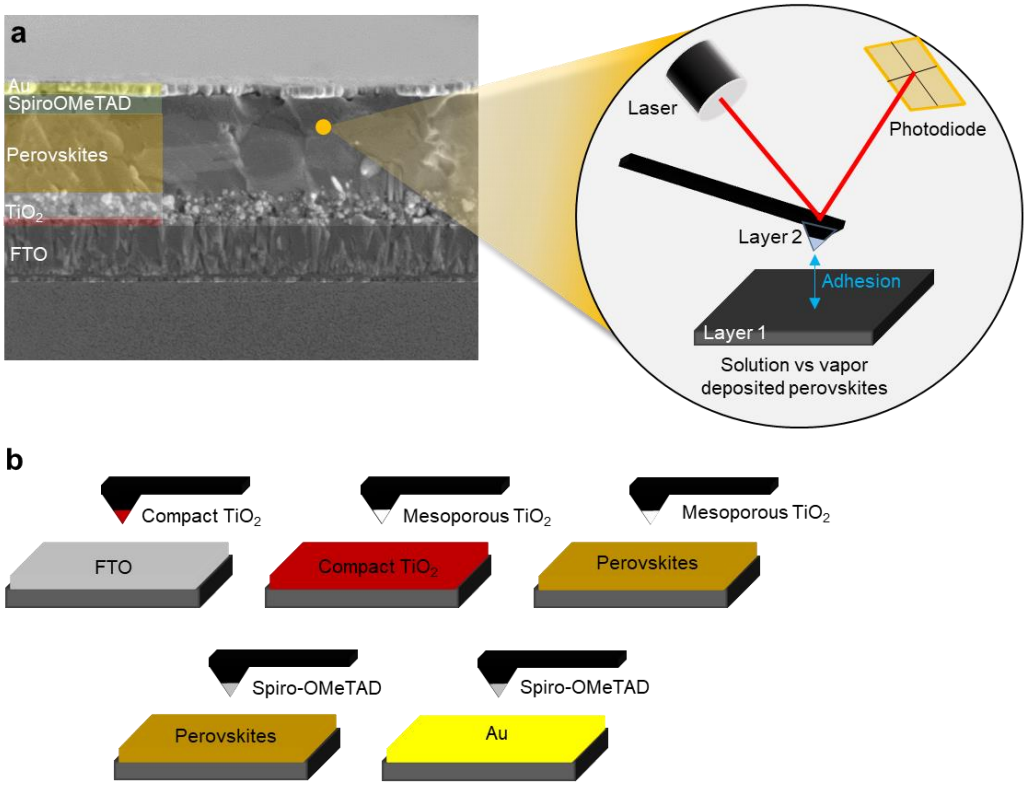


Figure 3-3 (a) Schematic for-displacement curve of AFM measurements at interest interfaces, and (b) The configurations of coatings on the AFM tips and substrates.

The contact AFM probing tips (PPP-CONTSCR 10M Park systems, Santa Clara, CA) were used in this study and these were coated with the materials that make direct contact with surfaces following the different configurations of interfaces in perovskite solar cell

structures as shown in Figure 3-3 (b). The tip were coated using a simple dip-coating technique described in prior studies [16,17] with the solution of $cTiO_2$, $mTiO_2$, and SpiroOMeTAD. The substrates were coated using the same deposition techniques that were used in device fabrication as described in section 3.3.1 Device Fabrication. Prior to force measurements, the cantilever spring constants were determined using the thermal tuning method [16]. This was used to obtain accurate measurements of the coated and uncoated AFM tips. The actual AFM tip geometries were also checked before and after the AFM measurements. This was done by observing the tips under Scanning Electron Microscopy (SEM, JEOL JSM-700F, Hollingsworth & Vose, MA, USA), operating at an accelerating voltage of 10 kV. The chemical compositions on coated tips were characterized using Energy-dispersive X-ray spectroscopy (EDS, Oxford Instruments, UK).

### 3.3.3 Surface Characterization

The surface topographies of the individual layers were characterized using AFM tapping mode. This was done using AFM tips (PPP-NCHR, Park systems, Santa Clara, CA) with nominal radii of less than 10 nm. Scanning areas of 5x5 $\mu m^2$ were used with a resolution of 256 x 256 pixels. All the measurements were carried out in air at room temperature (25 °C).

### 3.3.4 Device Characterization

To estimate photovoltaic performance, the PSCs were illuminated with a solar simulator (Oriel, Newport Corporation, Irvine, CA) that was instrumented with a source meter unit 2400 (Keithley, Tektronix, Newark, NJ). The devices were exposed to AM 1.5G illumination of 90 mW $cm^{-2}$ during the current density-voltage measurements. The solar simulator was calibrated using a calibrated silicon cell (91150 V, Newport, Irvine, CA). The current density-voltage (*J–V*) curves were obtained by scanning in the range of -0.4-1.2V, with device exposed area of 0.1 $cm^2$. The electrochemical impedance spectroscopy (EIS) characteristics of PSCs

were also studied using a potentiostat (SP-300, BioLogic Instrument) at the frequency range of 1 MHz-100 mHz.

### 3.4. Results and Discussion

#### 3.4.1 Surface and Tip Characterization

Figure 3-4 (a-h) show typical topographic AFM 2D images, while Figure 3-4 (a1-h1) present 3D images of the bare substrate FTO-coated glass, electron transport layers of $TiO_2$, SpiroOMeTAD, solution-deposited $MAPbI_3$ perovskite, solution deposited mixed-cation and mixed-anion FA-rich perovskite, vapor deposited $MAPbI_3$ perovskite, and the gold top electrode. The root-mean-squared roughness values ($R_{rms}$) obtained for the layers are summarized in Table 3.1.

Table 3.1 Root-mean-square roughness ($R_{rms}$) values of layers in PSC structures

| Layer | $R_{rms}$ (nm) |
|---|---|
| FTO-coated glass | 29.30 ± 2.25 |
| Compact $TiO_2$ | 19.82 ± 0.34 |
| Mesoporous $TiO_2$ | 23.65 ± 3.26 |
| FA-rich perovskite solution | 62.08 ± 8.38 |
| $MAPbI_3$ solution | 49.99 ± 4.21 |
| $MAPbI_3$ vapor | 27.47 ± 1.21 |
| SpiroOMeTAD | 0.56 ± 0.14 |
| Au | 10.99 ± 2.08 |

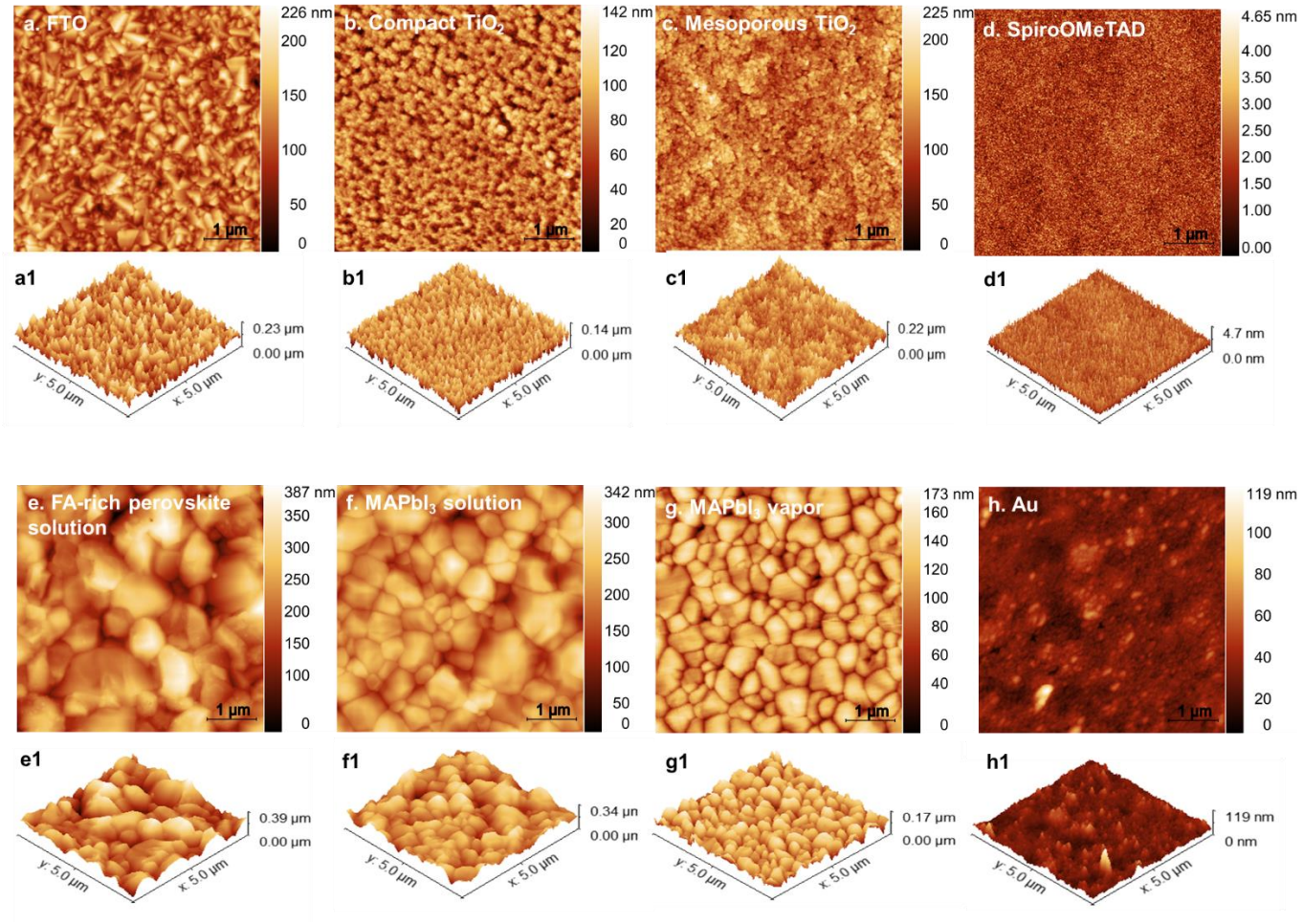


Figure 3-4 (a-h) AFM 2D topography images and (A1-H1) 3D views of the FTO, compact $TiO_2$, mesoporous $TiO_2$, SpiroOMeTAD, solution deposited mixed-cation and mixed anion FA-rich perovskite, solution deposited $MAPbI_3$ perovskite, thermally deposited $MAPbI_3$ perovskite and gold

AFM images of the perovskite films are presented in Figure 3-4 (e-g). The results show dense and closely packed grains with size of a few hundred nanometers and the grain sizes are affected by the perovskite fabrication method. The results of the vapor deposited perovskite films exhibits smaller grain sizes compared to those deposited through solution processing. 3D AFM images (Figure 3-4 (e1-g1)) suggest that the solution processed $MAPbI_3$,

and FA-rich perovskite films have rougher surfaces with respective average $R_{rms}$ values of 49.99 ± 4.21 nm and 62.08 ± 8.38 nm, compared to vapor deposited $MAPbI_3$ films with $R_{rms}$ of 27.47 ± 1.21 nm. We also observed that the surface roughness values of the films increased with increasing grain size (Figure 3-5).

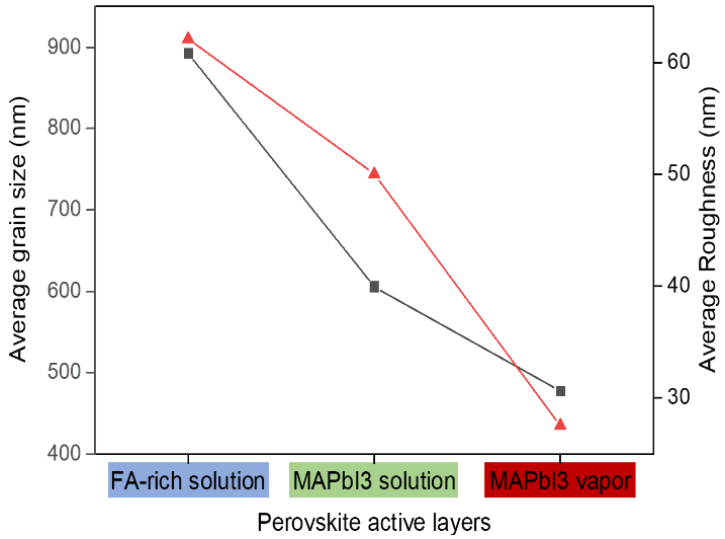


Figure 3-5 Average grain size and surface roughness ($R_{rms}$) of perovskite films

Figure 3-6 (a) presents an SEM image of a bare AFM tip, while Figure 3-6 (b-c) show the surface morphologies of AFM tips that are coated with charge transport layers of mesoporous $TiO_2$ before and after adhesion measurement. We observed that the coatings are still attached to the AFM probe tip surfaces (Figure 3-6 (c)) after pull-off force experiments. This confirms measurements of adhesive interactions between the AFM tip and substrate. Further evidence of the presence of the materials on the AFM tips is shown in Figure 3-6 (d). This shows the semi-quantitative EDS mapping results of a coated tip with hole transporting material, SpiroOMeTAD. The chemical compositions are also presented in Figure 3-6 (e) with compositions of C (49.5 %), S (44.6 %), O (1.9%) and F (0.5 %). The presence of C and F

elements are revealed the coating of SpiroOMeTAD on the AFM tips, while Si elements are from the tip itself (Figure 3-6 (f-h)).

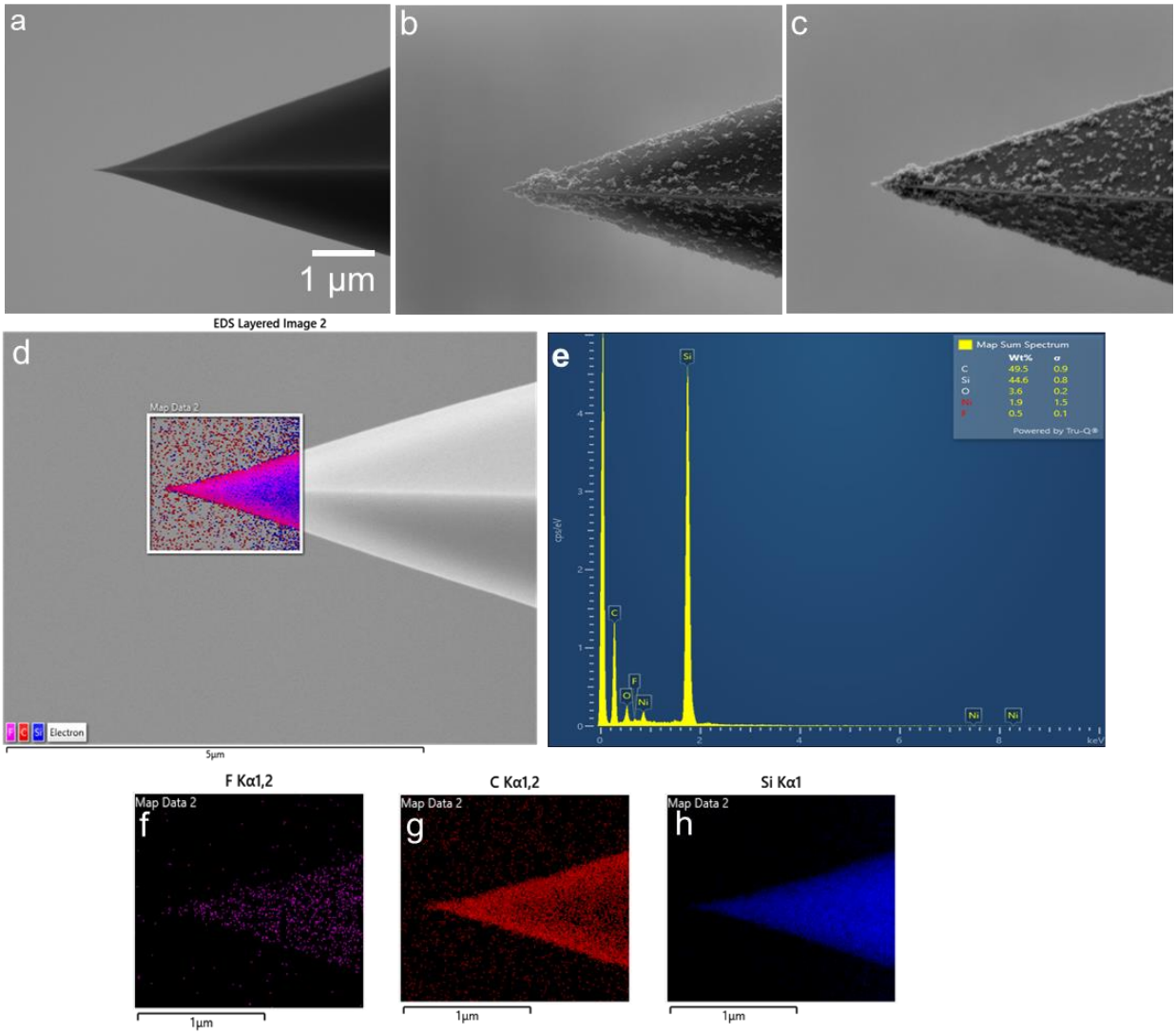


Figure 3-6 Representative profiles of tips: (a) bare tip and mesoporous $TiO_2$-coated tip before (b) and (c) after measurement. (d) Representative EDS elemental mapping of SpiroOMeTAD coated-AFM tip, (e) EDS spectrum of detected elements on the tip. Elemental mapping of (c) Fluorine, (d) Carbon, and (e) Silicon elements.

### 3.4.2 Adhesion Forces

A typical AFM force-displacement plot obtained for adhesive interaction between layers in organic-inorganic perovskite solar cells is presented in Figure 3-7. This force-displacement curve has similar characteristics to that pull-off schematic presented in Figure 3-2. The measured pull-off forces are presented in Figure 3-8. Relatively low adhesion forces were determined between FTO-coated glass and compact $TiO_2$; and SpiroOMeTAD-coated tip and gold electrode with 9.83 ± 2.63 and 24.45 ± 2.90 nN, respectively. A low adhesion force of 22.21 ± 4.81 nN was also obtained between the electron transport layer comprising compact $TiO_2$ as a blocking layer and mesoporous $TiO_2$ as a scaffold to support infiltration of perovskites.

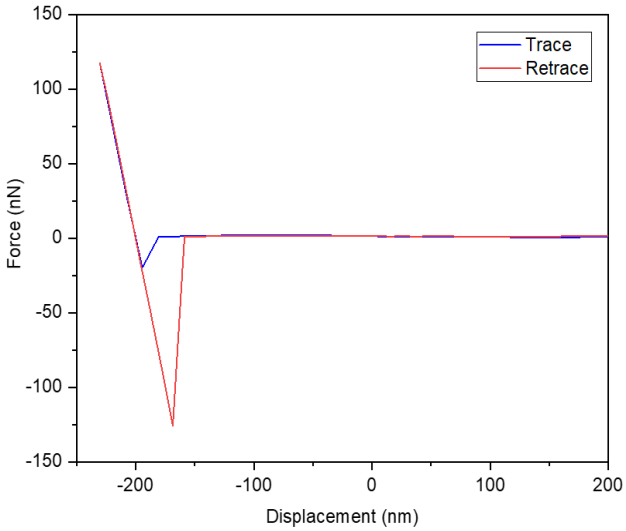


Figure 3-7 Typical AFM force-displacement behavior for SpiroOMeTAD coated tip

Charge-carrier transport layers in PSC consist of an electron transport layer (ETL) that facilitates electrons extraction and transfer from perovskite to the cathode and hole transport layer (HTL) that facilitates holes extraction and transfer from perovskites to anode [21]. Since the transport of charges across the interfaces between the perovskite and charge transport

layers are critical to collection of charges, it is important to explore the interfacial adhesion between the transport layers and the perovskite films that are processed using different processing routes. Figure 3-8 shows that the adhesive forces are higher between perovskites and adjacent mesoporous $TiO_2$ electron transport layer (ETL), for both solution-deposited perovskites ($MAPbI_3$ and FA-rich perovskite), compared to the vapor-processed perovskite. The adhesion forces between the ETL and solution-processed perovskite films are 354.30 ± 129.26 nN (FA-rich perovskites) and 268.36 ± 86.56 nN ($MAPbI_3$), while the interface between ETL and vapor-processed $MAPbI_3$ adhere only with 82.32 ± 10.05 nN. Similar trends were also observed at interfaces between perovskite thin films with the adjacent hole transport layer (HTL). The interfaces between solution-deposited perovskites and SpiroOMeTAD exhibit higher adhesive forces compared to those of vapor-deposited $MAPbI_3$/SpiroOMeTAD.

The above results suggest that the surface roughness of perovskites influences the force interactions at perovskite/ETL and perovskite/HTL interfaces. The perovskite films with rougher surfaces adhering more to the transporting layers. Also, the smoother films of $MAPbI_3$ (average grain size of ~476 nm) obtained via vapor deposition adhere less to the ETL and HTL layers, compared to the coarser films of perovskites obtained via solution deposition. It is important to note here that prior work has shown that higher surface roughness increases contact area at interface and thus improve the charge carrier collection, while producing less pronounced hysteresis within the structures [22].

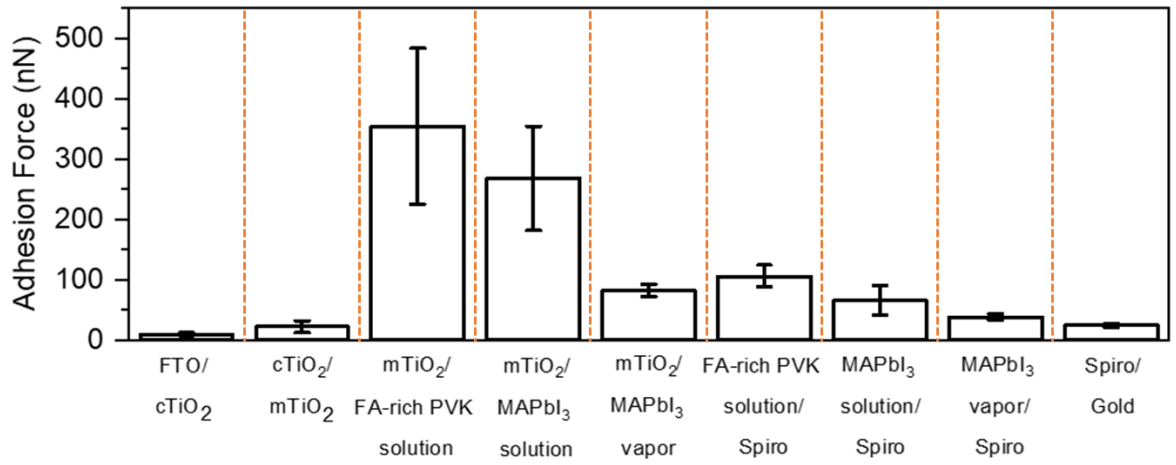


Figure 3-8 Measured adhesion forces of PSC interfaces

### 3.4.3 Correlating Adhesion Forces with Charge Transport Resistances

Electrochemical impedance spectroscopy (EIS) [23–25] was used to obtain insights into the charge carrier dynamics across the interfaces of the PSCs in this study. A semicircle from high to low frequency regions are observed for all PSC and are fitted to the appropriate equivalent circuit shown in Figure 3-9 (a) (inset). The equivalent circuit consist of series resistance $R_s$ (including the resistances from FTO and metal electrode), $R_{charge\ transfer}$ ($R_{ct}$) representing the resistance due to the interfaces between perovskites and transporting layers, and recombination resistance $R_{rec}$.[23,26] The resulting Nyquist plot (imaginary vs real part of the impedance) in Figure 3-9 (a) shows that the arc corresponding to the solution-processed perovskite devices is smaller in diameter than those of the solution-based perovskite devices. The calculated series resistance $R_s$ obtained for solution processed FA-rich and $MAPbI_3$ devices were 28.72 and 57.85 Ω, that were much lower than vapor-deposited device with 105.42 Ω. Low series resistance is highly desirable to improve the ability of charge transport to electrodes[21]. The $R_{ct}$ also exhibited the same trend, indicating lower loss of charge carrier in solution-processed PSC. This result links the lower internal resistance that comes from lower series resistance ($R_s$) to the improved charge injection that occurs at the mesoporous $TiO_2$/solution-processed perovskite interfaces. Efficient charge

transfer from perovskites to ETL results ultimately in improved solar cell performance.[27–29].

A summary of the measured adhesive forces of the interfaces in the solar cells and the fitted resistances is presented in Table 3.2. This shows that, when the adhesion forces of the solution-deposited perovskites/charge transport materials are high, then $R_s$ and $R_{ct}$ values were low. Conversely, when adhesion forces of the interfaces between the vapor deposited perovskite and charge transport layers were low, $R_s$ and $R_{ct}$ of the vapor-deposited PSC were high. Thus, the higher adhesion forces of the solution-processed perovskites and charge transporting layers give rise to more efficient charge transport in these devices, leading to an increased power conversion efficiency of solar cells. Figure 3-9 (b) presents the adhesion forces between perovskites and charge transport layers of the devices as a function of power conversion efficiency (PCE) of PSC. Consistent with the resistance of the solar cells, the vapor-deposited PSC had low PCEs of 4.77 ± 1.73 %, compared to those of solution deposited PSC with PCEs of 15.91 ± 0.92 and 12.11 ± 1.75 % for the FA-rich and $MAPbI_3$ devices. The relatively low PCE of the vapor-deposited PSC is associated with the lower adhesion forces of the perovskite/charge transport layer interfaces and the highest $R_s$ and $R_{ct}$ compared to solution processed PSC.

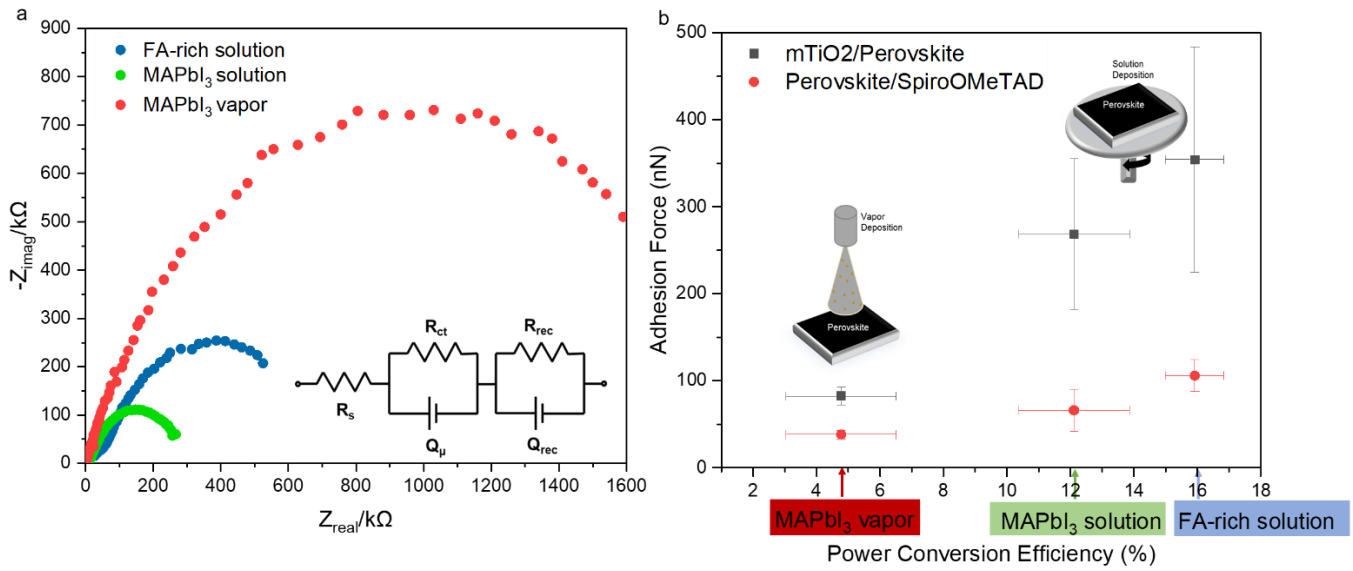


Figure 3-9 (a). Nyquist plots of impedance spectra at 0.1V of FA-rich, MAPbI3 solution and MAPbI3 vapor perovskite solar cells and circuit (inset); (b). Comparison of adhesion between perovskite and charge transport layers towards power conversion energy of solar devices

Table 3.2 Summary of adhesion forces at perovskite/charge transport layers and fitted data of representative impedance spectra

| Perovskites | Adhesion Forces (nN) | | $R_{series}$, | $R_{charge\ transfer}$, |
|---|---|---|---|---|
| | $mTiO_2$/ Perovskite | Perovskite/ SpiroOMeTAD | $R_s$ (Ω) | $R_{ct}$ (kΩ) |
| FA-rich solution | 354.30 ± 129.26 | 105.92 ± 18.32 | 28.72 | 8.76 |
| $MAPbI_3$ solution | 268.36 ± 86.56 | 65.99 ± 24.04 | 57.85 | 11.25 |
| $MAPbI_3$ vapor | 82.32 ± 10.05 | 38.36 ± 4.84 | 105.40 | 2080.00 |

### 3.4.4 Implications

The implications of the results are significant for the design of robust interfaces of multilayer perovskite solar cells. The adhesion measurements can be used to rank the most robust interfaces in PSCs. These rankings are crucial in the selection of appropriate functional layers and processing techniques for the fabrication of layers in PSCs. They can lead to improvements, not only in photovoltaic performance, but also in the reliability of multilayer perovskite solar cells.

This study also shows that the different methods that are used for the fabrication of layers in perovskite solar cells affect their surface morphologies and the adhesion of perovskite layers to adjacent layers. Strong adhesion between layers in PSCs improves the interfacial contacts that enhance the charge transport from the perovskite layer to the electrodes. Such adhesion also reduces the likelihood of interfacial cracking during solar cell operation. Thus, further improvements in interlayer adhesion could lead to production of more efficient and mechanically reliable perovskite solar cells in future. Further work is clearly needed to fabricate perovskite absorber layers using different solution processing other than spin-coating (such as spray coating, dip coating, roll-to-roll deposition) that could improve the interfacial robustness and scalability of PSCs.

## 3.5 Conclusion

This paper presents AFM technique in measuring adhesive forces of interfaces in PSC structures that are crystallized through vapor and solution routes. The interfaces that are present in model solution-processed perovskite solar cells generally exhibit higher levels of adhesion that are associated with larger perovskite grains and rougher surfaces. In general, adhesion forces at the interfaces in perovskite solar cells were below ~105 nN, except interfaces of scaffold mesoporous $TiO_2$/perovskites via solution deposition that are strongly related to perovskite infiltration into porous structures of $TiO_2$. This study also reveals the strong correlation between the adhesion of perovskites/charge transport layers and the

resistances ($R_s$ and $R_{ct}$) of PSCs. When the adhesion between the perovskite and the charge transport layers is high, $R_s$ and $R_{ct}$ of cells were found to be low. Conversely, $R_s$ and $R_{ct}$ were high when the adhesion levels between the perovskite and the charge transport layers were low. These results suggest that considerations of interfacial adhesion are needed in the development of PSCs with improved efficiencies and stability. The current study also shows that AFM technique provides a simple approach for the measurement of pull-off forces that can be used to rank the robustness of interfaces between layers in PSCs.

**References**


[1] N.R.E.L. (NREL), Best Research-Cell Efficiency Chart, (n.d.). https://www.nrel.gov/pv/cell-efficiency.html.

[2] M.I.H. Ansari, A. Qurashi, M.K. Nazeeruddin, Frontiers, opportunities, and challenges in perovskite solar cells: A critical review, J. Photochem. Photobiol. C Photochem. Rev. 35 (2018) 1–24. https://doi.org/10.1016/j.jphotochemrev.2017.11.002.

[3] G.-H. Kim, D.S. Kim, Development of perovskite solar cells with >25% conversion efficiency, Joule. 5 (2021) 1033–1035. https://doi.org/10.1016/j.joule.2021.04.008.

[4] O. V. Oyelade, O.K. Oyewole, D.O. Oyewole, S.A. Adeniji, R. Ichwani, D.M. Sanni, W.O. Soboyejo, Pressure-Assisted Fabrication of Perovskite Solar Cells, Sci. Rep. 10 (2020) 1–11. https://doi.org/10.1038/s41598-020-64090-5.

[5] Y.A. Olanrewaju, K. Orisekeh, O. V. Oyelade, R.K. Koech, R. Ichwani, A.I. Ebunu, D.I. Amune, A. Bello, V.C. Anye, O.K. Oyewole, W.O. Soboyejo, Effects of temperature-dependent burn-in decay on the performance of triple cation mixed halide perovskite solar cells, AIP Adv. 12 (2022) 015122. https://doi.org/10.1063/5.0078821.

[6] S.V.N. Pammi, V. Tran, R. Maddaka, J. Eom, J.S. Jung, H. Jeong, M. Kim, V. Pecunia, S.G. Yoon, Bromine Doping of MAPbI 3 Films Deposited via Chemical Vapor Deposition Enables Efficient and Photo-Stable Self-Powered Photodetectors, Adv. Opt. Mater. 8 (2020) 2000845. https://doi.org/10.1002/adom.202000845.

[7] S.V.N. Pammi, H.-W. Lee, J.-H. Eom, S.-G. Yoon, Predominant Stable MAPbI 3 Films Deposited via Chemical Vapor Deposition: Stability Studies in Illuminated and Darkened States Coupled with Temperature under an Open-Air Atmosphere, ACS Appl. Energy Mater. 1 (2018) 3301–3312. https://doi.org/10.1021/acsaem.8b00505.

[8] S. Bonomi, D. Marongiu, N. Sestu, M. Saba, M. Patrini, G. Bongiovanni, L. Malavasi, Novel Physical Vapor Deposition Approach to Hybrid Perovskites: Growth of MAPbI3 Thin Films by RF-Magnetron Sputtering, Sci. Rep. 8 (2018) 15388. https://doi.org/10.1038/s41598-018-33760-w.

[9] C. Ramirez, S.K. Yadavalli, H.F. Garces, Y. Zhou, N.P. Padture, Thermo-mechanical behavior of organic-inorganic halide perovskites for solar cells, Scr. Mater. 150 (2018) 36–41. https://doi.org/10.1016/j.scriptamat.2018.02.022.

[10] Z. Dai, S.K. Yadavalli, M. Chen, A. Abbaspourtamijani, Y. Qi, N.P. Padture, Interfacial toughening with self-assembled monolayers enhances perovskite solar cell reliability, Science (80-. ). 372 (2021) 618–622. https://doi.org/10.1126/science.abf5602.

[11] L.-J. Ji, S.-J. Sun, Y. Qin, K. Li, W. Li, Mechanical properties of hybrid organic-inorganic perovskites, Coord. Chem. Rev. 391 (2019) 15–29. https://doi.org/10.1016/j.ccr.2019.03.020.

[12] N. Rolston, B.L. Watson, C.D. Bailie, M.D. McGehee, J.P. Bastos, R. Gehlhaar, J.-E. Kim, D. Vak, A.T. Mallajosyula, G. Gupta, A.D. Mohite, R.H. Dauskardt, Mechanical integrity of solution-processed perovskite solar cells, Extrem. Mech. Lett. 9 (2016) 353–358. https://doi.org/10.1016/j.eml.2016.06.006.

[13] R. Ichwani, R. Koech, O.K. Oyewole, A. Huda, D.O. Oyewole, J. Cromwell, J.L. Martin, R.L. Grimm, W.O. Soboyejo, Interfacial fracture of hybrid organic–inorganic perovskite solar cells, Extrem. Mech. Lett. 50 (2022) 101515. https://doi.org/10.1016/j.eml.2021.101515.

[14] S. Hsieh, I.-T. Li, C.-W. Hsieh, M.-L. Kung, S.-L. Hsieh, D.-C. Wu, C.-H. Kuo, M.-H. Tai, H.-M. Wang, W.-J. Wu, B.-W. Yeh, Advances in cellular nanoscale force detection and manipulation, Arab. J. Chem. 12 (2019) 3163–3171. https://doi.org/10.1016/j.arabjc.2015.08.011.

[15] A. Busnaina, K. Bakhtari, J. Park, Particle Deposition and Adhesion, in: Handb. Silicon Wafer Clean. Technol., Elsevier, 2008: pp. 167–200. https://doi.org/10.1016/B978-081551554-8.50006-9.

[16] T. Tong, B. Babatope, S. Admassie, J. Meng, O. Akwogu, W. Akande, W.O. Soboyejo, Adhesion in organic electronic structures, J. Appl. Phys. 106 (2009) 083708. https://doi.org/10.1063/1.3246786.

[17] D. Yu, O.K. Oyewole, D. Kwabi, T. Tong, V.C. Anye, J. Asare, E. Rwenyagila, A. Fashina, O. Akogwu, J. Du, W.O. Soboyejo, Adhesion in flexible organic and hybrid organic/inorganic light emitting device and solar cells, J. Appl. Phys. 116 (2014) 074506. https://doi.org/10.1063/1.4892393.

[18] O. V. Oyelade, O.K. Oyewole, Y.A. Olanrewaju, R. Ichwani, R. Koech, D.O. Oyewole, S.A. Adeniji, D.M. Sanni, J. Cromwell, R.A. Ahmed, K. Orisekeh, V.C. Anye, W.O. Soboyejo, Understanding the effects of annealing temperature on the mechanical properties of layers in FAI-rich perovskite solar cells, AIP Adv. 12 (2022) 025104. https://doi.org/10.1063/5.0078558.

[19] D.O. Oyewole, R.K. Koech, R. Ichwani, R. Ahmed, J. Hinostroza Tamayo, S.A. Adeniji, J. Cromwell, E. Colin Ulloa, O.K. Oyewole, B. Agyei-Tuffour, L. V. Titova, N.A. Burnham, W.O. Soboyejo, Annealing effects on interdiffusion in layered FA-rich perovskite solar cells, AIP Adv. 11 (2021) 065327. https://doi.org/10.1063/5.0046205.

[20] R.K. Koech, R. Ichwani, J.L. Martin, D.O. Oyewole, O. V. Oyelade, Y.A. Olanrewaju, D.M. Sanni, S.A. Adeniji, R.L. Grimm, A. Bello, O.K. Oyewole, E. Ntsoenzok, W.O. Soboyejo, A study of the effects of a thermally evaporated nanoscale CsBr layer on the optoelectronic properties and stability of formamidinium-rich perovskite solar cells, AIP Adv. 11 (2021) 095112. https://doi.org/10.1063/5.0064398.

[21] A.A. Said, J. Xie, Q. Zhang, Recent Progress in Organic Electron Transport Materials in Inverted Perovskite Solar Cells, Small. 15 (2019) 1900854. https://doi.org/10.1002/smll.201900854.

[22] Z. Jehl, M. Bouttemy, D. Lincot, J.F. Guillemoles, I. Gerard, A. Etcheberry, G. Voorwinden, M. Powalla, N. Naghavi, Insights on the influence of surface roughness on photovoltaic properties of state of the art copper indium gallium diselenide thin films solar cells, J. Appl. Phys. 111 (2012) 114509. https://doi.org/10.1063/1.4721648.

[23] K. Hongsith, V. Yarangsi, S. Sucharitakul, S. Phadungdhitidhada, A. Ngamjarurojana, S. Choopun, A Multi-Electron Transporting Layer for Efficient Perovskite Solar Cells,

Coatings. 11 (2021) 1020. https://doi.org/10.3390/coatings11091020.

[24] P. Yadav, M.H. Alotaibi, N. Arora, M.I. Dar, S.M. Zakeeruddin, M. Grätzel, Influence of the Nature of A Cation on Dynamics of Charge Transfer Processes in Perovskite Solar Cells, Adv. Funct. Mater. 28 (2018) 1706073. https://doi.org/10.1002/adfm.201706073.

[25] R.K. Koech, R. Ichwani, D. Oyewole, M. Kigozi, D. Amune, D.M. Sanni, S. Adeniji, K. Oyewole, A. Bello, E. Ntsoenzok, W. Soboyejo, Tin Oxide Modified Titanium Dioxide as Electron Transport Layer in Formamidinium-Rich Perovskite Solar Cells, Energies. 14 (2021) 7870. https://doi.org/10.3390/en14237870.

[26] T. Du, N. Wang, H. Chen, H. Lin, H. He, Comparative Study of Vapor- and Solution-Crystallized Perovskite for Planar Heterojunction Solar Cells, ACS Appl. Mater. Interfaces. 7 (2015) 3382–3388. https://doi.org/10.1021/am508495r.

[27] M. Kim, B.J. Kim, J. Yoon, J. Lee, D. Suh, N. Park, M. Choi, H.S. Jung, Electro-spray deposition of a mesoporous TiO 2 charge collection layer: toward large scale and continuous production of high efficiency perovskite solar cells, Nanoscale. 7 (2015) 20725–20733. https://doi.org/10.1039/C5NR06558E.

[28] E.J. Juarez-Perez, M. Wuβler, F. Fabregat-Santiago, K. Lakus-Wollny, E. Mankel, T. Mayer, W. Jaegermann, I. Mora-Sero, Role of the Selective Contacts in the Performance of Lead Halide Perovskite Solar Cells, J. Phys. Chem. Lett. 5 (2014) 680–685. https://doi.org/10.1021/jz500059v.

[29] N. Wang, K. Zhao, T. Ding, W. Liu, A.S. Ahmed, Z. Wang, M. Tian, X.W. Sun, Q. Zhang, Improving Interfacial Charge Recombination in Planar Heterojunction Perovskite Photovoltaics with Small Molecule as Electron Transport Layer, Adv. Energy Mater. 7 (2017) 1700522. https://doi.org/10.1002/aenm.201700522.

# Chapter 4

# Interfacial Fracture of Hybrid Organic-Inorganic Perovskite Solar Cells

### 4.1 Introduction

Hybrid organic-inorganic perovskite materials have promising electro-optical properties such as broad optical absorption coefficients [1,2], long electron-hole diffusion lengths [1–3], high charge carrier mobilities [4,5], and potentially low fabrication costs [6]. They are also relatively easy to process [7]. These properties have contributed to making hybrid organic-inorganic perovskites promising candidates for next-generation, low-cost solar cell absorbers. Among organic-inorganic perovskite solar cell (PSC) materials, methyl ammonium lead iodide ($CH_3NH_3PbI_3$ or $MAPbI_3$), is used as light harvester [8–10]. It has an $ABX_3$ structure (A is organic cation, B is divalent metal cation and X is halogen ion), and can be vapor and solution processed into perovskite solar cells (PSCs)[6,11] with early 3.8% photoconversion efficiencies (PCEs) in 2009 [12], to above 25.1% in 2020 [13], which favorably compares to established photovoltaic (PV) technologies. However, their stability and durability are limited, especially when exposed to air and moisture.

In an effort to improve the stability and durability of $MAPbI_3$ perovskite solar cells, new materials compositions have emerged [14] by tuning the A-site cation of the $ABX_3$ structure with larger-ionic-radius cations, such as formamidium (FA) $[CH(NH_2)_2^+]$[15,16]. Such cation substitution has improved the optoelectronic properties of perovskite films with band gaps that are closer to the optimal bandgap of a single junction cell, longer charge-carrier lifetime and diffusion length [10]. Cation substitution further enabled PSCs with

improved thermal/phase stabilities, and device performance [17,18]. Moreover, perovskites with mixed halide compositions demonstrate attractive optical properties as the bandgap is tuned by varying the halide ion ratio (Cl:Br and Br:I)[19].

Perovskite solar cells with mixed-cations and mixed halides have attractive combinations of film quality, enhanced carrier charge transport and stability, as well as lower level of scanning electrochemical hysteresis, with PCE exceeding 25% [10,13,20]. Conversely, many multi-cation and multi-anion devices may be subjected to significant stresses such as residual stress induced crack growth device fabrication, installation, and sustained service [21], in-service thermal excursions [22], and interfacial cracking due to coefficient of thermal expansion (CTE) mismatch between layers [23]. Thus, a critical need exists for better understanding the interfacial fracture toughness as an important indicator of robust and reliable multilayer PSCs.

The stability of PSCs has been reported to be strongly related to interfacial adhesion between perovskite photoactive films and the adjacent hole and electron transporting layers [24]. Interfacial defects (in perovskite solar cells) are also detrimental to the performance of perovskite solar cells, and can lead to Ohmic contact losses and defect-induced degradation that can provide pathways for volatile compound diffusion [25]. Recent double-cantilever-beam (DCB) delamination experiments revealed the fracture resistance behavior of arrays of solution-processed $MAPbI_3$ solar cell with Gc below 1.5 J/m$^2$. Although the fracture initiates at a layer between perovskite and hole-transport-layer (HTL) interfaces due to micro-defects such as voids and cracks at the interfaces [26,27], few studies have investigated the interfacial reliability of each interfaces in perovskite multilayer devices. Therefore, a need exists for fundamental studies of interfacial fracture at each interface of the interfaces that are present in model PSCs layered structures, and such studies motivate the present work.

In this paper, Brazil-disk specimens are used to study of the mode-mixity dependence of interfacial fracture toughness, as well as the fracture/toughening mechanisms associated with interfacial fracture along the interfaces of perovskite solar cells. This study utilizes

perovskite materials that are based on solution-processed methylammonium lead iodide ($MAPbI_3$) and mixed-cations mixed-halides (FA-MA-Br-I) photoactive absorbers (FA-rich perovskite). The interfacial fracture toughness of vapor processed perovskite solar cells is also studied and compared with those of solution-processed organic-inorganic perovskite interfaces. The implications of the results are discussed for the design of robust organic-inorganic perovskite solar cells with improved resistance to interfacial fracture.

## 4.2 Experimental Section

### 4.2.1 Processing of PSCs

This study utilized mesoscopic architectures of solution- and vapor-processed organic-inorganic perovskite solar cells as illustrated in Figure 4-1 (a–c). The electron transporting layer (ETL), hole transporting layer (HTL) and the top contact electrode are identical for all the organic-inorganic perovskite solar cells, while the photoactive organic-inorganic perovskite layers were processed using different techniques/materials.

For the ETL, a compact titanium dioxide ($TiO_2$) ($cTiO_2$) layer was prepared from the solutions of 0.15 M and 0.3 M titanium diisopropoxide *bis*(acetylacetone) solution (Sigma Aldrich) in *n*-butanol. The 0.15 M solution was spin-coated onto FTO-coated glass slides that were cleaned successively in Decon-90, deionized water, acetone, and isopropyl alcohol, at 2000 rpm for 30 s. This was followed by annealing on a hot plate at 125 °C for 5 min before spin-costing the 0.3 M solution at 2000 rpm for 30 s. The films were then annealed at 500 °C for 30 min [28,29]. The mesoporous solution of titanium dioxide was prepared from titania paste (Sigma Aldrich) that was dissolved in ethanol (1:5, v/v). The solution was spin-coated at 4000 rpm for 30 s and sintered in a furnace (Lindberg Blue M, Thermo Fisher Scientific) at 500 °C for 30 min.

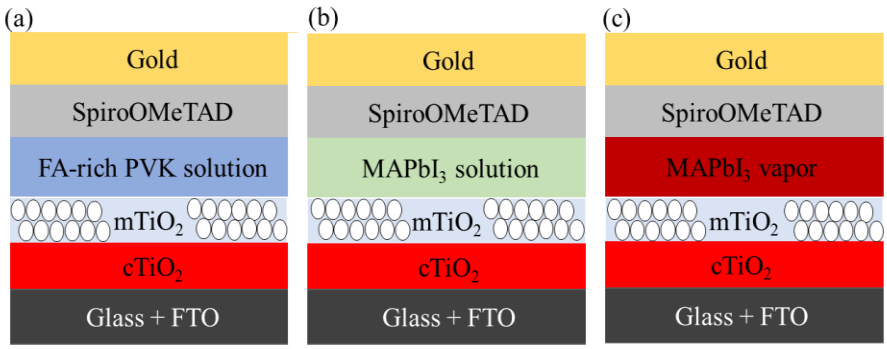


Figure 4-1 Device schematics of :(a) solution-processed organic-inorganic perovskite solar cells based on mixed-cations mixed-halides FA-rich perovskite, (b) $MAPbI_3$, and (c) vapor-processed $MAPbI_3$

Organic-inorganic perovskite layer was deposited using vapor and solution processing techniques. For the solution-processed $MAPbI_3$ and mixed-cations mixed-halides FA-rich perovskite, a two-step sequential deposition technique was used. A mixture of 599.3 mg $PbI_2$ (> 98.9% purity, Sigma Aldrich) in 1 ml of DMF:DMSO (9.5:0.5 of volume ratio) was spin-coated onto the ETL at 1500 rpm for 30s and then dried at 70 °C for 1 min before spin-coating the organic components. In the case of $MAPbI_3$, a solution of methylammonium iodide (MAI) (40 mg in 1ml of IPA) was spin coated onto $PbI_2$ layer at 1300 rpm for 30 s before annealing at 100°C for 20 min.

Formamidium (FA)-rich mixed organic cation precursor solution was prepared from a mixture of 60 mg FAI, 6 mg of MABr and 6 mg of MACl in 1ml of IPA. This was then spin coated onto on the $PbI_2$ layer at 1300 rpm to obtain FA-rich organic-inorganic perovskite before annealing at 130 °C for 15 min. In the case of vapor-deposited $MAPbI_3$, solid $PbI_2$ (Sigma Aldrich, 99.999% trace metal basis) was evaporated onto the ETL under a vacuum pressure of ~$10^4$ torr at deposition rate of 0.1 nm $s^{-1}$. The coated $PbI_2$ film was subsequently converted to methylammonium lead iodide inside low vacuum oven at 160 °C using

methylammonium iodide (MAI) (Sigma Aldrich). The films were further annealed on hot plate for 10 min at 150 °C to remove excess MAI on the film.

HTL was deposited by spin coating SpiroOMeTAD solution onto the perovskite film at 4000 rpm at 30 s. The SpiroOMeTAD solution was prepared by dissolving 72 mg of SpiroOMeTAD was dissolved in 1 ml of chlorobenzene before adding 30 μL of 4-*tert*-butylpyridine (tBP) solution and 35 μL of lithium *bis*(trifluoromethylsulphony) imide (Li-TFSI) solution (260 mg of Li-TFSI in 1 ml of acetonitrile). Finally, 80 nm thick gold was thermally evaporated using a thermal evaporator (Edwards E306A, Easton PA, USA) under a vacuum pressure of $10^{-6}$ Torr at a deposition rate of 0.1 nm $s^{-1}$, forming the back contact of the device.

### 4.2.2 Interfacial Fracture Toughness Measurements

The interfacial fracture toughness of each interface of the organic-inorganic perovskite solar cells (Figure 4-1 (a–c)) was measured using circular quartz Brazil disk specimens (Machined Ceramics, Bowling Green, KY). The Brazil disk specimen geometry was chosen because it enabled the measurement of interfacial fracture toughness over a very wide range of mode mixities between pure mode I and pure mode II. The Brazil disk geometry that we used also enabled us to introduce thin film thicknesses that mimic the actual film thicknesses in real perovskite solar cells. The circular disks had radii of 5.5 mm in radius and thicknesses of 5 mm. They also had notch radii of 1 mm radius within the specimens. One of the specimens was notched, while the other was flat as shown in Figure 4-2 (a).

To measure the interfacial fracture toughness between layers, the two layers (of two materials 1 and 2) of interest were deposited onto the notched half of the disk using the processing techniques described in Section 2.1. The second half of the was then glued to material 2 using epoxy (Epoxy Technology, Inc. Billerica, MA) and allowed to cure overnight at room-temperature (25 °C) to form a specimen in Figure 4-2 (a). It is important to note that excess epoxy was cleaned from the Brazil disk.

Brazil disks were compressed using a servo-hydraulic Instron testing machine (Instron 8872, Instron, Norwood, MA) (Figure 4-3 (a)) to measure the load-displacement curves associated with the interfacial fracture behavior of the interfaces between the layers in the Brazil disk specimens. The Instron machine was equipped with a 5 kN load cell and operated under displacement control at a cross head speed of 0.001 mm $s^{-1}$.

Loading was applied at loading angles ($\theta$) that were varied between 0° and 12°. The maximum loads corresponding to material failure were used to calculate fracture toughness value (strain energy release rate, $G$) and mode mixities using Equations (4) – (5). Figure 4-3 (a) presents images of the interfacial fracture toughness specimen before and after loading. Representative of load-displacement curves are presented in Figure 4-3 (b) – (d).

### 4.2.3 Characterization

The interfacial fracture surfaces of the layers were observed in a field-emission scanning electron microscope (SEM JEOL JSM-700F, Hollingsworth & Vose, MA) that was operated at an accelerating voltage of 10 kV. The chemical compositions associated with the fractured surfaces were characterized using Energy-dispersive X-Ray spectroscopy (EDS) (Oxford Instruments, UK). A survey of x-ray photo spectroscopy (PHI 5600 XPS system, RBD Instruments, Bend, OR) was also done for fractured interface between perovskites and SpiroOMeTAD HTL layers to further elucidate the fracture path.

The current density-voltage ($J$–$V$) characteristics of photovoltaic devices were also measured using a Keithley SMU 2400 source meter (Keithley, Tektronix, Newark, NJ, USA) that was illuminated under simulated air mass 1.5 global (AM 1.5G) solar illumination of 90 mW $cm^{-2}$ from Oriel solar simulator (Oriel, Newport Corporation, Irvine, CA). The effective exposed area of the masked cell was 0.125 $cm^2$. Also, the light intensity was calibrated using 918D high performance calibrated photodiode sensor (Newport Corporation, Irvine, CA).

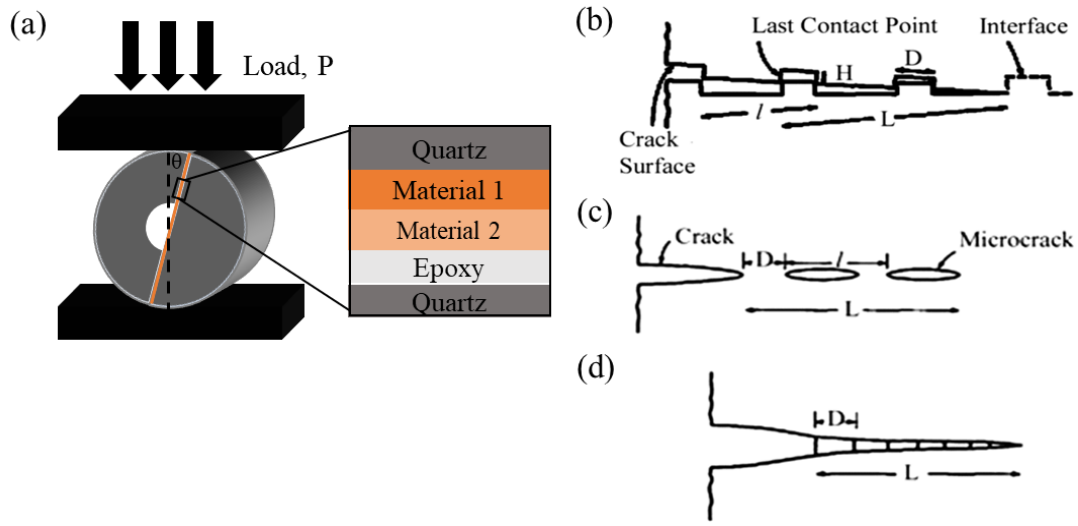


Figure 4-2 Schematics of: (a) Brazil disk specimen, (b) Crack growth in zone model, (c) Equivalent microcrack model, and (d) Idealization of crack bridging (Adapted from reference [30])

## 4.3 Theory

### 4.3.1 Crack Driving Forces and Mode Mixity

This section presents the expressions for crack driving forces, loading phases, and mode mixities associated with the Brazil disk specimens that were used in this study. The loading phase was controlled by varying the inclination angle, $\theta$ (Figure 4-2 (a)). This angle was also used to control the mode mixity, $\psi$, of the Brazil disk specimen geometry (between pure mode I and pure mode II). The stress intensity factors for modes I and II are given by Equations (4.1) and (4.2) [31].

$$K_I = f_I \sigma (\pi l)^{-1/2} \tag{4.1}$$

$$K_{II} = f_{II} \sigma (\pi l)^{-1/2} \tag{4.2}$$

In Equations (4.1)–(4.2), $l$ is the crack length, $f_I$ and $f_I$ are the non-dimensional calibration factors which a function of the loading angle, $\theta$, and relative crack length, $l/a$. Equation (4.3)

yields the stress, $\sigma$, where $F_{\max}$ is the maximum applied load to induce fracture from the compressive testing, $a$ is the disk radius and $t$ is the disk thickness.

$$\sigma = \frac{F_{\max}}{\pi a t} \tag{4.3}$$

The overall energy release rate can be calculated as in Equation (4.4) where $E^*$ is the plane strain Young's modulus for bi-material pairs [32].

$$G = G_I + G_{II} = \frac{1}{E^*}\left({K_I}^2 + {K_{II}}^2\right) \tag{4.4}$$

The mode mixities can be expressed as in Equation (4.5).

$$\psi = tan^{-1}\left(\frac{K_I}{K_{II}}\right) + \omega + \varepsilon\, ln\left(\frac{\hat{L}}{h}\right) \tag{4.5}$$

In Equation (4.5), $\hat{L}$ is a fixed length to define the loading phase and $h$ is the layer thickness. As reported by Suo *et al.*,[33] $\omega$ is the shift due to a bimaterial's elastic modulus mismatch and Dundurs Parameters, which are given by Equations (4.6)–(4.8).

$$\alpha = \frac{(1-\nu_2)/\mu_2 - (1-\nu_1)/\mu_1}{(1-\nu_2)/\mu_2 - (1-\nu_1)/\mu_1} \tag{4.6}$$

$$\beta = \frac{1}{2}\frac{(1-2\nu_2)/\mu_2 - (1-2\nu_1)/\mu_1}{(1-\nu_2)/\mu_2 - (1-\nu_1)/\mu_1} \tag{4.7}$$

$$\varepsilon = \frac{1}{2} ln \frac{(1-\beta)}{(1+\beta)} \tag{4.8}$$

### 4.3.2 Toughening Mechanisms

*Zone Shielding Model*

Evans and Hutchinson [30] introduced the dependence of interfacial fracture toughness using asperity contact models. Mixed mode, mode I (crack opening) and mode II (in-plane shear), and non-planarity of the interface are involved in the interfacial fracture problems. To estimate the interfacial fracture toughness, zone model is used in this study. This idealizes the bridged crack (Figure 4-2 (b)) as a distribution of equivalent microcracks (Figure 4-2 (c)) or equivalent bridges (Figure 4-2 (d)). As illustrated in Figure 4-2 (b), $L$ is the zone length, $H$ is the height of the interface step, $D$ is the facet length and $l$ are the facet (microcrack) center spacing. The toughening mechanism is associated with the zone that can be estimated from expressions that consider the effects of distributed microcracks and ligament bridges.

*Prediction of Critical Energy Release Rate*

The crack-tip shielding associated with the zone model of Evans and Hutchinson that can be determined from Ref. [30] to be:

$$\frac{\Delta G}{G} = \frac{tan^2\psi\left\{1-k\left[\alpha_o\left(1+tan^2\psi\right)\left(\frac{\Delta G}{G}+1\right)\right]\right\}}{1+\ tan^2\psi} \tag{4.9}$$

where the function $k(\alpha)$ in Equation (4.9) is given in Table 1 (as $1/\lambda$) in Ref. [34] and $\alpha_o$ is a material parameter that can be calculated from Equation (4.10), which gives:

$$\alpha_o = \frac{\pi E H^2/lG_o}{32(1-\nu^2)\ln\left(1/\sin\frac{\pi D}{2l}\right)} \tag{4.10}$$

As defined in Equation (4.11), a parameter $\chi$ contains basic information of contact zone dimension where large value of $\chi$ (~10) associates to maximum contact and small value of $\chi$ (~0.10) associates to lack of contact.

$$\chi = \frac{EH}{G_o} \tag{4.11}$$

In the case of large $\chi$ values, the contact forces have maximum level of crack tip shielding and $K_{II} \sim 0$. Hence, the toughening can be simplified based on the pure mode I energy release rate, $G_o$, as in Equation (4.12).

$$G = G_o\,(1 + tan^2\psi) \tag{4.12}$$

## 4.4 Results and Discussions

### 4.4.1 Interfacial Fracture Toughness

The Brazil disk specimen were placed under compression in a servo hydraulic Instron testing machine at loading angles ($\theta$) that were varied between 0° and 12° presented in Figure 4-3 (a). Figure 4-3 also included the details of specimens before and after loading. The load-displacement curves associated with the interfacial fracture behavior of the interfaces was produced and typical curves are presented in Figure 4-3 (b-d). The maximum force obtained from the load-displacement curves were then plugged into the Equation (4.1)-(4.5) to calculate the interfacial fracture toughness.

The mode mixity dependence of interfacial fracture toughness values of the interfaces that were examined in this study is presented in Figure 4-4 (a-c). Figure 4-4 (a) shows the interfacial fracture toughness values of the interfaces that are relevant to the organic-inorganic perovskite solar cell with solution-processed mixed-cations mixed-halides FA-rich perovskite as the absorber layers. These include interfaces between compact $TiO_2$ and mesoporous $TiO_2$ ($cTiO_2$/$mTiO_2$); mesoporous $TiO_2$ and solution-processed FA-rich ($mTiO_2$/FA-rich PVK); solution-processed FA-rich and SpiroOMeTAD (FA-rich PVK/SpiroOMeTAD); and SpiroOMeTAD/gold top electrodes. The results are presented for

three different loading angles (0°, 7° and 12°). They show that the interfacial toughness generally increases with increasing mode mixity.

Similar trends were observed for the interfaces in perovskite solar cells with solution-processed $MAPbI_3$ (Figure 4-4 (b)), and vapor-deposited $MAPbI_3$ (Figure 4-4 (c)) photoactive layers in which the average interfacial fracture toughness values increase with increasing mode mixity. The increase in the fracture energy, *G*, with increasing mode mixity was also associated with more tortuous crack paths, as shown schematically in Figure 4-4 (a–c).

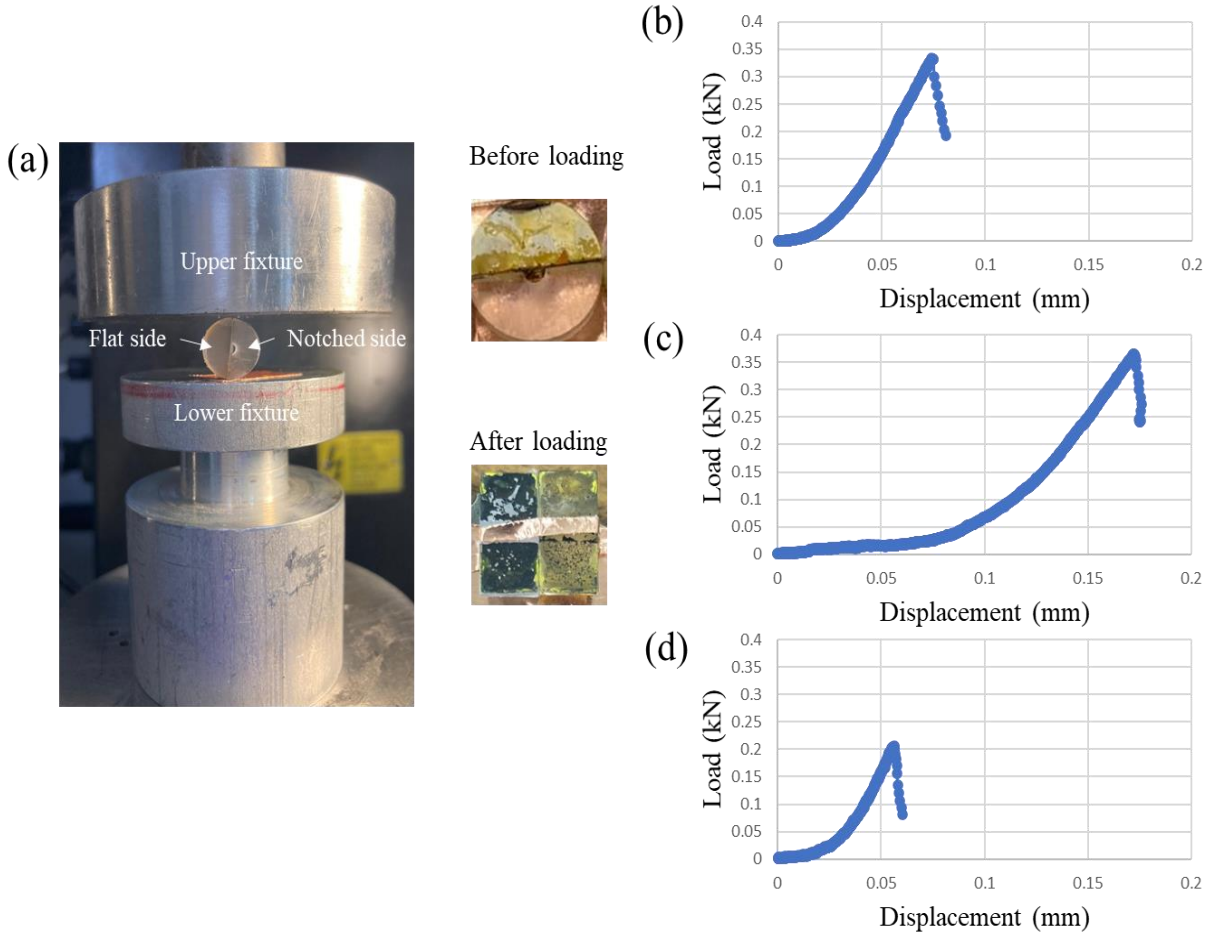


Figure 4-3 (a) The photograph of testing set up loaded in Instron Machine, Brazil disk specimen before and after loading and the representative load-displacement curves at interface between mesoporous $TiO_2$ and (a) FA-rich perovskite solution, (c) $MAPbI_3$ solution and (d) $MAPbI_3$ vapor.

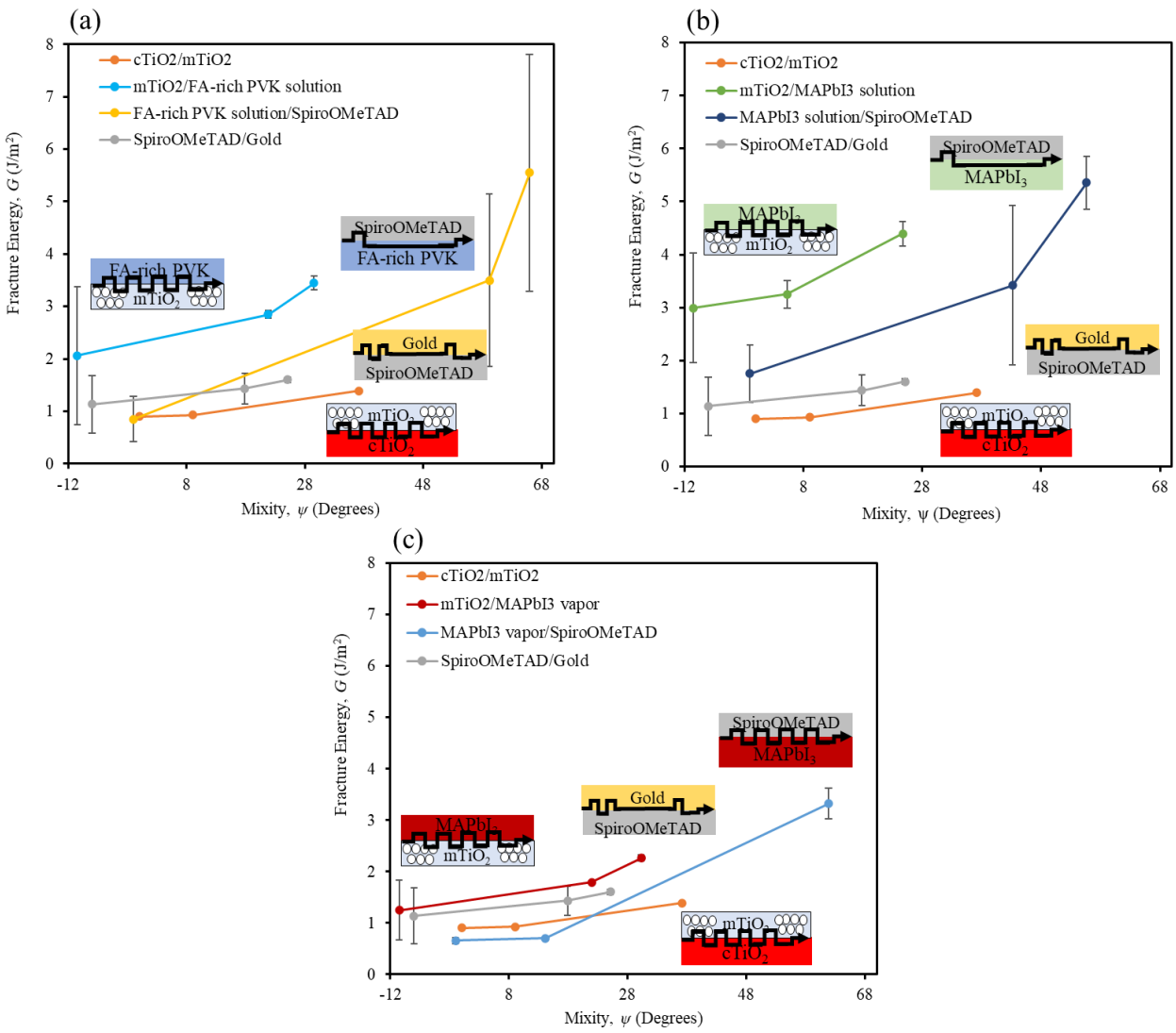


Figure 4-4 The measured average interfacial fracture toughness, *G*, as function of mode mixity for organic-inorganic perovskite solar cells structures: solution-processed FA-rich PVK (a), solution-processed $MAPbI_3$ (b), and vapor-deposited $MAPbI_3$ (c). The insets in (a–c) are the proposed interfacial mechanisms of failure path along the interfaces.

Figure 4-5 presents the effects of layer deposition methods on layer microstructure and interfacial fracture toughness. The SEM images of the top surfaces of all the hybrid organic-inorganic perovskite films in this study (Figure 4-5 (a–c)) are very uniform and

compact. As shown in Figure 4-5, solution-deposited mixed-cations mixed-halides FA-rich perovskite films (Figure 4-5 (a)) have larger grains than the both vapor and solution deposited $MAPbI_3$ organic-inorganic perovskite films (Figure 4-5 (b–c)). Solution-processed deposition promoted the formation of organic-inorganic perovskite layers with moderate/coarser grain sizes, while vapor deposition resulted in organic-inorganic perovskite layers with moderate grain sizes. The inset in Figure 4-5 (a–c) presents cross-sectional scanning electron microscopy (SEM) images of complete solar cells that comprise of glass/FTO/$cTiO_2$/$mTiO_2$/perovskites/SpiroOMeTAD/gold structures.

At a mode mixity, $\psi$ = –10.5, the interfacial fracture toughness values of ETL/Perovskite interface of the solution-processed $MAPbI_3$ PSCs were much greater than those of the $MAPbI_3$ vapor processed PSCs and the FA-rich solution processed PSCs (Figure 4-5 (d)). The increase in the interfacial fracture toughness of the solution-processed PSCs associates with the infiltration of $MAPbI_3$ perovskite within the mesoporous $TiO_2$ scaffold film during the two-step sequential deposition technique [35]. Moreover, similar trend has also been observed for the interface of Perovskite/HTL at mode mixity $\psi$ = –1.

The solution processed $MAPbI_3$ PSCs had higher interfacial fracture toughness values at both of ETL/perovskite and perovskite/HTL interfaces (Figure 4-5 (d–e)). These had interfacial fracture energies of 2.99 ± 1.03 J/m$^2$ and 1.75 ± 0.54 J/m$^2$, respectively. The latter value is similar to the reported interfacial fracture energy of 1.61 ± 0.54 J/m$^2$ for solution processed $MAPbI_3$/SpiroOMeTAD by Lee *et al*. [36] In the case of perovskite/HTL interface, vapor-deposited $MAPbI_3$ had the weakest interface with an interfacial fracture toughness, $G$ of 0.65 ± 0.06 J/m$^2$ that was about half of the fracture energy of the $MAPbI_3$ solution/SpiroOMeTAD interface.

The interfacial fracture toughness is influenced by bigger grain sizes and rougher surfaces of solution-processed perovskites compared to that of vapor-deposited perovskite. The comparison of AFM images the perovskite films are shown in Figure 4-5 while the roughness values are summarized in Table 4.1. Roughness is associated to the mechanism

that prevents separation from occurring completely along the interface line. Adjacent layers tend to fill up the rough and pointed surfaces of perovskite, leading to higher interfacial fracture toughness due to mechanical interlocking that make the adjacent layers difficult to fully delaminate from the perovskite layer. Other reports also been observed that rough surfaces lead to cohesive failure that contributes to enhanced interfacial adhesion [36,37].

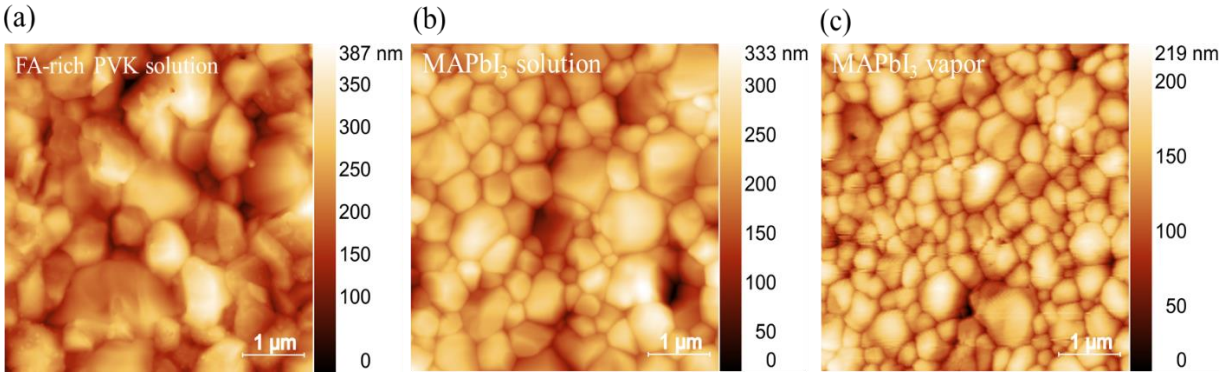


Figure 4-5 AFM images of perovskite active layers: (a). FA-rich perovskite, (b) $MAPbI_3$ solution, and (c) $MAPbI_3$ vapor

Table 4.1 Surface roughness of perovskite active layers

| Perovskites | Roughness (nm) |
|---|---|
| FA-rich solution | 62.08 ± 8.38 |
| $MAPbI_3$ solution | 49.99 ± 4.21 |
| $MAPbI_3$ vapor | 23.65 ± 3.26 |

### 4.4.2 Solar Cell Performance and Interfacial Fracture Toughness

We measured the current density-voltage *J-V* characteristics of the solar cells under AM 1.5G solar irradiation. Figure 4-6 (f) shows the best *J-V* curves measured for PSCs with active

layers of FA-rich perovskites solution processing, $MAPbI_3$ solution-processing, and $MAPbI_3$ vapor deposition. Mixed-cations mixed-halides FA-rich organic-inorganic perovskite solar cells had higher current densities than $MAPbI_3$ solution- and vapor-processed solar cells. This was associated with larger grain sizes in the FA-rich organic-inorganic perovskite solar cell that had a power conversion efficiency of FA-rich PSCs, yielding ~16.18 ± 0.28 %.

The results (Figure 4-6 (a-f)) suggests that there is a trade-off between the measured interfacial fracture resistance and photovoltaic performances. Hence, although the mixed-cation and mixed-halides FA-rich organic-inorganic perovskite PSCs yielded the highest power conversion efficiency (PCE) among the PSCs examined in this study, the fracture resistance at interfaces between perovskite photoactive films and the adjacent hole and electron transporting layers were lower than those obtained from the solution-processed $MAPbI_3$ solar cell structures.

Conversely, the average PCEs of the solar cells with solution processed $MAPbI_3$ active layers was ~10.03 ± 1.64 %. The improved performance of the solution-processed $MAPbI_3$ solar cell was also associated with the higher interfacial fracture toughness between the organic-inorganic perovskite films and the adjacent hole and electron transport layers (HTLs/ETLs). Vapor-deposited $MAPbI_3$ solar cells had relatively low average PCE of ~4.19 ± 0.20 %. These are associated with the small grain sizes ad low interfacial fracture toughness between absorber layer to the transporting layer.

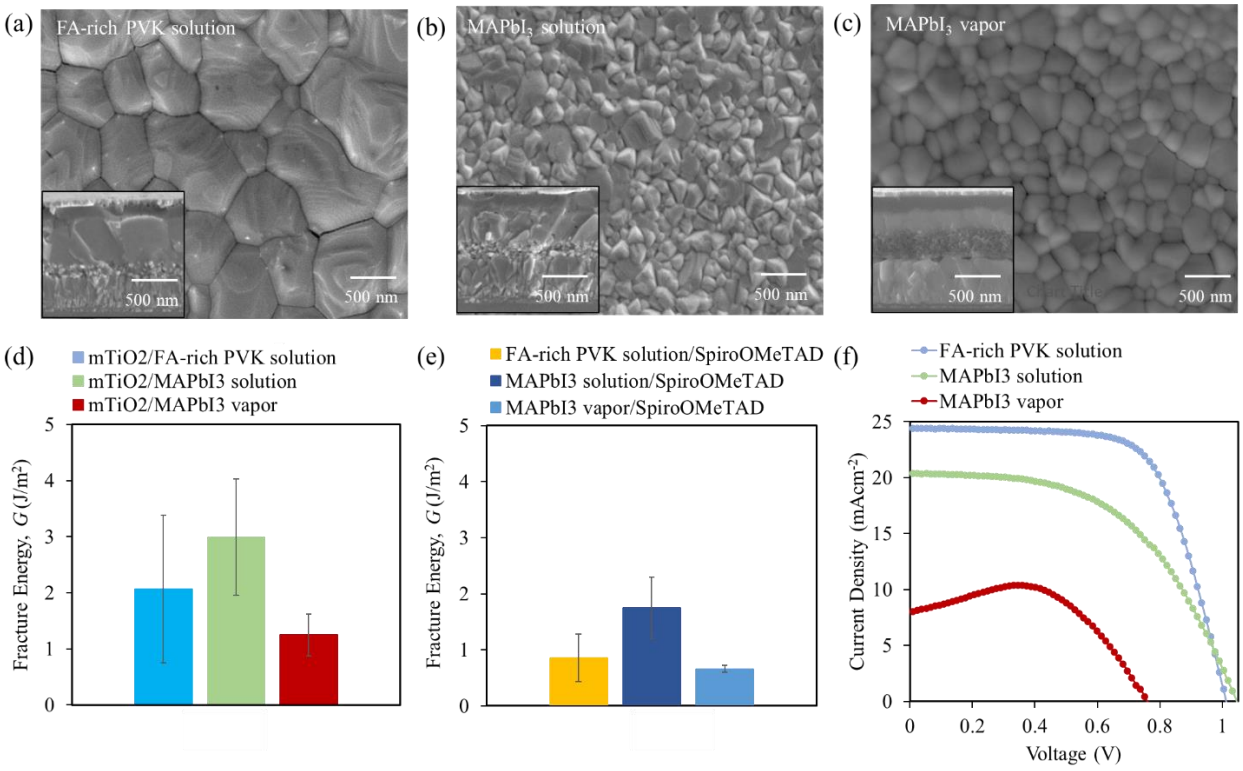


Figure 4-6 (a–c) Top surface morphology and cross-section view (inset) of FA-rich solution, $MAPbI_3$ solution, and $MAPbI_3$ vapor organic-inorganic perovskites active layer. (d) Average $G$ of ETL/Perovskite interfaces at $\psi$ = –10.5 for all PSCs. (e) Average $G$ of Perovskite/HTL interfaces at $\psi$ = –1 for all PSCs. (f) The best $J$–$V$ characteristics of all perovskites solar cells.

### 4.4.3. Fracture and Toughening Mechanisms

Figure 4-7 (a) shows the schematic of Brazil disk testing for SpiroOMeTAD/gold interface. SEM images and EDS elemental analysis of the representative fracture surfaces of the SpiroOMeTAD/gold interface are presented in Figure 4-7 (b-c). The SEM images of the surface of upper surface (side 1) (Figure 4-7 (b)) revealed a matching morphology with the bottom surface (side 2) (Figure 4-7 (c)). The EDS results also show that a region of the gold layer was delaminated onto upper disk, leaving SpiroOMeTAD on the notched disk. The cross-sectional EDS maps of the fractured disk also provide additional insights into the

fracture and toughening mechanisms (Figure 4-8). These include the evidence of crack kinking in-and-out of the SpiroOMeTAD/gold interfaces during the initial stages of cracking.

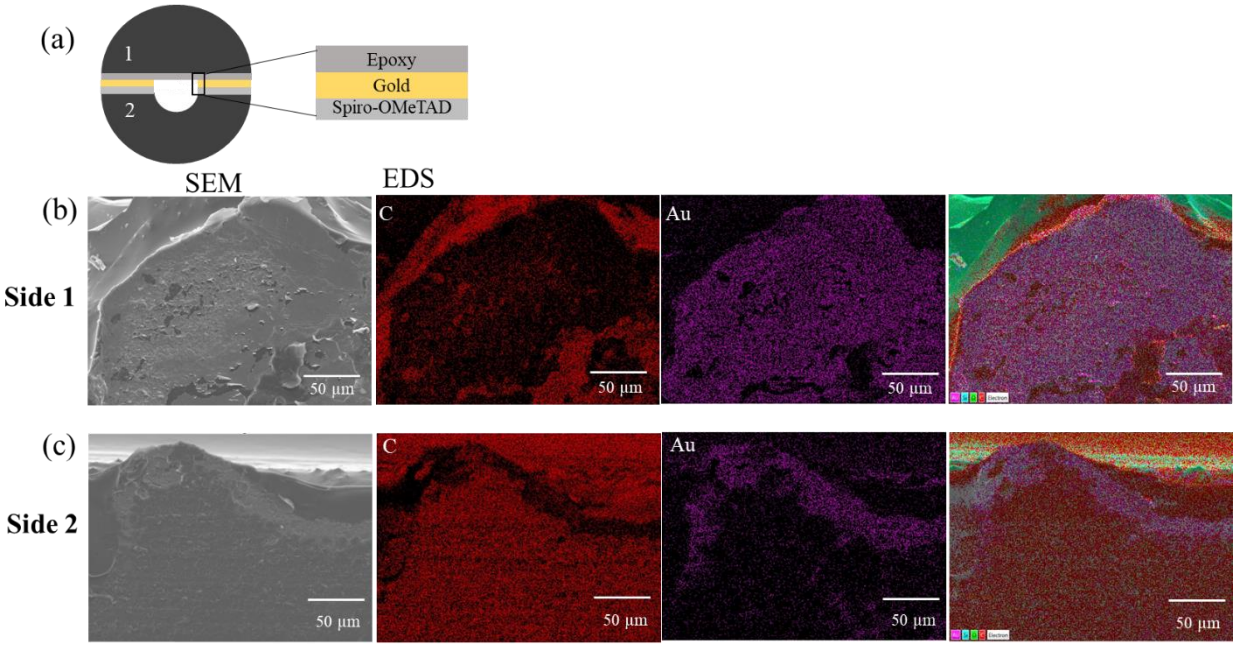


Figure 4-7 (a) Schematic of SpiroOMeTAD/gold Brazil disk specimen. Representative of associated EDS elemental maps of the pairing fractured disk in the same area; (b) Upper half disk (Side 1), (c) bottom half disk (Side 2).

X-ray photoelectron spectroscopy (XPS) and energy-dispersive spectroscopy (EDS) confirmed the chemical compositions on either side of the Brazil disks. They also further elucidate the failure mechanisms along the interfaces between the perovskites and the HTL. Figure 4-9 presents high-resolution N 1s and Pb 4f regions of the XP spectra as respective proxies for the SpiroOMeTAD and for the perovskite itself, with wide-area survey scans of each surface available in Figure 4-10.

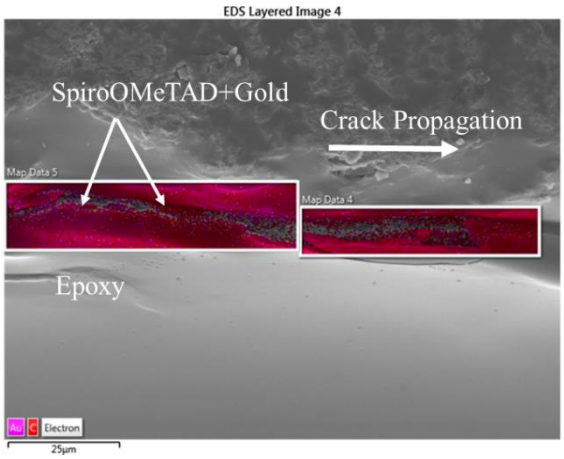


Figure 4-8 Cross-sectional EDS maps of SpiroOMeTAD/gold interface, indicating failure kinking in-and-out of SpiroOMeTAD/gold interface.

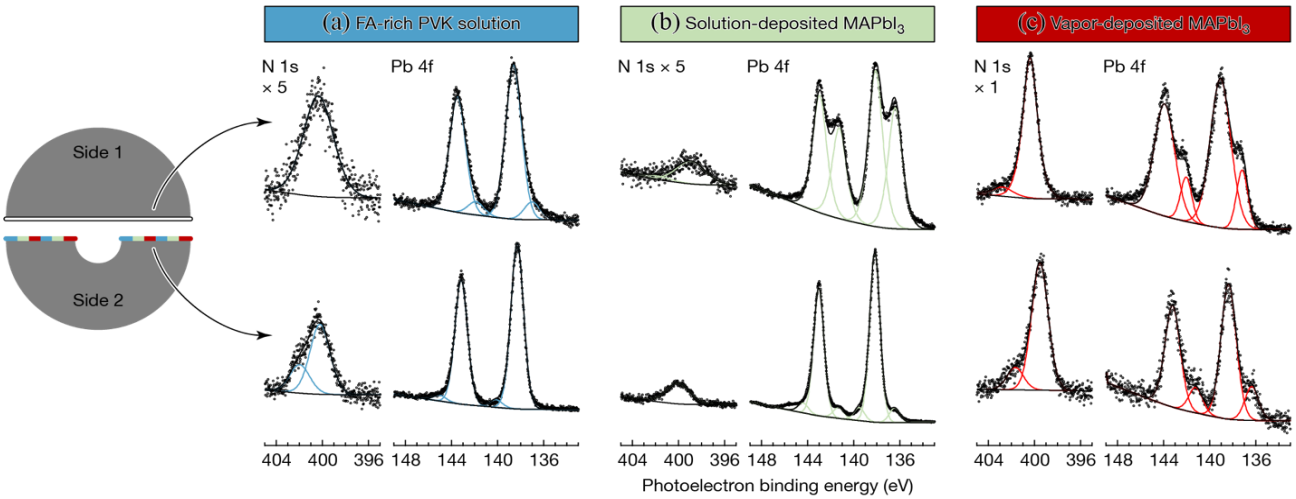


Figure 4-9 XP spectra of pairing fractured surfaces of perovskite/HTL in the same area for solution-processed FA-rich PVK (a), solution-processed $MAPbI_3$ (b), and vapor-deposited $MAPbI_3$ (c)

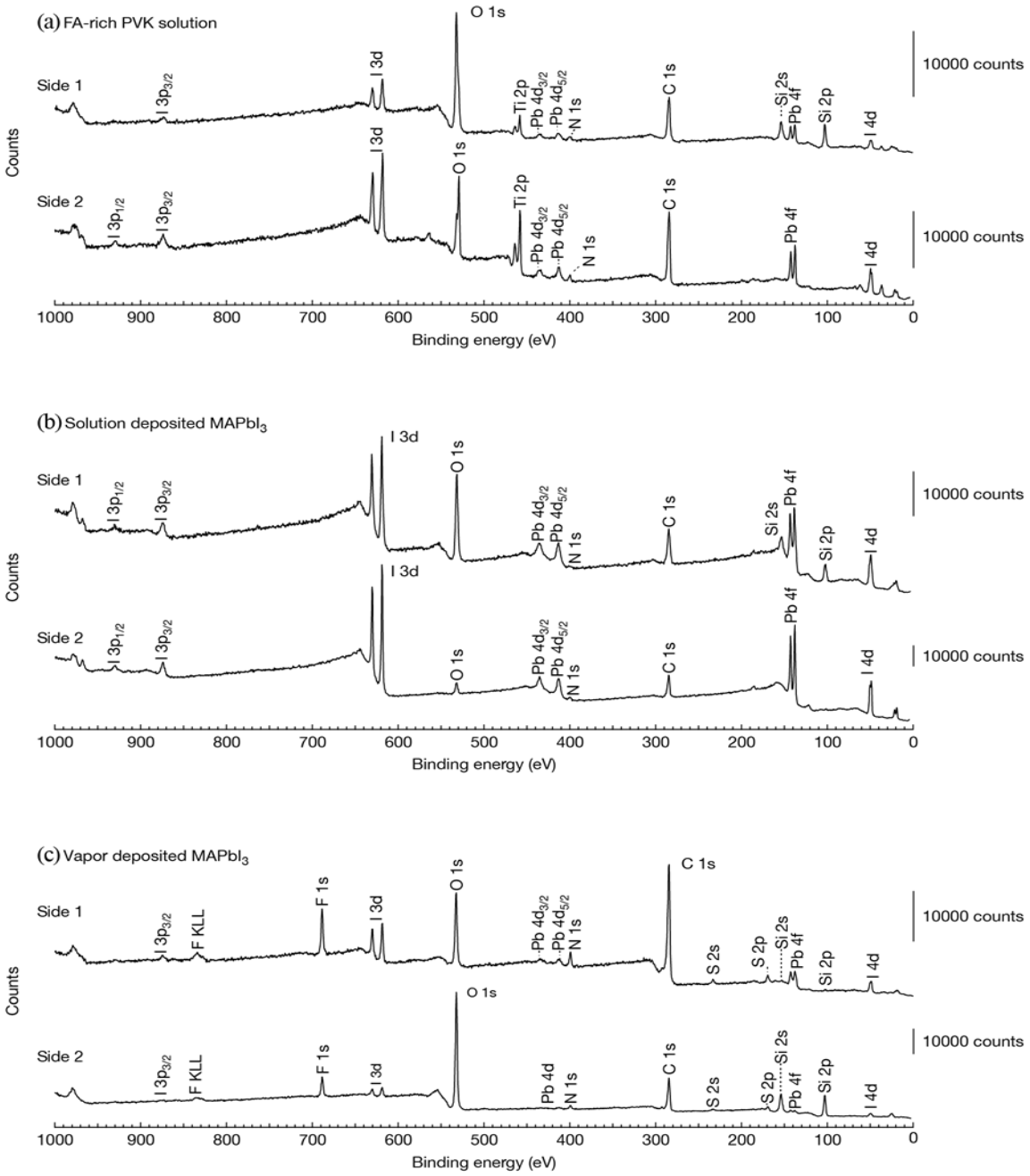


Figure 4-10 XP spectra survey scans of pairing fractured surfaces of perovskite/HTL in the same area for solution-processed FA-rich PVK (a), solution-processed $MAPbI_3$ (b), and vapor-deposited $MAPbI_3$ (c)

Figure 4-9 (a–c) presents the XP spectra of the two halves for solution FA-rich perovskite (Figure 4-9 (a)), solution $MAPbI_3$ (Figure 4-9 (b)) and vapor $MAPbI_3$ (Figure 4-9 (c)). We interpret the presence of both N 1s and Pb 4f on the two halves is evidence of kinks in and out of the interfacial crack along the interface. The results show that the intensity of N 1s in the XP spectra of vapor deposited $MAPbI_3$ solar cells (Figure 4-9 (a)) dominates Pb 4f, which may be associated with dominant kinking of cracks towards the SpiroOMeTAD film. A representative survey of the scanned fractured surface is presented in Figure 4-10, while Figure 4-11 shows further detailed of EDS elemental scanning at interface of vapor deposited $MAPbI_3$/HTL. Traces of I and Pb elements in EDS images correspond to fractured specimens on both sides, which demonstrate crack kinking in-and-out mechanism at interfaces. In the case of solution processed $MAPbI_3$ and FA-rich perovskite (Figure 4-9 (b-c)), Pb 4f relatively dominated the fractured surfaces. The dominance of Pb 4f demonstrates that the fractures mostly occur along perovskite layers. It is due to the deeply penetrated SpiroOMeTAD on rough and pointed perovskite surfaces resulting in enhanced fracture toughness [36].

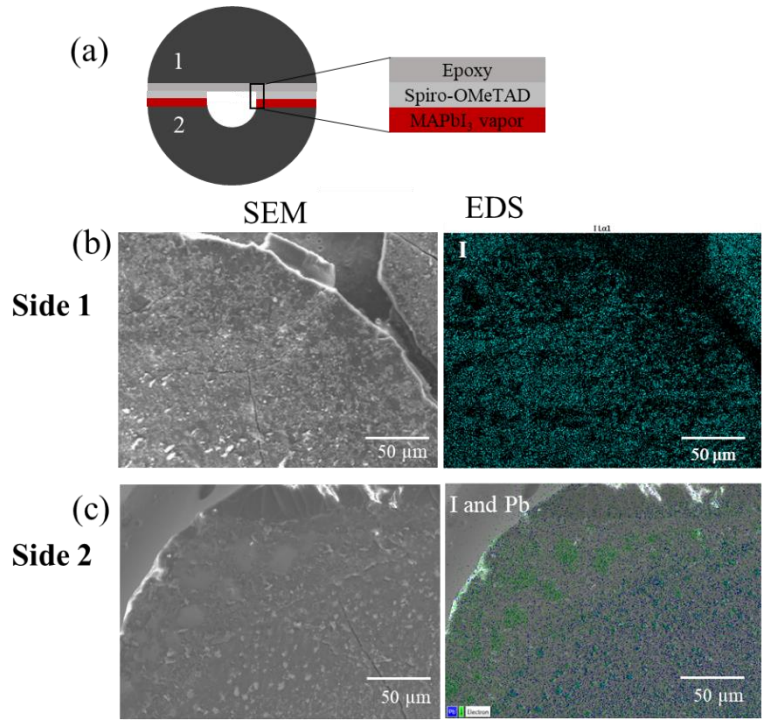


Figure 4-11 (a) Schematic of $MAPbI_3$ vapor/spiroOMeTAD Brazil disk specimen. Representative of SEM images and associated EDS elemental maps of the pairing fractured disk in the same area; (b) Upper half disk (Side 1), (c) bottom half disk (Side 2).

In the case interface between perovskite and electron transport layer, the representative EDS images that characterized the pairing fracture modes of perovskite/charge transport layers are also presented in Figure 4-12. The overall characterized fractured surfaces correspond to the failure path at perovskite/HTL interfaces. The kinking in-and-out mechanism is typically observed along the interfaces of most of the bi-material.

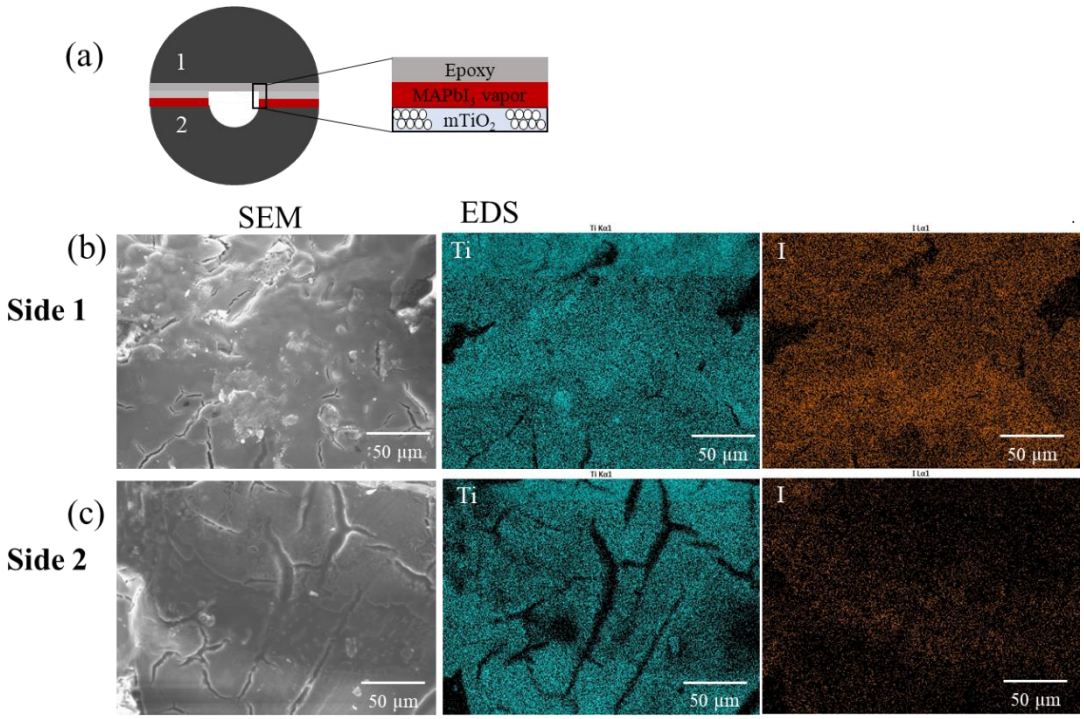


Figure 4-12 (a) Schematic of $mTiO_2$/$MAPbI_3$ vapor Brazil disk specimen. Representative of SEM images and associated EDS elemental maps of the pairing fractured disk in the same area; (b) Upper half disk (Side 1), (c) bottom half disk (Side 2)

Cross-sectional SEM images of the crack profiles along the different interfaces revealed the toughening. Figure 4-13 (a–d) demonstrates the cross-sectional SEM images of the crack profiles for interfaces between: (a) $mTiO_2$ and solution-processed $MAPbI_3$ perovskite; (b) SpiroOMeTAD and Gold; (c) $mTiO_2$ and vapor-processed $MAPbI_3$ perovskite, and (d) solution-processed mixed-cations mixed-halides FA-rich perovskite and SpiroOMeTAD. All the images reveal evidence of kinking in-and-out of interfaces, with evidence of bridging by uncracked ligaments. These result in crack-tip shielding and toughening by crack bridging. The observed shielding was modeled using the zone model [12] and parameters summarized in Table 4.2.

Table 4.2 Basic material properties used in zone model predictions.[28]

| Materials | Young's Modulus (GPa) | Poisson Ratio | Shear Modulus (GPa)[a] |
|---|---|---|---|
| $TiO_2$ | 210 | 0.3 | 80.76 |
| Perovskites | 19.77 | 0.33 | 22.55 |
| SpiroOMeTAD | 15 | 0.36 | 5.51 |
| Au | 78 | 0.48 | 26.35 |

[a]Shear modulus is obtained from $G=0.5[E/(1+\upsilon)]$

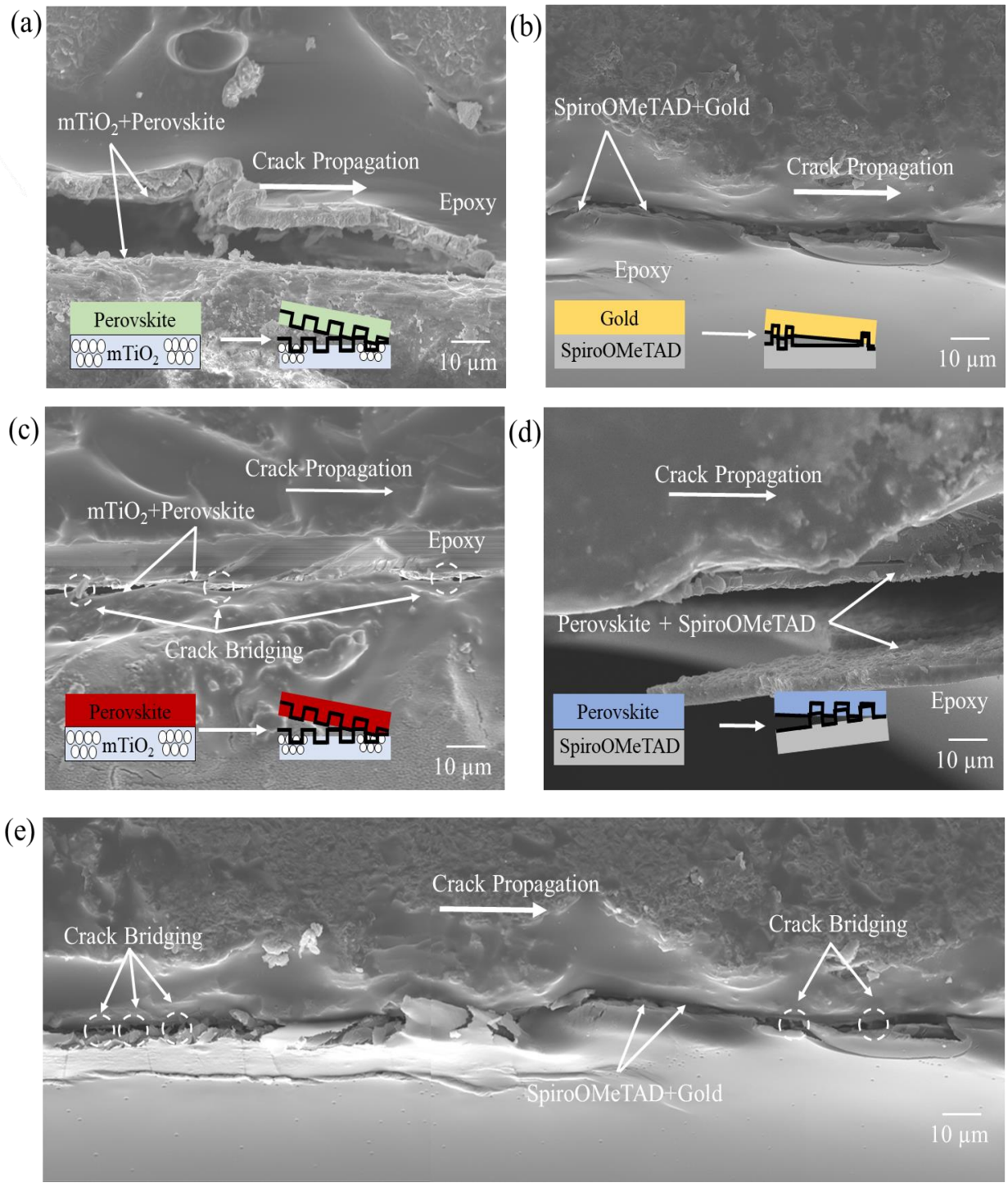


Figure 4-13 Representative cross-sectional SEM images of fractured Brazil disks for interfaces between: (a) $mTiO_2$ and solution processed $MAPbI_3$ solution; (b) SpiroOMeTAD and Gold; (c) $mTiO_2$ and vapor processed $MAPbI_3$, (d) solution processed FA-rich perovskite and SpiroOMeTAD, and (e) Bridging in interfaces of SpiroOMeTAD and Gold

The predicted interfacial fracture toughness vales obtained from the zone shielding model are compared with the measured interfacial fracture toughness values in Figure 4-14 (a–c). These show clearly that the zone shielding model predict the trends in the measured interfacial toughness values over the range of mode mixities that was examined in this study. This was in agreement for ETL/Perovskite (Figure 4-14 (a)), HTL/Perovskite (Figure 4-14 (b)), $cTiO_2/mTiO_2$ and SpiroOMeTAD/gold (Figure 4-14 (c)). This suggests that the observed toughening due to crack bridging and kinking in-and-out of interfaces can be used to estimate the overall toughening along the different interfaces that are relevant to the organic-inorganic perovskite solar cells that were examined in this study. The overall fracture toughness at a given mode mixity was also estimated from the sum of the initiation toughness and the predicted toughening at that mode mixity.

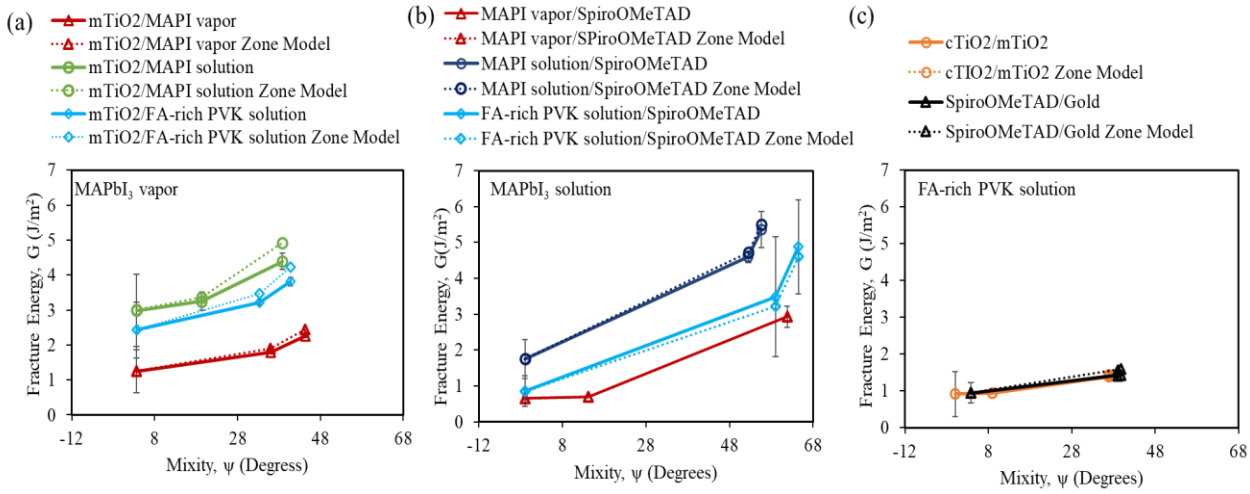


Figure 4-14 Comparison of measured and predicted interfacial fracture toughness of ETL/Perovskite (a), HTL/Perovskite (b), $cTiO_2/mTiO_2$ and SpiroOMeTAD/gold (c) interfaces.

### 4.4.4 Implications

The implications of the current results are significant for the design of robust interfaces in hybrid organic-inorganic perovskite solar cells. First, the current results show that the processing methods have a significant effect on layer microstructures and surface morphologies, which in turn affect the initiation fracture toughness values and the overall crack-tip shielding levels that can occur during interfacial crack growth across interfaces that are relevant to hybrid organic-inorganic perovskite solar cells.

Trade-offs were also observed with larger perovskite grains resulting in lower interfacial fracture toughness and improved solar cell performance and vice-versa. Thus, higher solar cell PCEs were observed in PSCs with solution-processed perovskites active layer, while PSCs with vapor-deposited organic-inorganic perovskite layers with smaller grain sizes had the lower solar cell performance and interfacial fracture toughness values, for the interfaces between the organic-inorganic perovskite and the ETL/HTL layers.

Thus, a combination of processing and microstructure control can be used to engineer the solar cell performance characteristics (photoconversion efficiencies, short circuit currents and open circuit voltages) of hybrid organic-inorganic perovskite solar cells. Furthermore, the kinking in-and-out of the interfaces between the different layers has a significant effect on the crack-tip shielding that can occur due to crack bridging and microcracking within the context of the zone shielding model developed by Evans and Hutchinson [31]. This was found to predict the trends in the measured interfacial fracture toughness values over the range of mode mixities that was examined in this study.

Finally, it is important to note that this study provides useful quantitative measurements of interfacial fracture toughness measurements for the ranking of interfacial robustness. The measured interfacial fracture toughness values also provide useful measurements that can be incorporated into simulations of crack growth along the interfaces of model perovskite solar cell structures. These are being developed for potential applications in rigid or flexible solar cells in which the layers and interfaces (within the solar

cells may) be subjected to axial and/or in-plane shear stresses under the mixed-mode loading conditions that were considered in this study. However, there is a need to consider the possible effects of sub-critical interfacial cracking that can occur at crack driving forces that are below those required for failure under monotonic loading. These are clearly some of the challenges for future work.

### 4.5. Conclusion

This paper presents the results of a study of the effects of processing on the microstructure and mode mixity-dependence of the interfacial resistance of organic-inorganic perovskite solar cells. Salient conclusions arising from this study are presented below. First, vapor deposition results in organic-inorganic perovskite layers with smaller grain sizes, while solid solution processing is shown to promote the formation of organic-inorganic perovskite layers with moderate/coarser grain sizes. Second, the vapor-deposited perovskite layers result in lower interfacial fracture toughness, while the coarser solution-processed organic-inorganic perovskite layers are shown to result in improved interfacial fracture toughness values, for interfaces between perovskite and the ETL/HTL layers. Third, in the case of the solution processed perovskites, larger grain sizes of perovskite layers results in lower interfacial fracture toughness and improve solar cell performance. Finally, the mechanism of interfacial fracture is associated with kinking in-and-out of interfaces in all cases. This results in crack-tip shielding by crack bridging, which was modeled using a zone shielding model that predicted the measured interfacial fracture toughness over the range of mode mixities that was explored in this study. The measured interfacial fracture toughness values can be used to evaluate the interfacial robustness of organic-inorganic perovskite solar cells. They may also be used in fracture mechanics simulations of interfacial cracking in organic-inorganic perovskite solar cells with flexible or rigid substrates.

**References**


[1] D. Shi, V. Adinolfi, R. Comin, M. Yuan, E. Alarousu, A. Buin, Y. Chen, S. Hoogland, A. Rothenberger, K. Katsiev, Y. Losovyj, X. Zhang, P.A. Dowben, O.F. Mohammed, E.H. Sargent, O.M. Bakr, Low trap-state density and long carrier diffusion in organolead trihalide perovskite single crystals, Science (80-. ). 347 (2015) 519–522. https://doi.org/10.1126/science.aaa2725.

[2] G. Xing, N. Mathews, S. Sun, S.S. Lim, Y.M. Lam, M. Gratzel, S. Mhaisalkar, T.C. Sum, Long-Range Balanced Electron- and Hole-Transport Lengths in Organic-Inorganic CH3NH3PbI3, Science (80-. ). 342 (2013) 344–347. https://doi.org/10.1126/science.1243167.

[3] S.D. Stranks, G.E. Eperon, G. Grancini, C. Menelaou, M.J.P. Alcocer, T. Leijtens, L.M. Herz, A. Petrozza, H.J. Snaith, Electron-Hole Diffusion Lengths Exceeding 1 Micrometer in an Organometal Trihalide Perovskite Absorber, Science (80-. ). 342 (2013) 341–344. https://doi.org/10.1126/science.1243982.

[4] B. Conings, J. Drijkoningen, N. Gauquelin, A. Babayigit, J.D. Haen, L.D. Olieslaeger, A. Ethirajan, J. Verbeeck, J. Manca, E. Mosconi, F. De Angelis, H. Boyen, Intrinsic Thermal Instability of Methylammonium Lead Trihalide Perovskite, (2020) 1–8. https://doi.org/10.1002/aenm.201500477.

[5] C. Wehrenfennig, G.E. Eperon, M.B. Johnston, H.J. Snaith, L.M. Herz, High Charge Carrier Mobilities and Lifetimes in Organolead Trihalide Perovskites, Adv. Mater. 26 (2014) 1584–1589. https://doi.org/10.1002/adma.201305172.

[6] Z. Wang, D.P. McMeekin, N. Sakai, S. van Reenen, K. Wojciechowski, J.B. Patel, M.B. Johnston, H.J. Snaith, Efficient and Air-Stable Mixed-Cation Lead Mixed-Halide Perovskite Solar Cells with n-Doped Organic Electron Extraction Layers, Adv. Mater. 29 (2017) 1604186. https://doi.org/10.1002/adma.201604186.

[7] L. Meng, J. You, Y. Yang, Addressing the stability issue of perovskite solar cells for commercial applications, Nat. Commun. 9 (2018) 5265. https://doi.org/10.1038/s41467-

018-07255-1.

[8] M.A. Green, A. Ho-baillie, Perovskite Solar Cells : The Birth of a New Era in Photovoltaics, (2017). https://doi.org/10.1021/acsenergylett.7b00137.

[9] N.R.E.L. (NREL), Best Research-Cell Efficiency Chart, (n.d.). https://www.nrel.gov/pv/cell-efficiency.html.

[10] J.Y. Kim, J.-W. Lee, H.S. Jung, H. Shin, N.-G. Park, High-Efficiency Perovskite Solar Cells, Chem. Rev. 120 (2020) 7867–7918. https://doi.org/10.1021/acs.chemrev.0c00107.

[11] J. Ávila, C. Momblona, P.P. Boix, M. Sessolo, H.J. Bolink, Vapor-Deposited Perovskites: The Route to High-Performance Solar Cell Production?, Joule. 1 (2017) 431–442. https://doi.org/10.1016/j.joule.2017.07.014.

[12] A. Kojima, K. Teshima, Y. Shirai, T. Miyasaka, Organometal halide perovskites as visible-light sensitizers for photovoltaic cells, J. Am. Chem. Soc. 131 (2009) 6050–6051. https://doi.org/10.1021/ja809598r.

[13] L.K. Ono, E.J. Juarez-Perez, Y. Qi, Progress on Perovskite Materials and Solar Cells with Mixed Cations and Halide Anions, ACS Appl. Mater. Interfaces. 9 (2017) 30197–30246. https://doi.org/10.1021/acsami.7b06001.

[14] H.-S. Kim, A. Hagfeldt, N.-G. Park, Morphological and compositional progress in halide perovskite solar cells, Chem. Commun. 55 (2019) 1192–1200. https://doi.org/10.1039/C8CC08653B.

[15] T.M. Koh, K. Fu, Y. Fang, S. Chen, T.C. Sum, N. Mathews, S.G. Mhaisalkar, P.P. Boix, T. Baikie, Formamidinium-Containing Metal-Halide: An Alternative Material for Near-IR Absorption Perovskite Solar Cells, J. Phys. Chem. C. 118 (2014) 16458–16462. https://doi.org/10.1021/jp411112k.

[16] G.E. Eperon, S.D. Stranks, C. Menelaou, M.B. Johnston, L.M. Herz, H.J. Snaith, Formamidinium lead trihalide: a broadly tunable perovskite for efficient planar heterojunction solar cells, Energy Environ. Sci. 7 (2014) 982. https://doi.org/10.1039/c3ee43822h.

[17] T. Jesper Jacobsson, J.-P. Correa-Baena, M. Pazoki, M. Saliba, K. Schenk, M. Grätzel, A. Hagfeldt, Exploration of the compositional space for mixed lead halogen perovskites for high efficiency solar cells, Energy Environ. Sci. 9 (2016) 1706–1724. https://doi.org/10.1039/C6EE00030D.

[18] Z. Xu, Z. Liu, N. Li, G. Tang, G. Zheng, C. Zhu, Y. Chen, L. Wang, Y. Huang, L. Li, N. Zhou, J. Hong, Q. Chen, H. Zhou, A Thermodynamically Favored Crystal Orientation in Mixed Formamidinium/Methylammonium Perovskite for Efficient Solar Cells, Adv. Mater. (2019) 1900390. https://doi.org/10.1002/adma.201900390.

[19] R.G. Balakrishna, S.M. Kobosko, P. V. Kamat, Mixed Halide Perovskite Solar Cells. Consequence of Iodide Treatment on Phase Segregation Recovery, ACS Energy Lett. 3 (2018) 2267–2272. https://doi.org/10.1021/acsenergylett.8b01450.

[20] E.H. Jung, N.J. Jeon, E.Y. Park, C.S. Moon, T.J. Shin, T.-Y. Yang, J.H. Noh, J. Seo, Efficient, stable and scalable perovskite solar cells using poly(3-hexylthiophene), Nature. 567 (2019) 511–515. https://doi.org/10.1038/s41586-019-1036-3.

[21] H. Wang, C. Zhu, L. Liu, S. Ma, P. Liu, J. Wu, C. Shi, Q. Du, Y. Hao, S. Xiang, H. Chen, P. Chen, Y. Bai, H. Zhou, Y. Li, Q. Chen, Interfacial Residual Stress Relaxation in Perovskite Solar Cells with Improved Stability, Adv. Mater. 31 (2019) 1904408. https://doi.org/10.1002/adma.201904408.

[22] S.K. Yadavalli, Z. Dai, H. Zhou, Y. Zhou, N.P. Padture, Facile healing of cracks in organic–inorganic halide perovskite thin films, Acta Mater. 187 (2020) 112–121. https://doi.org/10.1016/j.actamat.2020.01.040.

[23] Z. Dai, S.K. Yadavalli, M. Chen, A. Abbaspourtamijani, Y. Qi, N.P. Padture, Interfacial toughening with self-assembled monolayers enhances perovskite solar cell reliability, Science (80-. ). 372 (2021) 618–622. https://doi.org/10.1126/science.abf5602.

[24] Z. Hawash, L.K. Ono, S.R. Raga, M. V. Lee, Y. Qi, Air-Exposure Induced Dopant Redistribution and Energy Level Shifts in Spin-Coated Spiro-MeOTAD Films, Chem. Mater. 27 (2015) 562–569. https://doi.org/10.1021/cm504022q.

[25] N. Rolston, B.L. Watson, C.D. Bailie, M.D. McGehee, J.P. Bastos, R. Gehlhaar, J.-E. Kim, D. Vak, A.T. Mallajosyula, G. Gupta, A.D. Mohite, R.H. Dauskardt, Mechanical integrity of solution-processed perovskite solar cells, Extrem. Mech. Lett. 9 (2016) 353–358. https://doi.org/10.1016/j.eml.2016.06.006.

[26] I. Lee, J.H. Yun, H.J. Son, T.-S. Kim, ":|?>L csx, ACS Appl. Mater. Interfaces. 9 (2017) 7029–7035. https://doi.org/10.1021/acsami.6b14089.

[27] J.H. Yun, I. Lee, T.-S. Kim, M.J. Ko, J.Y. Kim, H.J. Son, Synergistic enhancement and mechanism study of mechanical and moisture stability of perovskite solar cells introducing polyethylene-imine into the CH 3 NH 3 PbI 3 /HTM interface, J. Mater. Chem. A. 3 (2015) 22176–22182. https://doi.org/10.1039/C5TA06008G.

[28] O. V. Oyelade, O.K. Oyewole, D.O. Oyewole, S.A. Adeniji, R. Ichwani, D.M. Sanni, W.O. Soboyejo, Pressure-Assisted Fabrication of Perovskite Solar Cells, Sci. Rep. 10 (2020) 1–11. https://doi.org/10.1038/s41598-020-64090-5.

[29] D.O. Oyewole, R.K. Koech, R. Ichwani, R. Ahmed, J. Hinostroza Tamayo, S.A. Adeniji, J. Cromwell, E. Colin Ulloa, O.K. Oyewole, B. Agyei-Tuffour, L. V. Titova, N.A. Burnham, W.O. Soboyejo, Annealing effects on interdiffusion in layered FA-rich perovskite solar cells, AIP Adv. 11 (2021) 065327. https://doi.org/10.1063/5.0046205.

[30] A.. Evans, J.. Hutchinson, Effects of non-planarity on the mixed mode fracture resistance of bimaterial interfaces, Acta Metall. 37 (1989) 909–916. https://doi.org/10.1016/0001-6160(89)90017-5.

[31] T.M. Tong, Ting Tan, N. Rahbar, W.O. Soboyejo, Mode Mixity Dependence of Interfacial Fracture Toughness in Organic Electronic Structures, IEEE Trans. Device Mater. Reliab. 14 (2014) 291–299. https://doi.org/10.1109/TDMR.2013.2256788.

[32] N. Rahbar, Y. Yang, W. Soboyejo, Mixed mode fracture of dental interfaces, Mater. Sci. Eng. A. 488 (2008) 381–388. https://doi.org/10.1016/j.msea.2007.11.038.

[33] Z. Suo, J.W. Hutchinson, Sandwich test specimens for measuring interface crack toughness, Mater. Sci. Eng. A. 107 (1989) 135–143. https://doi.org/10.1016/0921-

5093(89)90382-1.

[34] B. Budiansky, J.C. Amazigo, A.G. Evans, Small-scale crack bridging and the fracture toughness of particulate-reinforced ceramics, J. Mech. Phys. Solids. 36 (1988) 167–187. https://doi.org/10.1016/S0022-5096(98)90003-5.

[35] J. Burschka, N. Pellet, S.-J. Moon, R. Humphry-Baker, P. Gao, M.K. Nazeeruddin, M. Grätzel, Sequential deposition as a route to high-performance perovskite-sensitized solar cells, Nature. 499 (2013) 316–319. https://doi.org/10.1038/nature12340.

[36] I. Lee, J.H. Yun, H.J. Son, T.-S. Kim, Accelerated Degradation Due to Weakened Adhesion from Li-TFSI Additives in Perovskite Solar Cells, ACS Appl. Mater. Interfaces. 9 (2017) 7029–7035. https://doi.org/10.1021/acsami.6b14089.

[37] Q. Yao, J. Qu, Interfacial Versus Cohesive Failure on Polymer-Metal Interfaces in Electronic Packaging—Effects of Interface Roughness, J. Electron. Packag. 124 (2002) 127–134. https://doi.org/10.1115/1.1459470.

# Chapter 5

# Optimization and Mechanical Integrity of Spray-Assisted Perovskite Solar Cells

### 5.1 Introduction

Hybrid perovskite solar cells (PSCs) have emerged as a promising photovoltaic (PV) light-harvester candidate for more a decade [1]. These materials exhibit excellent characteristics that are suitable for efficient light-absorbers, including long carrier diffusion length, high defect tolerance, tunable bandgap, and strong optical absorption [2,3]. Perovskite films are also desirable due to its earth-abundancy of raw materials, compatibility with flexible substrates and its ability to be formed in low-temperature processing [4]. The solution processing of perovskites enables solar cells to be fabricated quickly which helps to reduce manufacturing cost compared to the traditional silicon PV counterparts.

Perovskite solar cells are yet to become commercially available in the market. One obstacles of this technology is upscaling PSC to commercial PV module size (more > $1m^2$)[5]. Spin-coating is widely used technique for lab-scale perovskite fabrication which involves the precursor solution spreading on a substrate by centrifugal force. While this method is capable of producing highly uniform perovskites with up to 25% of photoconversion efficiency (PCE) of PSC, the vast reported research and development of PSC by spin-coating still remained the devices with small area (<$1cm^2$)[6]. Spin-coating also experienced large loss of precursor solution that wasted during deposition [7]. As a result, photovoltaic community urgently seek an alternative scalable deposition technique with a general aim to scale up

perovskite materials with comparable efficiency as those prepared via spin-coating technique for allowing PSC commercial manufacturing.

Research efforts on scalable solution-based technique of perovskites such as blade-coating [8], slot-die coating [9], inkjet printing [10], dip coating, and spray coating [11], has been explored. Among of those techniques, spray coating has better compatibility to coat nonplanar surfaces and it has been widely used in many industries such as painting of automotive parts [12], pigments and catalysts production, and battery materials [13]. The spray coating involves processes such as atomized microdroplets transportation onto substrate carried by compressed gas and substrate heating which helps to control the nucleation rate of perovskite crystals [7]. Although spray-coating is potentially deposited materials in big scale, high speed and minimal precursor ink loss, the physics behind this technique are multiscale and complex which various variables affect the properties of resulted materials [13,14].

Two-step sequential processes comprising the deposition of $PbI_2$ and organic precursor solution have been widely used to produce compact and void-less structures of perovskites. Various two step processes such as two-step spin coating [15], two-step thermal evaporation [16], spin coating of $PbI_2$ followed by dip coating of organic precursors [17], and spin coating of $PbI_2$ followed by thermal evaporation of organic precursors [18] has been reported as effort to produce pinhole free structures of perovskite film. However, problem of $PbI_2$ peeling and dissolving are remained once the organic precursor being deposited on top of $PbI_2$ film. Therefore, sequential technique combining spin and spray coating has been introduced for pinhole free film formation [19].

In the present work, perovskite absorber layers were fabricated via sequential two-steps of spin and spray-assisted coating combination in open air. As PSC performances are inextricably linked to properties of the formed perovskites absorber films, including their morphology, coverage and conformity to the underlying substrate [20], the spray parameters (substrate temperature, spray head height, and automated nozzle speed) was tuned to

fabricate pinhole free of spray-assisted perovskite film. The optimized 500 nm-perovskite film was produced with an excellent crystallinity. Higher mechanical reliability at interfaces of perovskite/adjacent CTLS and lower charge transfer resistances compared to the PSC via spin coating, spray-assisted PSCs achieves the best PCE of 9.98%. The fracture toughness of Perovskite/CTLs interfaces is also subjected to different loading positions and its associated toughening mechanism are investigated. We relate the interfacial contact of spray-assisted PSC to the application of pressure to further close the remained voids in the structures. This work illustrates that spray-assisted method of PSC is promising to push the scalability of efficient and reliable perovskite solar cells.

## 5.2 Experimental Sections

### 5.2.1 Device Fabrication

Mesoscopic architectures of hybrid organic–inorganic perovskite solar cells with structures of FTO/$TiO_2$/Perovskite/SpiroOMeTAD/Au were used in this study (Figure 5-1 inset). Prepatterned FTO-coated glass (12.5 x 25 $mm^2$) were sequentially cleaned vis sonication in Decon-90, deionized water, acetone, and IPA and treated under UV Ozone for 20 minutes. To prepare electron transporting layer, 0.15 and 0.3 M solution of titanium diisopropoxide bis(acetylacetone) (Sigma) was diluted in n-butanol. The 0.15 M solution spun at 2000 rpm for 30 s and heated at 125 °C for 5 min. It is followed by spin coating of 0.3 M solution at the same speed and annealing at 500 °C for 30 min [21,22]. Mesoporous $TiO_2$ was prepared from titania paste diluted at 1:5 in ethanol and spin coated at 4000 rpm for 30 s onto compact $TiO_2$ and sintered at 500 °C for 30 min.

Two-step sequential deposition technique was used to fabricate the perovskite layer. For each 1 ml of precursor solution, a mixture of 599.3 mg $PbI_2$ (> 98.9% purity, Sigma) dissolved in a mixture of DMF and DMSO at a ratio 9.5:0.5. First, the $PbI_2$ solution was spin-coated onto the ETL at 1500 rpm for 30 s and then dried at 70 °C for 1 min. Second, formamidium-rich organic precursor with following quantities: 60 mg FAI, 6 mg of MABr

and 6 mg of MACl (Sigma) were used for each 1 ml of IPA and sonicated for 1 hour. The precursor was spray casted using automated spray coating (MTI Corporation, Richmond, CA) illustrated in Figure 5-1. The atomizer nozzle was 40 kHz. The precursor solution was initially fed to the ink chamber and the spray system was programmed to move across the substrate in single pass at a speed of 100-300 mm/s, head-substrate height of 50-80 mm, and flow rate of 1 μm/min via compressed air. The spray pattern and spray velocity of solution at the nozzle was controlled by the compressed air where the pressure of 10 psi was maintained. The FTO/$TIO_2$/$PbI_2$ substrate was put on hot plate and heated at desired temperature for 1 min before spraying the organic precursor onto $PbI_2$ film in air. The spray coating was done in a single pass for 8 samples at once. The substrate temperature ($T_{sub}$) was also varied from 50-90°C. As-sprayed films were left for 30s for even solution distribution and heated at 130 °C for 30 min to promote complete conversion from $PbI_2$ to FA-rich perovskite crystal. The yellow layer of $PbI_2$ will be completely changed to black film of perovskite in this step.

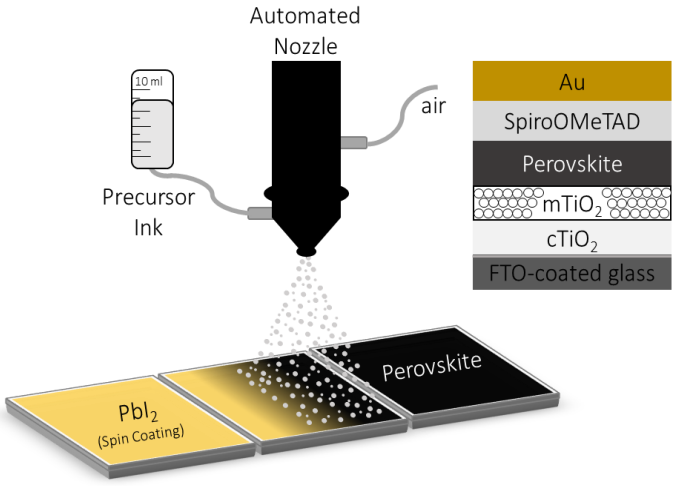


Figure 5-1 The schematic of spray coating method on perovskite film and the structure of complete devices stack used in the study (inset).

Hole transport layer (HTL), SpiroOMeTAD, was prepared by dissolving 72 mg of SpiroOMeTAD, 30 μL of 4-*tert*-butylpyridine (tBP) and 35 μL of lithium *bis*(trifluoromethylsulphony) imide (Li-TFSI) (260 mg of Li-TFSI in 1 ml of acetonitrile) dopants in 1 ml of chlorobenzene. Finally, 80 nm thick gold back contact electrode was thermally evaporated using a thermal evaporator (Edwards E306 A, Easton, PA) under a vacuum pressure of $10^{-6}$ Torr at a deposition rate of 0.1 nm $s^{-1}$.

### 5.2.2 Pressure Application

Full stack perovskite solar cells were subjected to external pressure ranging from 0-10 MPa. This was done using 5848 Instron MicroTester (Instron, Norwood, MA, USA) with cured PDMS anvil layer placed between device and the fixture. PDMS was made using a mixture ratio (10:1) by weight of Sylgard 184 silicon elastomer base and curing agent (Dow Corning Corporation, Midland, MI). The mixture was cured at 65 °C for 2h in a mold. The PDMS anvil was cut into desired dimension based on the size of solar cells. The Instron was set to compress the perovskite solar cells at a displacement rate of -1.0 mm $min^{-1}$ and hold for 10 minutes [23].

### 5.2.3 Interfacial Properties

*Adhesion*

To mimic the interfacial condition of perovskite solar cells, adhesion between perovskite and charge transporting layers (CTLs) were measured by interacting bi-materials at the interest interfaces using an atomic force microscopy (Park systems NX20, Santa Clara, CA) in ambient environment as described earlier [24,25]. The perovskite was coated on a substrate using the same procedure as mentioned in section 5.2.1 Device Fabrication, while the tips were coated by dip coating method. The contact tips (PPP-CONTSCR 10 M Par Systems) were used in this study and the cantilever spring constant of coated tips were measured before conducting each experiment.

*Interfacial Fracture Toughness*

Fracture toughness at interfaces between perovskites and CTLs were carried out using circular Brazil Disk specimen (Machined Ceramics, Bowling Green, KY). The configuration of the disk was explained in Reference [21]. The Brazil disk specimen geometries were chosen to enable the measurement of wide range of mode mixities between fracture mode I and II. It also allowed us to mimic the actual film in perovskite solar cells. The interest layers were deposited on the first half of the disk using method described in section 5.2.1 Device Fabrication. Epoxy (Epoxy Technology, Inc. Billerica, MA) was used to glue the first half disk to the second half disk to complete the Brazil disk. As shown in Figure 4-3 (a), complete Brazil disks were compressed using Instron testing machine (Instron 8872, Instron, Norwood, MA) to measure load-displacement curves that associated to interfacial facture behavior. A load cell of 1 kN at rates of 0.001 mm/s were used in the testing setup. The details of the fracture energy calculation are presented in section 4.3 Theory (Equations 4.1-4.8).

### 5.2.4 Characterization

Surface topographies were acquired with atomic force microscopy (Park systems NX 20, Santa Clara, CA) operating in tapping mode using AFM tip (PPP-NCHR, Park systems, Santa Clara, CA) with radius of less than 10 nm. The scanning areas were 5x5 $\mu m^2$, with resolution of 256 x 256 pixels performed in ambient environment with relative humidity of ~30-40%. Top Scanning Electron Microscope (SEM) were also done for each prepared perovskite film and cross-sectional view was for complete PSC devices. To estimate photovoltaic performance, perovskite solar cells were measured using a solar simulator (Oriel, Newport Corporation, Irvine, CA) with a source meter (Keithley, Tektronix, Newark, NJ) of 90 mW $cm^{-2}$ under illumination at AM 1.5G that were calibrated using 918D high performance calibrated photodiode sensor (Newport Corporation, Irvine, CA). The current density-voltage (*J–V*) curves were obtained by scanning in the range of -0.4 to 1.2V, with device exposed area of 0.1 $cm^2$. The electrochemical impedance spectroscopy (EIS) characteristics of

PSC devices were studied using a potentiostat (SP-300, BioLogic Instrument) performed in the frequency range 1 MHz-100 mHz. For toughening mechanism characterization, the top and cross-sectional of underlying fractured Brazil disks were observed under SEM/EDS system to elucidate the fracture path between the interest interfaces.

## 5.3 Results and Discussion

### 5.3.1 Device Fabrication

Sequential two-step processes (Figure 5-1) were used to deposit formamidium-rich (FA-rich) perovskite PSC devices. In perovskite film formation, the $PbI_2$ precursor was spin coated onto the FTO/$TiO_2$, followed by the spray-coating of FA-rich organic agents. The underlying $PbI_2$ thin film reacted with sprayed FA-rich organic precursor to form perovskite films. The spray system allows independent control of dispensing rate of solution, speed of spray head movement, substrate temperature, spray movement through the software interfaces, except the distance of substrate and spray head that was adjusted manually. Experimental optimizations were done to determine optimum substrate temperature, spray head-substrate distance, and drive speed of spray movement for fabricating pinhole free semitransparent perovskite films.

Substrate temperature ($T_{sub}$) is a key parameter to optimize a spray deposition technique [12]. In this study, the duration of heating the substrate was fixed at 1 min for every $T_{sub}$ to allow even heating on $PbI_2$ substrates before the formamidium-rich organic precursor being sprayed. There were interdiffusion of FA-rich organic droplets into $PbI_2$ identified from the gradual color changes upon contact between $PbI_2$ and FA-rich precursor, from yellow to black thin films [19,26]. The post annealing temperature and time were also fixed at 130°C for 30 min for all formed perovskite films. In Figure 5-2 (a-f), we present a series of SEM top and cross-sectional SEM images that show the effect of the $T_{sub}$ during deposition on quality of formed spray-assisted perovskite films. Voids in perovskites were not identified from the top view of SEM images (Figure 5-2 (a-c)). The perovskites had dense

and compact grain structures, while the grains show irregulars shape as $T_{sub}$ increasing. However, increasing the $T_{sub}$ resulted the formation of defects in perovskite structures and at interfaces to the neighboring transport layer (Figure 5-2 (d-f)). Non-compact and non-continuous films were reported when the applied $T_{sub}$ during processing were too high, resulting a rapid solvent evaporation even before the precursor ink being evenly spread and merge on substrates [27]. Therefore, $T_{sub}$ of 50°C was fixed to further optimization.

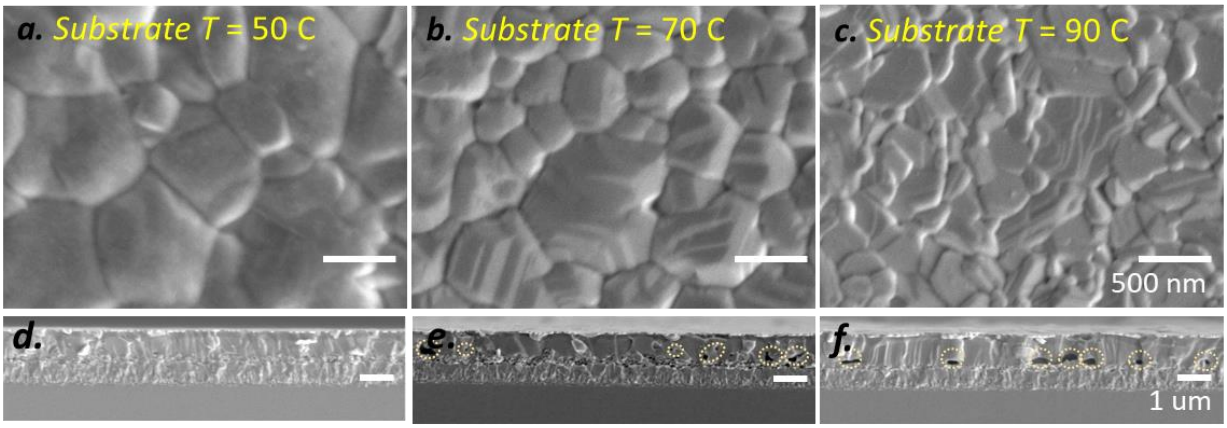


Figure 5-2 Top-view SEM images of deposited perovskite film and cross-sectional view images of complete PSC devices via spray-assisted technique at range of substrate temperatures, $T_{sub}$: 50°C (a and d), 70°C (b and e), and 90°C (c and f).

Next, keeping $T_{sub}$ fixed at 50°C and increasing velocity of the head as it passes across the substrate surfaces formed perovskite films with different grain sizes (Figure 5-3 (b-f)). Even though throughput speed in perovskite deposition process potentially reduced future manufacturing cost [28], increasing speed of spray movement caused the growth of smaller grain sizes. It shows that fabrication with moving speed of 150 mm/s (Figure 5-3 (c)) resulted in similar grains shape and size compared to the spray-coated film (Figure 5-3 (a)). Very small grain of perovskite films with more grain boundaries were not favorable as they may

induce charge recombination with their high defect density [29]. Finally, we also found that controlling head height played important role to maintain pinhole free films. Increasing head height did not give significant changes in perovskite grains (Figure 5-4). However, voids in film structures were identified in cross-sectional SEM images (Figure 5-5) as the head was closer to the surfaces. As the spray head moved closer to the surfaces and the spray velocity of solution at the nozzle was high, the sprayed droplets may bounce off from the target substates. Thus, $T_{sub}$ of 50°C, speed of 150 mm/s, and height of 7 mm were kept as the optimum conditions of spray-assisted PSC.

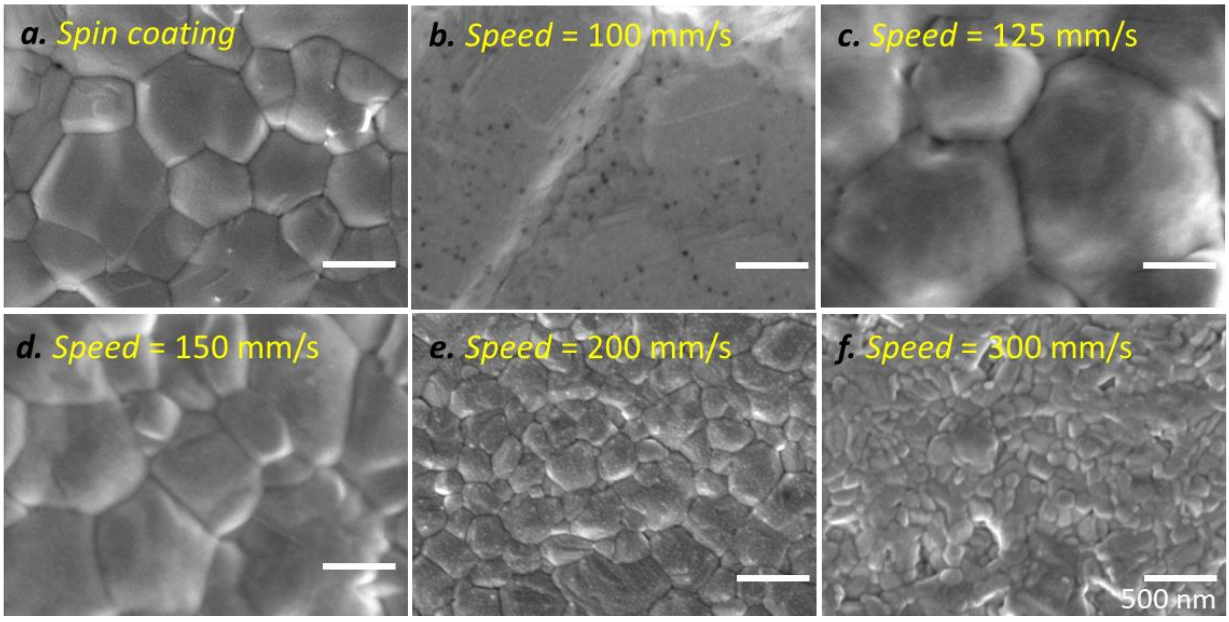


Figure 5-3 Top-view SEM images of deposited perovskite film via spin coating (a) and via spray-assisted technique at range of moving spray speed: (b) 100, (c) 125, (d) 150, (e) 200, and (f) 300 mm/s.

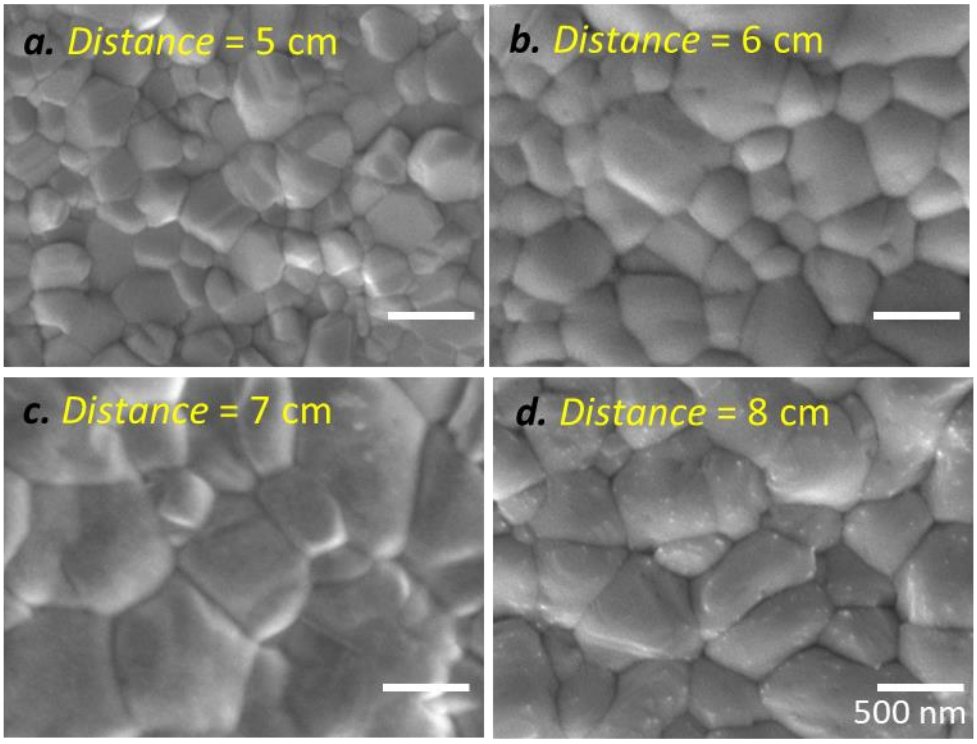


Figure 5-4 Top-view SEM images of spray-assisted perovskite film at range of spray head-substrate distance: (a) 5, (b) 6, (c) 7, and (d) 8 cm.

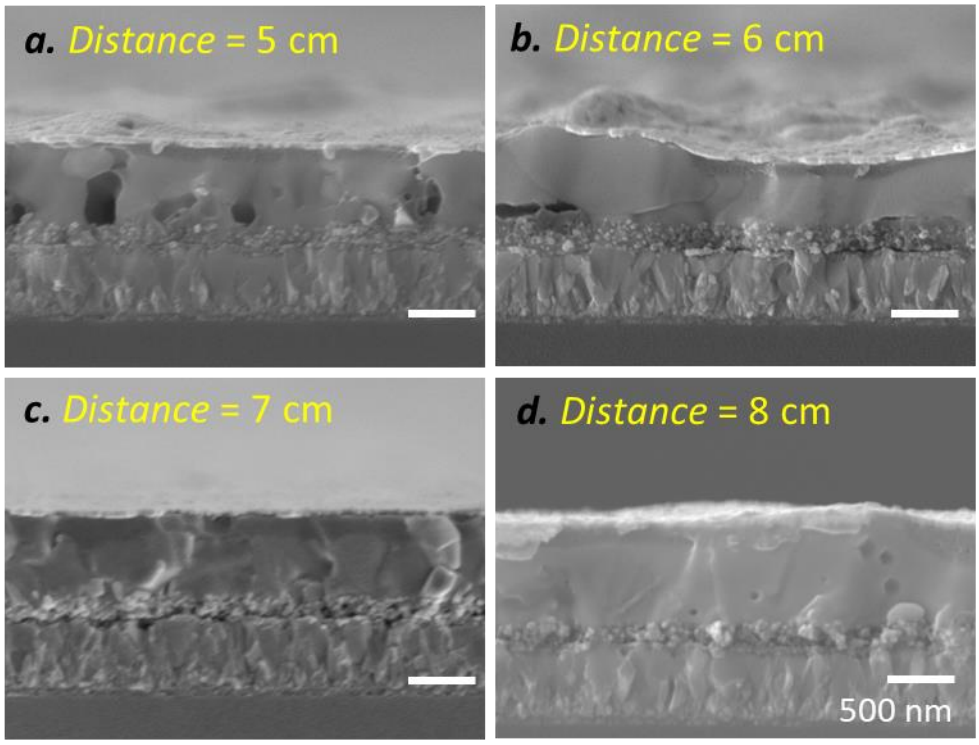


Figure 5-5 Cross-sectional view of SEM images of spray-assisted perovskite film at range of spray head-substrate distance: (a) 5, (b) 6, (c) 7, and (d) 8 cm.

### 5.3.2 Performances of the optimized Spray-Assisted PSCs

Through optimization of spray parameters, the morphology of optimum spray-assisted perovskite film had smoother surfaces confirmed by AFM characterization (Figure 5-6 (a-b)) with 40.46 ± 6.73 nm, compared to the spin coated film of 62.08 ± 8.38 nm. The final thickness of perovskites fabricated by both routes was equal of approximately 500-nm as illustrated in the SEM images of associated devices (Figure 5-6 (c-d)), substantiating the merit of spray coating.

A series of photovoltaic PSCs were fabricated based on the preceding optimization experiments and their performances were evaluated (Figure 5-7). In Figure 5-7 (a), comparable crystallinities were identified using X-Ray diffraction (XRD) as the diffraction intensity of sprayed and spin-coated perovskites had identical peaks. FA-rich perovskites

showed characteristic peak at 14.08°, while small peak of $PbI_2$ at 12.7° were remaining. Organic precursors were reported to hardly penetrate into $PbI_2$ seed layers, resulting some of $PbI_2$ was not completely reacted in solution processed PSCs [30]. Figure 5-7 (b) compares the absorption spectra of perovskites films by spray-assisted coating and spin coating. The absorbance of the spin coated perovskite is observed to be slightly higher than that of spray-assisted method. This is likely originated from the nature of greater roughness of the spin-coated perovskite films [31], compared to spray-assisted perovskite film as presented by AFM images in Figure 5-6 (a-b).

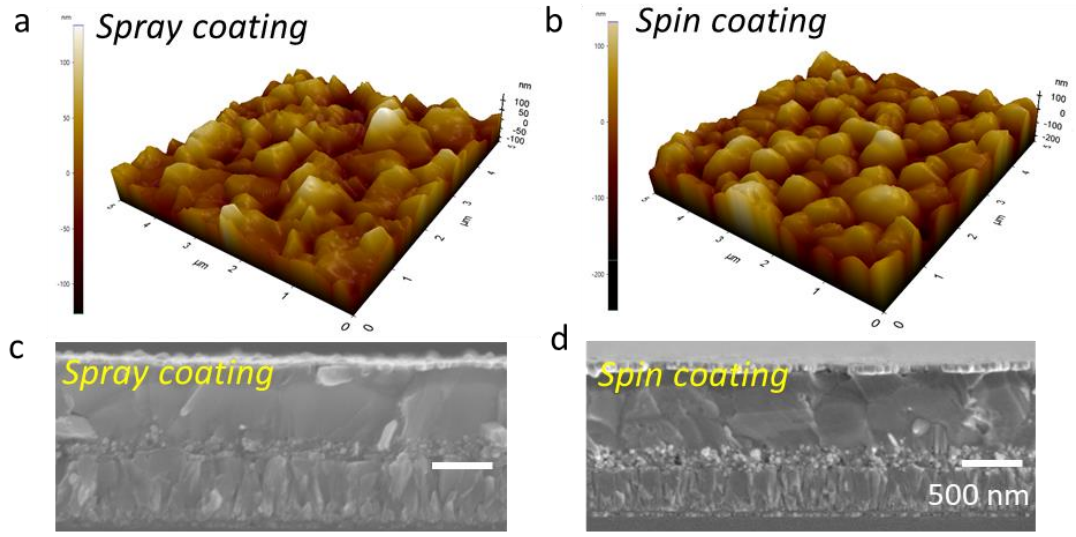


Figure 5-6 AFM images of perovskites films via spray-assisted coating (a) and spin-coating (b). Cross sectional images of SEM for spray-assisted PSC (c), and spin-coated PSC (d).

The *J-V* characteristics of optimum spray-assisted versus spray-coated PSCs are compared in Figure 5-7 (c). The champion device of spray-assisted PSC demonstrates the photoconversion efficiency of 8.58% at AM 1.5G one sun illumination, which was about half of the reference of spin-coated PSC of 16.49%. The difference in resulted performances were highly associated to the different mechanism of perovskite film formation as it were

fabricated with different processing. Even though the $PbI_2$ seed layer were identical for both devices, the deposition technique of FA-rich organic onto the $PbI_2$ were different. Spin-coated perovskites were crystallized through spreading precursor solution on the substrate by centrifugal forces, while spray coating relied on the transfer of the atomized microdroplets onto substrate [7]. Higher roughness of spin-coated perovskite films could also explain the higher $J_{sc}$ in the associated PSCs[31].

The external quantum efficiency (EQE) spectra for both spray-assisted and spin-coated PSCs is presented in Figure 5-7 (d). The EQE of spray-assisted PSC reached over 71% at the wavelength as short as 400 nm, maximized its value at 80% at 510 nm. However, the IPCE decreased to 73% at long wavelength region (73% up to 720 nm), indicating that the carrier diffusion length need to be further optimized [32]. The maximum $J_{sc}$ obtained from the champion device via spray coating was 16.85 $mA/cm^2$, that was relatively behind than the calculated integration $J_{sc}$ of 19.90 $mA/cm^2$ from IPCE data. Though the resulted performances of spray-assisted PSCs were still below the spin-coating PSC performances, spray-assisted PSCs is still worth to be further optimized as an effort to produce scalable devices in fast manner, which can be addressed in future work.

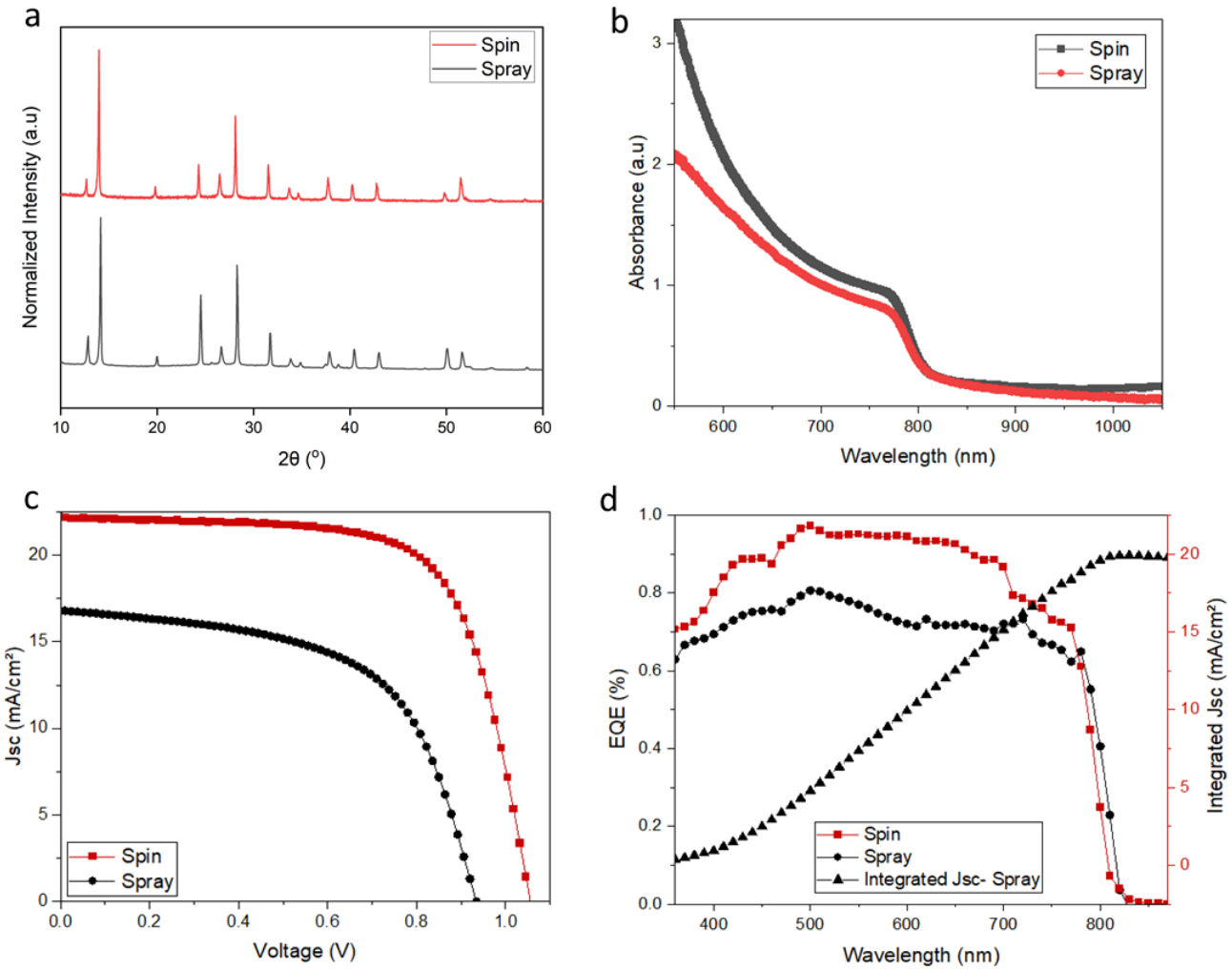


Figure 5-7 X-Ray diffraction pattern (a) and absorption Spectra (b) for spin-coated and spray-assisted perovskite films. The current density-voltage *J-V* curves (c) and the EQE spectra (d) for both associated PSCs. The integrated current density of spray-assisted PSC is also plotted in (d).

### 5.3.3 Mechanical Reliability of Spray-Assisted PSCs

For long operational lifetime, mechanical reliability towards delamination failure of PSC via spray-assisted fabrication is essential to be evaluated. Interfaces of perovskites and the adjacent charge transport layers (CTLs) are very critical PSC structures which facilitates

hole/electron extraction and hole/electron transfer [33]. Thus, this study combined nano-scale AFM experimental measurements of adhesion at interfaces between perovskite film to the adjacent CTLs ($TiO_2$ and SpiroOMeTAD). Figure 5-8 (a) shows the schematic of displacement curve of AFM measurements that consisting of some steps. The process is started with the initial approach of AFM cantilever to a coated substrate (step A). As the coated tip begins to move closer towards the substrate, it will jump to contact with the substrate (step B). The tip undergoes a deflection associated with the elastic bending (step C) before retraction (Step D). Due to the adhesive interactions, the tip does not detach from the coated substrate at zero force. The difference force is referred to adhesion forces [24,25].

For both routes, interfacial interactions between electron transport layer (ETL)/perovskite and perovskite/hole transport layer (HTL) were measured in Figure 5-8 (b). Interfaces of spray-assisted perovskites and both CTLs had a comparable adhesion interaction with that of spin-coated perovskites/both CTLs. The obtained adhesion was 445.63 ± 50.49 nN and 130.99 ± 34.48 nN for interfaces of spray-assisted perovskites /ETL and HTL, respectively. A small difference in adhesion at interfaces of perovskites/CTLs for both spray and spin coating technique were expected as both perovskite films had the identical chemistry characteristics confirmed by the associated XRD peaks (Figure 5-7 (a)). However, the roughness of perovskite films play role in the difference of interface interactions to the adjacent CTLs.

The nanoscale adhesion forces were further correlated with the charge carrier dynamics of perovskite solar cells. In Figure 5-8 (c), we performed electronic impedance spectroscopy (EIS) from 1 MHz-100 mHz and fitted the resulted curve to the appropriate equivalent circuit (Figure 5-8 (c), inset). Series resistance ($R_s$) represents resistance from FTO to metal electrode, charge transfer resistance ($R_{ct}$) represents resistance between perovskite and CTLs, and recombination resistance ($R_{rec}$) are included in the associated circuit [34]. The semicircle from high and low frequency regions were observed for both PSCs, in which the spray-assisted PSC had smaller diameter arc compared to spray-coated PSCs. The calculated

series resistance ($R_s$) of spray-assisted PSC was 20.85 Ω, slightly lower than that of spray-coated PSC of 28.72 Ω. The lower barrier of charge transport was also observed in spray-assisted PSC with $R_{ct}$ of 2.89 kΩ, compared to $R_{ct}$ of 8.76 kΩ for spin-coated PSC. The decrease in charge transfer resistances in spray-assisted PSCs is associated with the higher adhesion contact at interfaces of bulk sprayed perovskites/CTLs. The same phenomena was also reported earlier by Lee *et al*. that intimate contact in electronic structures lowered barrier to the charge injection in the devices [35]. Through lower performances of spray-assisted PSCs are observed, their adhesion and the charge transfer contact between layers were comparable as the high-efficiency spin-coated devices.

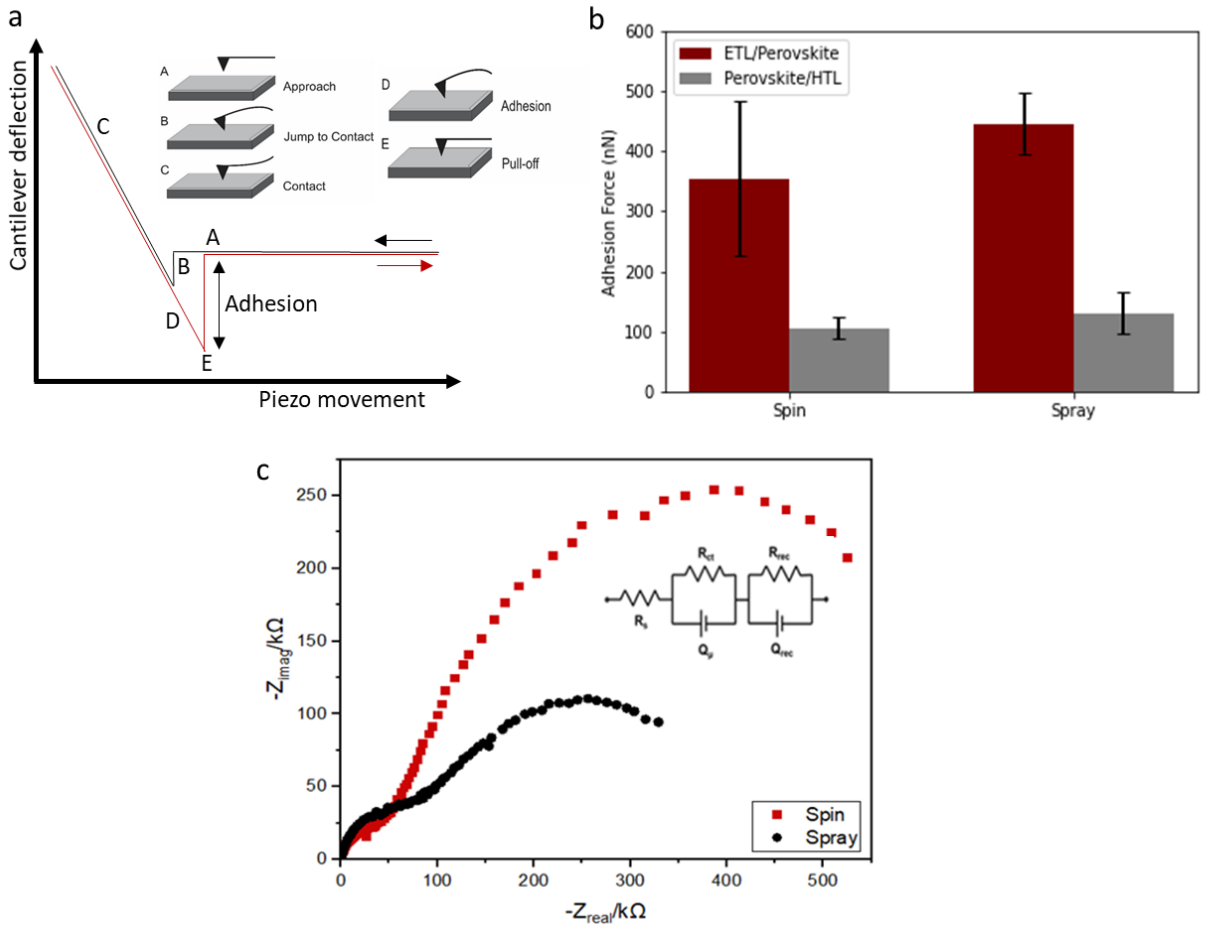


Figure 5-8 The schematic of displacement curve of AFM measurement (a). Comparison of measured adhesion forces between perovskites and CTLs for spray-assisted and spray coated techniques (b). Nyquist plot of impedance spectra at 0.1 V for both PSCs (c).

Fracture resistance of PSCs is crucial in preserving the electrical and mechanical reliability of device, preventing the perovskites decomposition [36]. To further investigate the robustness of interfaces in spray-assisted PSC, the interfacial fracture toughness in macroscale was carried out using Brazil disk fracture specimen presented in Figure 5-9 (a). It is semicircular specimens that is potentially oriented over ranges of mode mixities from pure mode I (opening) and mode II (in-plane shear)[21]. This study is relevant to the progress of flexible or stretchable PSC where integrity of PSC structures should be engineered over

range of loading condition [37]. As oriented in 3 different loading angles (0°, 7°, and 12°), the interfacial fracture energy increases with higher mode mixity (Figure 5-9 (b)). The interfacial fracture toughness was also further predicted by the zone shielding model to explore the on-going toughening mechanism. The predicted values were well agreeing with the measured values shown in Figure 5-9 (b).

Figure 5-9 (c) is the zone model schematic used to predict the fracture energy values using Equation 4.12 in section 4.3.2 Toughening Mechanisms. The toughening mechanism is attributed to the zone in which it considers the effects of presented microcracks and ligament bridges along the interfaces [21]. In order to explore the enhancement on fracture energy in spray-assisted PSC, the fractured Brazil disks were characterized cross sectionally by SEM after loading. As crack bridging can be simulated as a series of connected springs [38], the evidences of zone mechanism were obviously captured in Figure 5-9 (d-e) for perovskite/HTL interfaces. There were bridge ligaments connecting the crack faces along the interfaces of perovskite/HTL. Moreover, for the interfaces of ETL/perovskite, the similar bridging phenomena were also obviously seen at interfaces of perovskite/ETL, where perovskite kinked to the mesoporous $TiO_2$ ETL layer, contributing to enhance fracture energy in that interface.

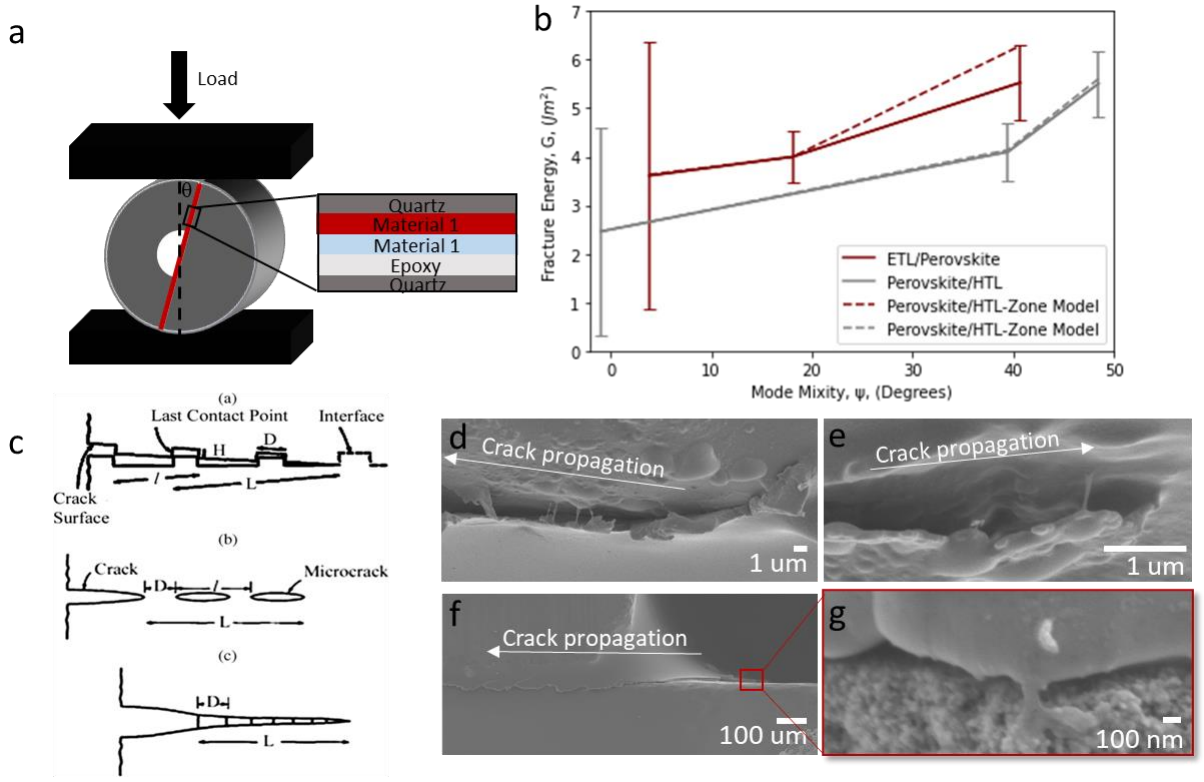


Figure 5-9 The schematic work using Brazil disk specimen (a). The measured and predicted average interfacial fracture toughness, *G*, as a function of mode mixity (b). Crack growth in zone model with spring idealization of crack bridging. Adapted from Ref.[39] (c). Representative of captured toughening mechanism between spray-assisted perovskites/HTL (d-e) and ETL/perovskites (f-g).

### 5.3.4 The effects of pressure application on Spray-Assisted PSC Performances

A notable increase on performances has been reported as the application of physical compressive pressure on electronic devices [23,35,40,41]. We performed an investigation on the effects of pressure on the spray-assisted PSC performances. Figure 5-10 (a) shows the schematic of compressive pressure on complete PSC devices. To protect the PSC device, we put an anvil (PDMS in this case) on device's surface before pressure being applied. Various pressure from 2-10 MPa was applied to the devices using Instron machine.

The detailed of PSC performances were shown in Table 5.1. We observed there was an increase on $J_{sc}$, $V_{oc}$, and the resultant photoconversion efficiency (PCE) of spray-assisted PSCs (Figure 5-10 (b)) by physical pressure application up to 7 MPa. The results shows that the optimum efficiency of PSC increased from 8.58% to 9.98% with 7 MPa pressure. This phenomenon was largely due to the contact evaluation between functional layers (Figure 5-10 (c-e)), in which the crack length was significantly reduced as reported earlier in spin-coated devices [23].

Table 5.1 Device performance parameters of spray-assisted PSC with different applied pressure

| Pressure | $V_{oc}$ (V) | $J_{sc}$ (mA/cm$^2$) | PCE (%) | FF |
|---|---|---|---|---|
| No Pressure | 0.89 ± 0.02 | 16.59 ± 0.26 | 8.58 (8.31± 0.19) | 0.53 ± 0.01 |
| 3 MPa | 0.91 ± 0.01 | 17.41 ± 0.91 | 8.83 (8.51± 0.37) | 0.53 ± 0.03 |
| 7 MPa | 0.93 ± 0.01 | 18.01 ± 0.45 | 9.98 (9.03 ± 0.74) | 0.56 ± 0.03 |
| 10 MPa | 0.92 ± 0.01 | 16.03 ± 2.47 | 8.10 (7.01 ± 1.53) | 0.48 ± 0.11 |

Figure 5-10 (c) shows the remained defects in the spray-assisted PSC structures upon fabrication. By applying external pressure of 7 MPa, evidence of an intimate contact between functional layers in PSCs was seen in cross-sectional images of PSC (Figure 5-10 (d)), where the remained voids were compacted. As described in Section 5.3.3, high adhesion/contact between layers in spray-assisted PSC structures was favorable for improving the performances of devices. The strong adhesion caused by the intimate contact could facilitate

an efficient charge transfer within the structures and reduce charge transfer resistances, leading to an improvement of spray-assisted device efficiency. However, crack was initiated at higher compressive pressure (10 MPa) as seen in Figure 5-10 (e). Physical applied pressure of 10 MPa opened up the initial interfacial cracks and created a failure in the bulk perovskite film (annotated by arrow in Figure 5-10 (e)). Thus, a decrease in PSC performances were demonstrated to 8.10% from the associated *J-V* characteristics.

### 5.3.5 Implications

The implications of the current results are significant for the scalability of reliable perovskite solar cells using spray coating techniques. First, this study provides an insight in which wide space of variables in spray coating system offers an opportunity to further optimize the spray conditions to achieve voids-free and highly efficient PSCs. Second, it also shows that the mechanical reliability of spray-assisted PSC is comparable to the high efficiency of spray-coated devices. It shows that replacement small-area coating via spin coating can be transformed to scalable spray deposition technique towards large-scale manufacturing of PSCs. Higher adhesion/contact between spray-assisted perovskites and the adjacent charge transporting layers (CTLs) leads to the lower barrier of charge transportation within the structures. Third, interfacial fracture toughness improves as the mode mixity increasing. It is relevant to the progress of flexible or stretchable PSC where integrity of PSC should be engineered for range of loading conditions. Crack bridging or interlocking phenomena between perovskite and the neighboring CTLs have a significant effect in the initiation fracture along the interfaces. Finally, this study gives an insight that the use of external physical pressure can also contribute to fabricate pinhole/defect free structures of spray-assisted perovskite, without focusing only on adjustment of internal variables of spray coating system itself.

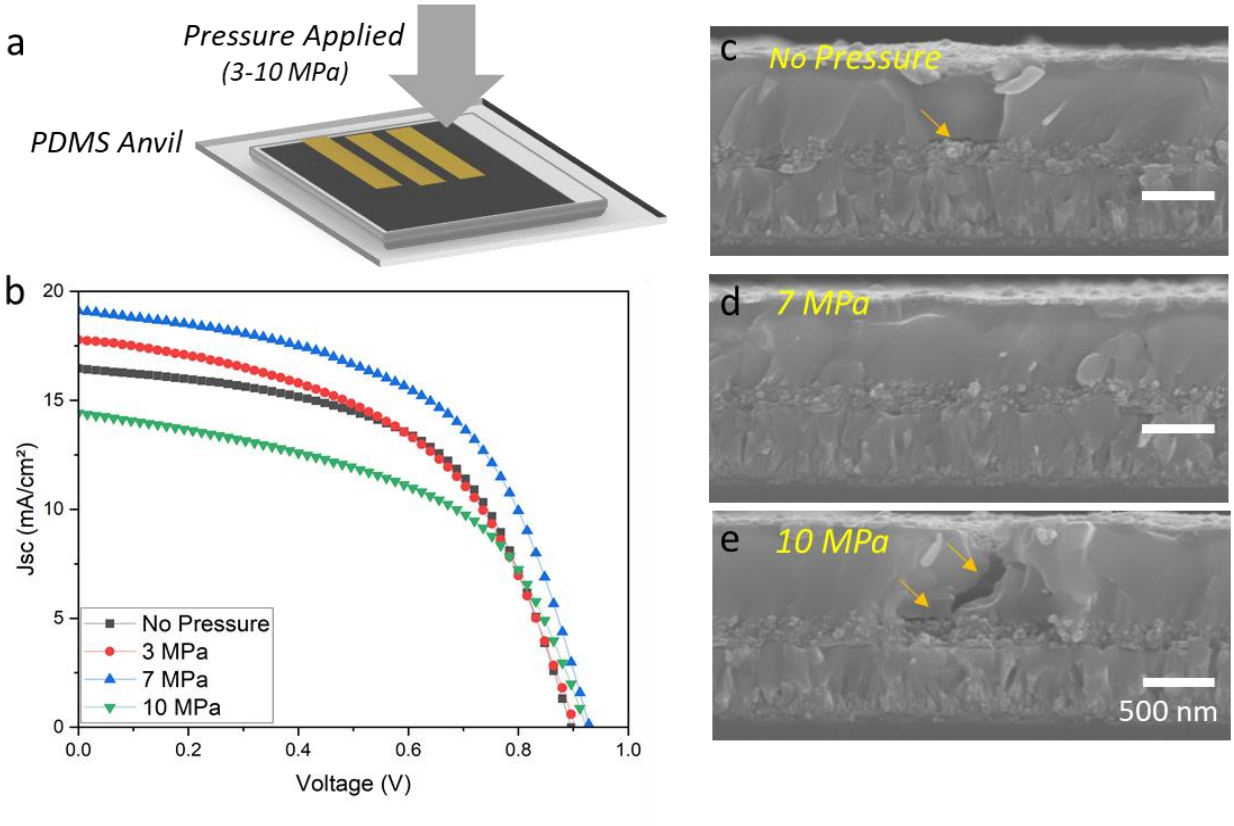


Figure 5-10 The schematic of compressive pressure-assisted fabrication of sprayed PSCs (a). The J-V characteristics of PSCs as applied pressure increasing (b). Cross-sectional SEM images of PSC with voids at the interfaces (c), void and crack closure with moderate applied pressure of 7 MPa (d), and cracking with 10 MPa applied pressure.

## 5.4 Conclusion

In summary, we have optimized the formation of perovskite films via spray-assisted method. The perovskite films are prepared by a sequential two-step combining of spin of $PbI_2$ and spray coating of FA-rich precursor in air. Compared to the spin-coated PSCs, the optimized spray-assisted perovskites exhibit an excellent crystallinity, and the resulted PSCs demonstrate a comparable efficiency of 8.58 (8.31± 0.19) %, low charge transfer barrier within the structures, and higher mechanical reliability at interfaces of bulk perovskite/neighboring

charge transporting layers (CTLs). The interfacial integrity of perovskite/CTLs interfaces was also subjected to different loading positions, showing an increment of fracture energy as the mode mixity increasing. The increment was attributed to the interfaces interlocking by the presented crack bridging ligaments along interfaces upon fracture test. Finally, interfacial contact between perovskites/CTLs provide an insight to pressure application of spray-assisted PSCs, contributing to the improved PSC performances to 9.98 (9.03 ± 0.74) % with pressure of 7 MPa. Through various characterizations, we recognize that the high-efficiency of spray-assisted PSCs can be further achieved by the optimization of spray conditions, which can be addressed in the future. Through this work, we highlight that this combination of techniques provides an efficient route for fabrication of low-temperature processing of scalable perovskite solar cells.

**References**


[1] Y. Rong, Y. Hu, A. Mei, H. Tan, M.I. Saidaminov, S. Il Seok, M.D. McGehee, E.H. Sargent, H. Han, Challenges for commercializing perovskite solar cells, Science (80-. ). 361 (2018). https://doi.org/10.1126/science.aat8235.

[2] G. Xing, N. Mathews, S. Sun, S.S. Lim, Y.M. Lam, M. Grätzel, S. Mhaisalkar, T.C. Sum, Long-Range Balanced Electron- and Hole-Transport Lengths in Organic-Inorganic CH 3 NH 3 PbI 3, Science (80-. ). 342 (2013) 344–347. https://doi.org/10.1126/science.1243167.

[3] C. Zuo, H.J. Bolink, H. Han, J. Huang, D. Cahen, L. Ding, Advances in Perovskite Solar Cells, Adv. Sci. 3 (2016) 1500324. https://doi.org/10.1002/advs.201500324.

[4] V.M. Goldschmidt, The principles of distribution of chemical elements in minerals and rocks. The seventh Hugo Müller Lecture, delivered before the Chemical Society on March 17th, 1937, J. Chem. Soc. 361 (1937) 655–673. https://doi.org/10.1039/JR9370000655.

[5] I.A. Howard, T. Abzieher, I.M. Hossain, H. Eggers, F. Schackmar, S. Ternes, B.S. Richards, U. Lemmer, U.W. Paetzold, Coated and Printed Perovskites for Photovoltaic Applications, Adv. Mater. 31 (2019) 1806702. https://doi.org/10.1002/adma.201806702.

[6] J.X.J. Zhang, K. Hoshino, Fundamentals of nano/microfabrication and scale effect, in: Mol. Sensors Nanodevices, Elsevier, 2019: pp. 43–111. https://doi.org/10.1016/B978-0-12-814862-4.00002-8.

[7] J. Su, H. Cai, J. Yang, X. Ye, R. Han, J. Ni, J. Li, J. Zhang, Perovskite Ink with an Ultrawide Processing Window for Efficient and Scalable Perovskite Solar Cells in Ambient Air, ACS Appl. Mater. Interfaces. 12 (2020) 3531–3538. https://doi.org/10.1021/acsami.9b17141.

[8] W.-Q. Wu, Q. Wang, Y. Fang, Y. Shao, S. Tang, Y. Deng, H. Lu, Y. Liu, T. Li, Z. Yang, A. Gruverman, J. Huang, Molecular doping enabled scalable blading of efficient hole-transport-layer-free perovskite solar cells, Nat. Commun. 9 (2018) 1625.

https://doi.org/10.1038/s41467-018-04028-8.

[9] J.B. Whitaker, D.H. Kim, B.W. Larson, F. Zhang, J.J. Berry, M.F.A.M. van Hest, K. Zhu, Scalable slot-die coating of high performance perovskite solar cells, Sustain. Energy Fuels. 2 (2018) 2442–2449. https://doi.org/10.1039/C8SE00368H.

[10] P. Li, C. Liang, B. Bao, Y. Li, X. Hu, Y. Wang, Y. Zhang, F. Li, G. Shao, Y. Song, Inkjet manipulated homogeneous large size perovskite grains for efficient and large-area perovskite solar cells, Nano Energy. 46 (2018) 203–211. https://doi.org/10.1016/j.nanoen.2018.01.049.

[11] J.E. Bishop, D.K. Mohamad, M. Wong-Stringer, A. Smith, D.G. Lidzey, Spray-cast multilayer perovskite solar cells with an active-area of 1.5 cm2, Sci. Rep. 7 (2017) 7962. https://doi.org/10.1038/s41598-017-08642-2.

[12] J.E. Bishop, T.J. Routledge, D.G. Lidzey, Advances in Spray-Cast Perovskite Solar Cells, J. Phys. Chem. Lett. 9 (2018) 1977–1984. https://doi.org/10.1021/acs.jpclett.8b00311.

[13] N.H. Paulson, J.A. Libera, M. Stan, Flame spray pyrolysis optimization via statistics and machine learning, Mater. Des. 196 (2020) 108972. https://doi.org/10.1016/j.matdes.2020.108972.

[14] J.E. Bishop, C.D. Read, J.A. Smith, T.J. Routledge, D.G. Lidzey, Fully Spray-Coated Triple-Cation Perovskite Solar Cells, Sci. Rep. 10 (2020) 6610. https://doi.org/10.1038/s41598-020-63674-5.

[15] H. Zhou, Q. Chen, G. Li, S. Luo, T. Song, H.-S. Duan, Z. Hong, J. You, Y. Liu, Y. Yang, Interface engineering of highly efficient perovskite solar cells, Science (80-. ). 345 (2014) 542–546. https://doi.org/10.1126/science.1254050.

[16] J. Burschka, N. Pellet, S.-J. Moon, R. Humphry-Baker, P. Gao, M.K. Nazeeruddin, M. Grätzel, Sequential deposition as a route to high-performance perovskite-sensitized solar cells, Nature. 499 (2013) 316–319. https://doi.org/10.1038/nature12340.

[17] D. Liu, T.L. Kelly, Perovskite solar cells with a planar heterojunction structure

prepared using room-temperature solution processing techniques, Nat. Photonics. 8 (2014) 133–138. https://doi.org/10.1038/nphoton.2013.342.

[18] Q. Chen, H. Zhou, Z. Hong, S. Luo, H.-S. Duan, H.-H. Wang, Y. Liu, G. Li, Y. Yang, Planar Heterojunction Perovskite Solar Cells via Vapor-Assisted Solution Process, J. Am. Chem. Soc. 136 (2014) 622–625. https://doi.org/10.1021/ja411509g.

[19] K.M. Boopathi, M. Ramesh, P. Perumal, Y.-C. Huang, C.-S. Tsao, Y.-F. Chen, C.-H. Lee, C.-W. Chu, Preparation of metal halide perovskite solar cells through a liquid droplet assisted method, J. Mater. Chem. A. 3 (2015) 9257–9263. https://doi.org/10.1039/C4TA06392A.

[20] N. Alhazmi, E. Pineda, J. Rawle, J.R. Howse, A.D.F. Dunbar, Perovskite Crystallization Dynamics during Spin-Casting: An In Situ Wide-Angle X-ray Scattering Study, ACS Appl. Energy Mater. 3 (2020) 6155–6164. https://doi.org/10.1021/acsaem.9b02470.

[21] R. Ichwani, R. Koech, O.K. Oyewole, A. Huda, D.O. Oyewole, J. Cromwell, J.L. Martin, R.L. Grimm, W.O. Soboyejo, Interfacial fracture of hybrid organic–inorganic perovskite solar cells, Extrem. Mech. Lett. 50 (2022) 101515. https://doi.org/10.1016/j.eml.2021.101515.

[22] O. V. Oyelade, O.K. Oyewole, Y.A. Olanrewaju, R. Ichwani, R. Koech, D.O. Oyewole, S.A. Adeniji, D.M. Sanni, J. Cromwell, R.A. Ahmed, K. Orisekeh, V.C. Anye, W.O. Soboyejo, Understanding the effects of annealing temperature on the mechanical properties of layers in FAI-rich perovskite solar cells, AIP Adv. 12 (2022) 025104. https://doi.org/10.1063/5.0078558.

[23] O. V. Oyelade, O.K. Oyewole, D.O. Oyewole, S.A. Adeniji, R. Ichwani, D.M. Sanni, W.O. Soboyejo, Pressure-Assisted Fabrication of Perovskite Solar Cells, Sci. Rep. 10 (2020) 1–11. https://doi.org/10.1038/s41598-020-64090-5.

[24] D. Yu, O.K. Oyewole, D. Kwabi, T. Tong, V.C. Anye, J. Asare, E. Rwenyagila, A. Fashina, O. Akogwu, J. Du, W.O. Soboyejo, Adhesion in flexible organic and hybrid organic/inorganic light emitting device and solar cells, J. Appl. Phys. 116 (2014) 074506.

https://doi.org/10.1063/1.4892393.

[25] T. Tong, B. Babatope, S. Admassie, J. Meng, O. Akwogu, W. Akande, W.O. Soboyejo, Adhesion in organic electronic structures, J. Appl. Phys. 106 (2009) 083708. https://doi.org/10.1063/1.3246786.

[26] Z. Xiao, C. Bi, Y. Shao, Q. Dong, Q. Wang, Y. Yuan, C. Wang, Y. Gao, J. Huang, Efficient, high yield perovskite photovoltaic devices grown by interdiffusion of solution-processed precursor stacking layers, Energy Environ. Sci. 7 (2014) 2619–2623. https://doi.org/10.1039/C4EE01138D.

[27] M. Liu, M.B. Johnston, H.J. Snaith, Efficient planar heterojunction perovskite solar cells by vapour deposition, Nature. 501 (2013) 395–398. https://doi.org/10.1038/nature12509.

[28] J.E. Bishop, J.A. Smith, D.G. Lidzey, Development of Spray-Coated Perovskite Solar Cells, ACS Appl. Mater. Interfaces. 12 (2020) 48237–48245. https://doi.org/10.1021/acsami.0c14540.

[29] X. Xu, Y. Sun, D. He, Z. Liang, G. Liu, S. Xu, Z. Li, L. Zhu, X. Pan, Grain size control for high-performance formamidinium-based perovskite solar cells via suppressing heterogenous nucleation, J. Mater. Chem. C. 9 (2021) 208–213. https://doi.org/10.1039/D0TC04833J.

[30] T. Du, N. Wang, H. Chen, H. Lin, H. He, Comparative Study of Vapor- and Solution-Crystallized Perovskite for Planar Heterojunction Solar Cells, ACS Appl. Mater. Interfaces. 7 (2015) 3382–3388. https://doi.org/10.1021/am508495r.

[31] S. Uličná, B. Dou, D.H. Kim, K. Zhu, J.M. Walls, J.W. Bowers, M.F.A.M. van Hest, Scalable Deposition of High-Efficiency Perovskite Solar Cells by Spray-Coating, ACS Appl. Energy Mater. 1 (2018) 1853–1857. https://doi.org/10.1021/acsaem.8b00328.

[32] H. Huang, J. Shi, L. Zhu, D. Li, Y. Luo, Q. Meng, Two-step ultrasonic spray deposition of CH3NH3PbI3 for efficient and large-area perovskite solar cell, Nano Energy. 27 (2016) 352–358. https://doi.org/10.1016/j.nanoen.2016.07.026.

[33] A.A. Said, J. Xie, Q. Zhang, Recent Progress in Organic Electron Transport Materials

in Inverted Perovskite Solar Cells, Small. 15 (2019) 1900854. https://doi.org/10.1002/smll.201900854.

[34] K. Hongsith, V. Yarangsi, S. Sucharitakul, S. Phadungdhitidhada, A. Ngamjarurojana, S. Choopun, A Multi-Electron Transporting Layer for Efficient Perovskite Solar Cells, Coatings. 11 (2021) 1020. https://doi.org/10.3390/coatings11091020.

[35] J.H. Kim, S. Seo, H.H. Lee, Nanovoid nature and compression effects in organic light emitting diode, Appl. Phys. Lett. 90 (2007) 143521. https://doi.org/10.1063/1.2720268.

[36] S. Jeong, I. Lee, T. Kim, J. Lee, An Interlocking Fibrillar Polymer Layer for Mechanical Stability of Perovskite Solar Cells, Adv. Mater. Interfaces. 7 (2020) 2001425. https://doi.org/10.1002/admi.202001425.

[37] T.M. Tong, Ting Tan, N. Rahbar, W.O. Soboyejo, Mode Mixity Dependence of Interfacial Fracture Toughness in Organic Electronic Structures, IEEE Trans. Device Mater. Reliab. 14 (2014) 291–299. https://doi.org/10.1109/TDMR.2013.2256788.

[38] M.M. Shokrieh, S.M. Ghoreishi, M. Esmkhani, Toughening mechanisms of nanoparticle-reinforced polymers, in: Toughening Mech. Compos. Mater., Elsevier, 2015: pp. 295–320. https://doi.org/10.1016/B978-1-78242-279-2.00011-1.

[39] A.. Evans, J.. Hutchinson, Effects of non-planarity on the mixed mode fracture resistance of bimaterial interfaces, Acta Metall. 37 (1989) 909–916. https://doi.org/10.1016/0001-6160(89)90017-5.

[40] R.A. Ahmed, N. Ebechidi, I. Reisya, K. Orisekeh, A. Huda, A. Bello, O.K. Oyewole, W.O. Soboyejo, Pressure-induced interfacial contacts and the deformation in all solid-state Li-ion batteries, J. Power Sources. 521 (2022) 230939. https://doi.org/10.1016/j.jpowsour.2021.230939.

[41] T.-W. Lee, J. Zaumseil, Z. Bao, J.W.P. Hsu, J.A. Rogers, Organic light-emitting diodes formed by soft contact lamination, Proc. Natl. Acad. Sci. 101 (2004) 429–433. https://doi.org/10.1073/pnas.0304179101.

# Chapter 6

# Machine Learning for Optimization of Spray Processed Perovskite Solar Cells

### 6.1 Introduction

Solution processability of hybrid perovskite absorbers at low temperature is an attractive feature of perovskite photovoltaic (PV) technology [1]. It enables solar cell devices to be fabricated quickly at lower costs unlike traditional silicon PV counterparts. In the current state, spin coating is the most widely used technique to develop perovskite solar cells in laboratory scale that spreads precursor solution on a substrate by centrifugal force [2]. While this method is capable of producing highly efficient devices up to 25% of photoconversion efficiency, the spin coating technique suffers from low nonuniformity in film thickness, poor process reproducibility, and poor suited to large-area coating. As a result, the photovoltaic community seeks alternative scalable deposition techniques with the general aim of producing devices with high efficiencies that are comparable to those of solar cells prepared via spin-coating technique [3,4].

Some alternatives of scalable solution techniques of perovskites production have been investigated, e.g., blade-coating [5], slot-die coating [6], inkjet printing [7], and spray coating [3]. Among those, spray coating has improved the capacity for the coating of nonplanar surfaces, and it is also used widely in many industries for the painting of automotive parts [3,8], pigments and catalysts production, and battery materials [9]. Although spray-coating can be used to deposit materials on a large scale, the physics behind this technique are multiscale and complex. Many variables impact the properties of resulting materials [9]. In

the case of PSCs, spray coating of perovskites relies on the precursor ink that is formulated at relatively low solution concentrations, resulting in the dewetting of the film during drying process and voids in the perovskite structures [4]. Thus, adjustable variables in spray-processing and post-treatments are required to be optimized in fabricating efficient perovskite layers. The variables include spray nozzle speed, substrate temperature, flow rates, nozzle head to substrate height, annealing time, and external applied pressure.

Optimization of the spray processing of perovskites has traditionally relied on a combination of domain knowledge as well as the *trial-and-error* approach. Approach of *One factor in a time* or optimizing a variable and the optimum variable held constant for another variable optimization has been often used in most prior studies in process optimization [10], including our own experiment. Exploring sets of possible parameters of process optimization, particularly spray deposition, is often challenging and time consuming to optimize, due to the high-dimensional of parameter spaces of processing and time needed to perform the experiments [11].

Significant attention, recently, has been given to machine learning (ML) approaches to identify the effects of key variables on the desired properties using a much-reduced dataset. The resulted combination of parameters and properties outcome can be generalized to the larger set of all combinations of variable ranges [12]. It turns out that ML approaches such as regression models could help to strategically guide the design of experiments (DOE) [10]. This DOE is based on the choice of the most efficient parameter spaces with minimal number of experiments to create an appropriate model. ML based strategies have been used in some deposition techniques to optimize processing parameters, such as direct ink printing [13] and flame spray pyrolysis [9]. Therefore, the searching process of the best configurations of PSC via spray coating is suitable for ML-guided approach with purpose of manufacturing perovskite solar cells with shorter timescale and cheaper in budget that was previously possible.

In this work, we develop ML-guided framework for the spray processing of perovskite solar cells with the improved power conversion efficiency (PCE) as the target variable. The general framework is divided into 4 steps illustrated in Figure 6-1.

1. The initial step consists of processing perovskite solar cells using spray coating.
2. The PCE of resulting PSCs are then measured under the solar simulator. The resulting current-voltage (*I-V*) curves are used to extract PV parameters such as PCE.
3. With the known spray PSC fabrication variables and PCEs, a regression model is trained to learn the *variables-device efficiency* correlation. The trained model is used to predict the optimal PCE relative to the experimentally measured PCE. The results subsequently suggest a dataset design for the *next round* that is balanced in experimental feasibility and broadness of parameter space to achieve optimal efficiency of perovskite solar cells.
4. The new design of experiments was selected to efficiently optimize the resulted perovskite absorbing layer via spray coating for the *next-round* experiments.

Finally, the implications of the results will be used to guide the experimental process of designing efficient spray-assisted PSCs.

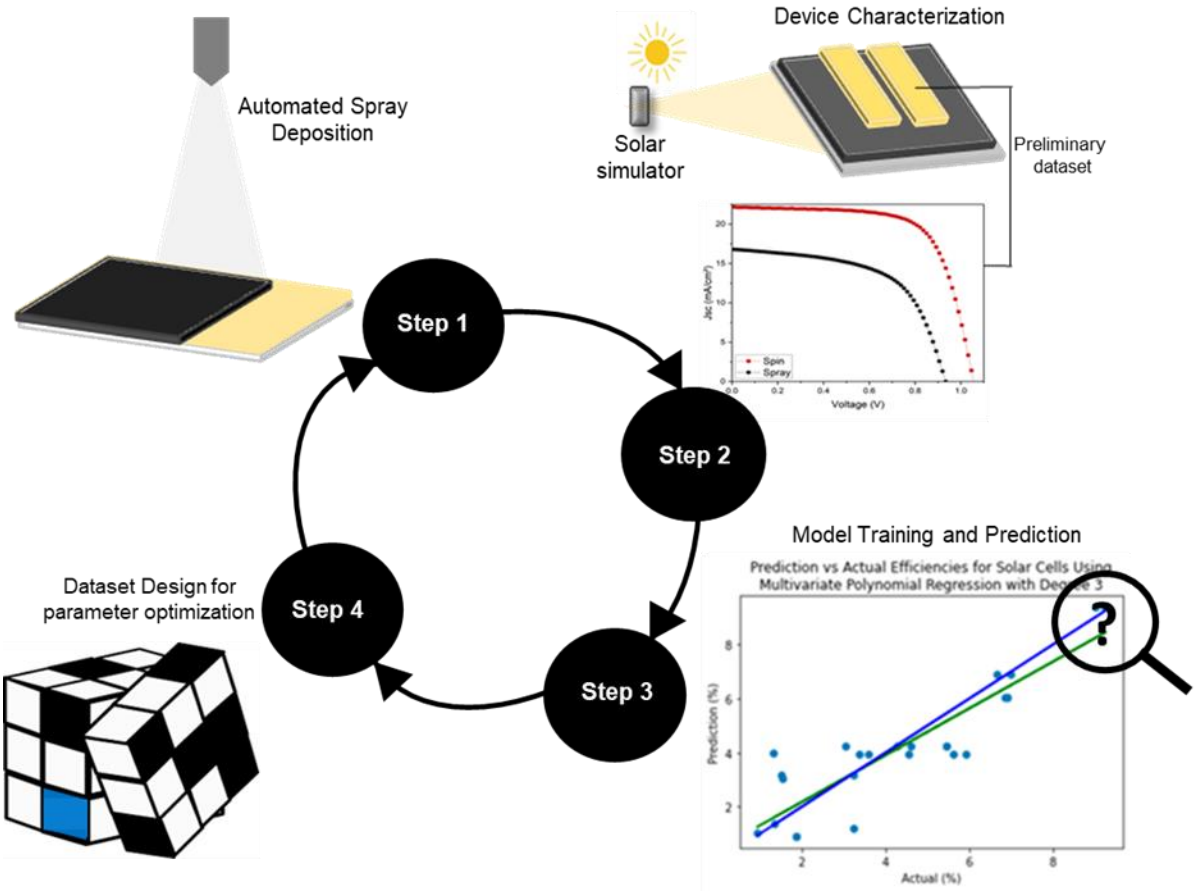


Figure 6-1. The framework for spray processed perovskite optimization

## 6.2 Theory

### 6.2.1 Regression Models

There are many choices for ML regression modeling and there is no algorithm that is suitable for every problem and every dataset [10]. Here, we compare different regression algorithms on spray-coated perovskites as an absorber in perovskite solar cells, including multivariate linear and polynomial regression.

*Linear Regression*

One-dimensional linear regression is the most commonly analysis method for predicting relationship between a quantitative variable outcome and a quantitative explanatory variable [14]. The linear relationship is shown as

$$y_i = \beta_0 + \beta_1 x_i + \epsilon_i \quad (6.1)$$

In Equation 6.1, $\beta_0$ and $\beta_1$ are two unknown constants representing the intercept and slope in linear model, and $\epsilon_i$ is the error term. For this study, we use a powerful version of the basic one-dimensional linear regression model called multiple linear regression model as we have four selected variables in spray processing to predict the resulted device efficiencies. Instead of fitting separated simple linear regression models, multiple linear regression can be used to directly accommodate multiple predictors. Equation 6.2 describes the form of the typical multiple linear regression model [15,16].

$$y_i = \beta_0 + \beta_1 x_1 + \beta_2 x_2 + \cdots + \beta_i x_i + \epsilon_i \quad (6.2)$$

where y is the dependent variable and $X_1$ and $X_2 \ldots X_n$ are the independent variables. Once fitted, the coefficients for the individual variables can be extracted and used as an indication of the importance of individual variables.

*Polynomial Regression*

Simple linear regression is suitable for fitting straight-line trends. However, for more general trends such as quadratics trends, an extended multilinear regression called polynomial regression can add extra predictors by raising each of the original predictors to the power $x_i$, ${x_i}^2, {x_i}^3, \ldots {x_i}^d$, as regressors. Polynomial regression provides a way to identify the non-linear relationship between independent and dependent variables shown in Equation 6.3. Polynomial regression allows to produce a very non-linear curve with large degree, $d$. It is

uncommon to use polynomial regression with $d$ more than 3 or 4, as there is a risk of overfitting the data points and the curve takes a very strange shapes [16].

$$y_i = \beta_o + \beta_1 x_i + \beta_2 {x_i}^2 + \beta_3 {x_i}^3 + \cdots + \beta_d {x_i}^d + \epsilon_i \quad (6.3)$$

*Error Metrics*

To evaluate the quality of the fitted model on the dataset, we need to measure the accuracy of the model prediction that is obtained when we apply our model on the dataset. We use three error metrics to quantify how well a model fits the preliminary dataset, including R-Squared, MSE (mean squared error), and RMSE (root means squared error). MSE is the most common error metrics which produces lower values when the predicted responses are closer to the actual responses. RMSE is the square root of MSE that measures the standard deviation of residuals. The lower MSE and MSE, the better a model fits the dataset. R-squared or coefficient of determination is used to determine the size of the proportion of the variance in the dependent variable which is explained by the regression model. R-Squared of 0 means that the dependent variable cannot be predicted by the independent variable, while R-Squared close to 1 indicates that the model explains the large portion of the variance in the response variables [14,16].

## 6.3 Experimental Section

### 6.3.1 Perovskite Solar Cells

*Device Fabrication*

Mesoscopic architectures of hybrid organic–inorganic perovskite solar cells is used as shown in **Error! Reference source not found.** (a), consisting of FTO/$TiO_2$/Perovskite/SpiroOMeTAD/Au. **Error! Reference source not found.** (b) captures a representative scanning electron microscope (SEM) image of complete PSC device.

Prepatterned FTO-coated glass were sequentially cleaned in Decon-90, deionized water, acetone, and isopropyl alcohol. An electron transporting layer (ETL), compact titanium dioxide ($cTiO_2$), was prepared from the solutions of 0.15 M and 0.3 M titanium diisopropoxide *bis*(acetylacetone) solution (Sigma Aldrich) in *n*-butanol. The 0.15 M solution was spin-coated onto FTO at 2000 rpm for 30 s with annealing at 125 °C for 5 min before spin-costing the 0.3 M solution at 2000 rpm for 30 s. The films were then annealed at 500 °C for 30 min [17,18]. The mesoporous $TiO_2$ ($mTiO_2$) was prepared from titania paste (Sigma Aldrich) dissolved in ethanol (1:5, v/v). It was spin-coated at 4000 rpm for 30 s and sintered in a furnace (Lindberg Blue M, Thermo Fisher Scientific) at 500 °C for 30 min.

To prepare perovskite thin film, two-step sequential deposition technique was used. In step one, a mixture of 599.3 mg $PbI_2$ (> 98.9% purity, Sigma Aldrich) in 1 ml of DMF:DMSO (9.5:0.5 of volume ratio) was spin-coated onto the ETL at 1500 rpm for 30 s and then dried at 70 °C for 1 min before spray-coating the organic components. In step two, Automated ultrasonic spray coating (MTI Corporation, Richmond, CA) is used to spray the organic solution (**Error! Reference source not found.** (c)). The organic solution of formamidium (FA)-rich mixed organic cation precursor was prepared from a mixture of 60 mg FAI, 6 mg of MABr and 6 mg of MACl (All chemicals are purchased in Sigma-Aldrich) in 1 ml of IPA and was fed to the ink chamber. The FTO/$TIO_2$/$PbI_2$ substrate was put on hot plate and heated at desired temperature for 1 min before spraying the FA-rich precursor onto $PbI_2$ film. The details of spray parameters are in Table 6.1. As-prepared film was heated at 130 °C for 25 min to promote complete conversion from $PbI_2$ to FA-rich perovskite crystal.

The hole transporting layer (HTL), SpiroOMeTAD, was spin-coated on the perovskite film at 4000 rpm at 30s. The SpiroOMeTAD solution was prepared by dissolving 72 mg of SpiroOMeTAD was dissolved in 1 ml of chlorobenzene before adding 30 μL of 4-*tert*-butylpyridine (tBP) solution and 35 μL of lithium *bis* (trifluoromethyl sulphony) imide (Li-TFSI) solution (260 mg of Li-TFSI in 1 ml of acetonitrile). Finally, 80 nm thick gold back

contact electrode was thermally evaporated using a thermal evaporator (Edwards E306 A, Easton, PA) under a vacuum pressure of $10^{-6}$ Torr at a deposition rate of 0.1 nm $s^{-1}$.

*Pressure Application*

A full stack perovskite solar cells were subjected to external pressure ranging from 0-10 MPa. This was done using 5848 Instron MicroTester (Instron, Norwood, MA, USA) with cured PDMS anvil layer placed between device and the fixture. PDMS was made using a mixture ratio (10:1) by weight of Sylgard 184 silicon elastomer base and curing agent (Dow Corning Corporation, Midland, MI). The mixture was cured at 65 °C for 2h in a mold. The PDMS anvil was cut into desired dimension based on the size of solar cells. The Instron was set to compress the perovskite solar cells at a displacement rate of -1.0 mm $min^{-1}$ and hold for 10 minutes [19].

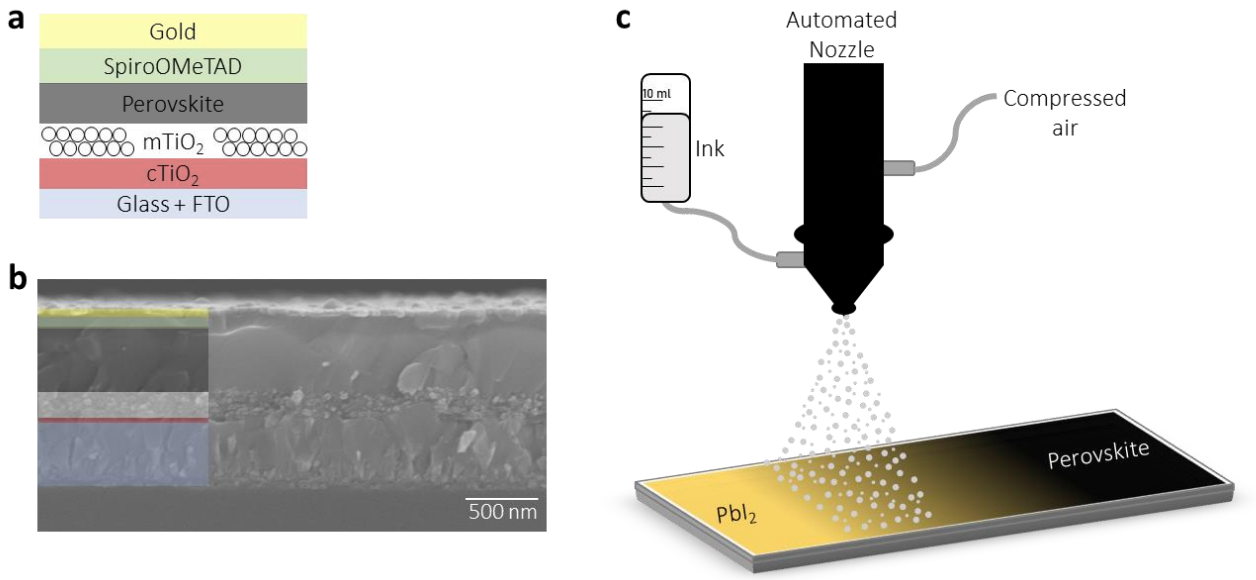


Figure 6-2. (a) The structure of perovskite solar cell used in this study, (b) Representative of SEM image of complete devices (color represents different functional layers in (a), and (c) Schematic of spray processing on perovskite absorber layer

### 6.3.2 Data Collection

Efficiency or PCE, is a key metric in the development of photovoltaic system. PCE obtained from *J-V* characteristic curve was collected as the target variable in this study. The typical J-V curve is shown in **Error! Reference source not found.** (a). This current-voltage (*J-V*) characteristics of PSC were measured using standard solar simulator Keithley SMU 2400 source meter (Keithley Tektronix, Newark, NJ) under AM 1.5G illumination of 90 mW cm $^{-2}$ (Oriel Solar Simulator, Newport Corporation, Irvine, CA). The effective exposed area of the masked cell was 0.125 cm$^2$ with a voltage scan range of -0.4 to 1.2 V. PCE was calculated using Equations (6.4) and (6.5).

$$PCE = \frac{P_{max}}{P_{in}} = \frac{V_{oc}J_{sc}FF}{P_{in}\, x\, active\ area} \tag{6.4}$$

$$FF = \frac{V_{mp}J_{mp}}{V_{oc}J_{sc}} \tag{6.5}$$

$P_{max} = J_{mp}V_{mp}$ is the maximum of output power from solar cell (**Error! Reference source not found.** (b)) [20].

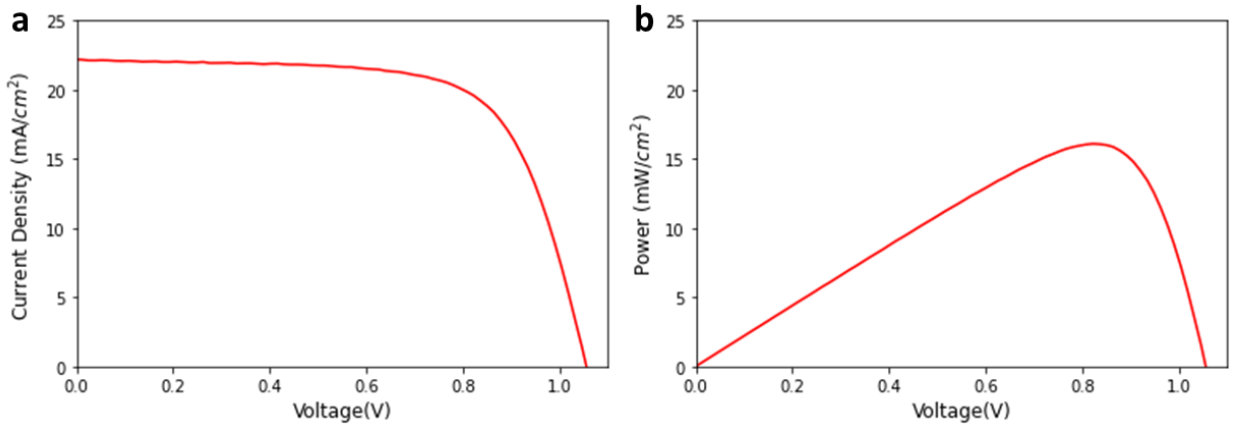


Figure 6-3. (a) Typical J-V characteristic of perovskite solar cell, and (b) the associated maximum power obtained from graph (a)

### 6.3.3 Analyzing the Correlation of Parameters from the Preliminary Dataset

The preliminary dataset consists of 106 devices with experimental process conditions and the solar cell device efficiencies presented in Table S 1 (Appendix). This dataset contains parameters that are considered important in achieving the most efficient perovskite solar cells. All parameter units are standardized before training to ensure that the values lie between the specified range. The selected independent variables are substrate temperature (°C), speed of the spray nozzle (mm/s), height between spray heat to the substrates (mm), and external applied pressure on complete devices (MPa), while the resulted PCE devices (%) is a dependent variable. To analyze the relationship between spray variables and the resulted device efficiency of the preliminary dataset, the distribution of individual variable was visualized through histograms to observe and evaluate the continuity and uniformity of data.

### 6.3.4 Model prediction and Evaluation

In order to guarantee the success of the model, the dataset has to be pre-processed by being split into two subsets, training, and testing sets. In this study, a training set with the size of 0.75 (75%) is used, while the remainder percentage 0.25 (25%) is assigned to the testing data. Two types of regression model, including multivariate linear regression and polynomial regression are used for the prediction of results. The evaluation of the model is then calculated using three error metrics, namely R-Squared, MSE, and RMSE values.

The following systematic approach was chosen to optimize the chosen model. After an iterative script was run to generate all possible distinct combinations of selected variables, the resulted combinations will be fed to the fitted regression model to guarantee that those combinations are accepted by the model. The prediction scores for efficiency will be generated and sorted to find the combinations that predicts the highest efficiency of perovskite solar cells.

### 6.3.5 Generating a Dataset for the *Next-Round* Collection

Ranges of variables in spray processing have been limited based on the resulted perovskite film microstructures investigated in Chapter 5. The details of the variable values are shown in Table 6.1.

Table 6.1 Ranges of process variables for optimization (variable inputs)

| Process Variables | Total Range (Interval) | Total Configurations |
|---|---|---|
| Substrate Temperature | 50-80 (5 °C) | 7 |
| Automated Nozzle Speed | 125-200 (5 mm/s) | 16 |
| Head-substrate distance | 5-8 (1 cm) | 4 |
| Applied Pressure | 0-10 (1 MPa) | 11 |

Based on the total ranges of variable values and its interval in Table 6.1, the total distinct configurations can be up to 4928 different conditions to optimize the conditions of spray-coated perovskite solar cells. Running these exhaustive conditions for experimental executions for only one functional layer in perovskite solar cell structures would incur significant costs both in time and materials. Thus, a script was used to generate a dataset for *next-round* experiments that is equally distributed, unbiased, and encompasses all variable ranges. The ranges of values for each variable were divided into four quadrants representing very low, low, high, and very high quality.

A script iteratively generates each new dataset consisting of random values in the given ranges through each variable and each quadrant. Randomization is a method of experimental control that has been used to prevent the selection bias and the accidental bias [14,21]. Therefore, variables in the new dataset contain 256 (4x4x4x4) district parameters

because the four selected variables are separated into four quadrants. Three subsections will create 81 (3x3x3x3) parameters which would not be enough for experiments, while five subsections will have 625 (5x5x5x5) parameters which would take too long to execute for only one absorber layer in perovskite solar cells. To analyze the relationship between varying spray variables and the resulted device efficiency of the new dataset, the distribution of individual variable was visualized in histograms as done for the preliminary dataset.

## 6.4 Results and Discussion

### 6.4.1 The *First-Round* Statistics

*Trial-and-error* experiments were performed at given parameters to produce a compact perovskite absorber layer that results in high PCE of perovskite solar cells. The optimum perovskite layer via spray coating were observed to have approximately 500 nm of thickness as seen in **Error! Reference source not found.** (b). Based on the *first-round* dataset, Figure 6-4**Error! Reference source not found.** illustrates the variances of individual parameters of spray processing to view the statistical distributions and the count of how frequent they occur in dataset. It clearly shows that the histogram of each variable originally had poor distributions. Temperature data, in **Error! Reference source not found.** (a), encompassed all ranges of temperature, but only concentrated between 50-60 °C and 70-80 °C. This also occurred for speed, distance, and pressure data, where high frequency data was only covered 25% sub-ranges of variables. Therefore, a model built from this imbalanced dataset would be unreliable to predict the remaining *unseen* data.

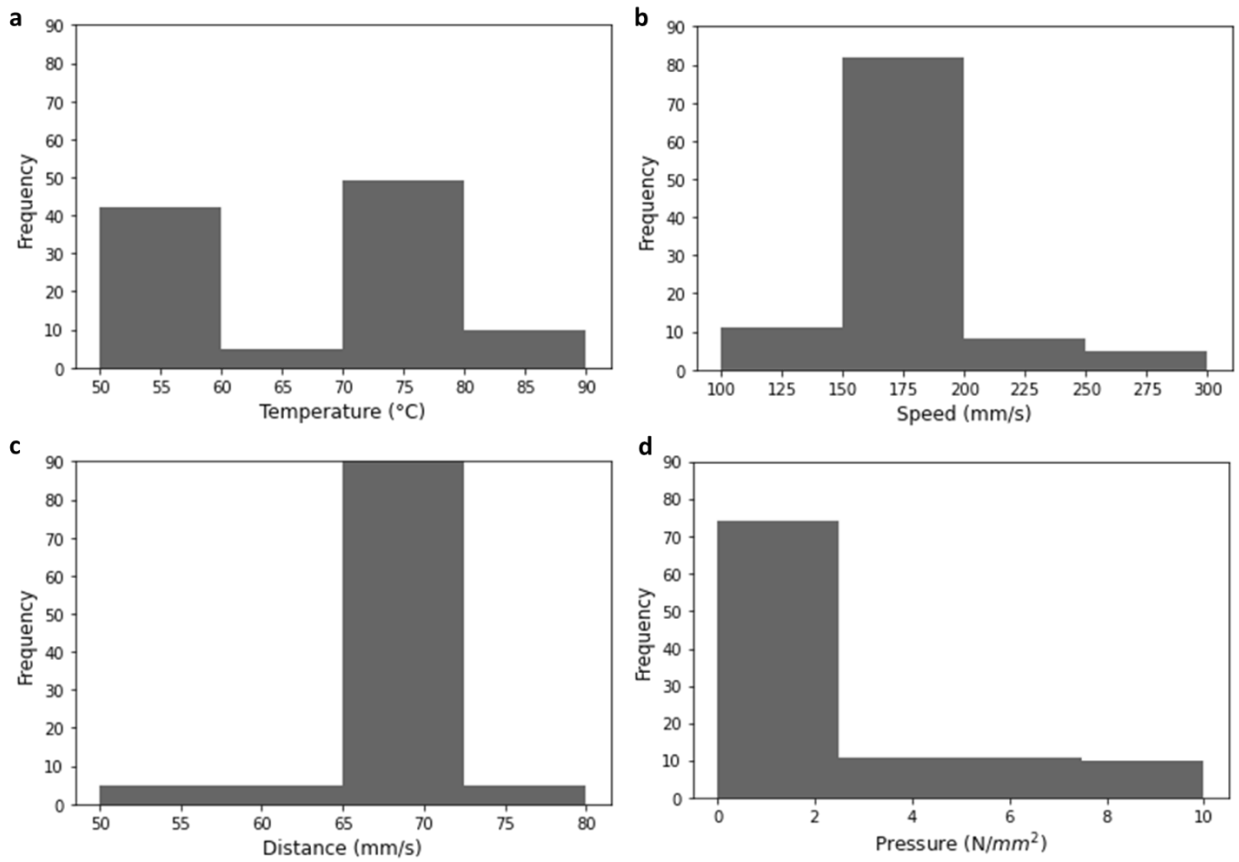


Figure 6-4. Overview of statistics in the *first-round* dataset for (a) temperature, (b) speed, (c) distance, and (d) pressure. The x-axis is the feature in spray processing parameters. The y-axis is the count of the given feature.

The nature of the imbalanced dataset is due to the traditional "one factor at a time" approach that has been used in most prior studies in the process optimization of perovskite solar cells [10], including our own. After varying the substrates temperature, for example, an optimum temperature that produced the compact perovskite structures and high efficiency of PSC devices was used in the *next-round* experiment of varying the automated moving speed of spray head. A single optimum temperature and nozzle speed were then chosen for the rest of values of the variable that was being investigated. This approach resulted in higher frequency in some range of process variables compared to the other ranges. Moreover, some set of experiments with the same configurations were often repeated to make sure the

reproducibility of PSC efficiency values. However, this time-consuming repetitions in the design of experiment also contributed to the imbalanced frequency of the dataset [22]. Therefore, we can conclude that more representative experiments should be performed to fill the missing gaps of variable ranges.

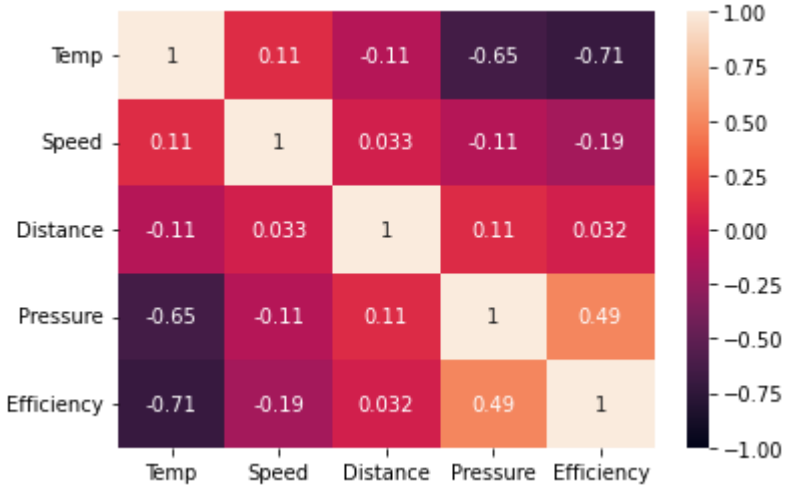


Figure 6-5 The correlation matrix of variables based on the preliminary dataset

Further analysis was carried out using a correlation matrix to analyze the collinearity between independent (x) and dependent variables (y) using the *first-round* experimental dataset. Collinearity means that one variable in the regression model is highly correlated to another feature variable. This causes problems as the trained regression model is not uniquely determined and in turn reduces the interpretation of the regression model [23]. Figure 6-5 depicts the correlation heatmap of the linear one-to-one correlation between variables based on the preliminary collected data that was normalized between -1 and 1. The heatmap shows that substrate temperature and external applied pressure had a strong correlation ($r$) to PCE of -0.71 and 0.49, respectively. This suggests that the PCE of perovskite solar cells increases as the substrate temperature decreases and the applied pressure increases. The automated nozzle speed had a moderate correlation ($r$) with r of -0.19

indicating a slight effect of nozzle spray speed in device's PCE, while the effect of nozzle head-substrate distance was almost negligible. The diagonals were 1 as they represent the correlation between and a variable and itself. It is obvious that the dataset collinearity was impacted by exploratory nature in which data was collected, and it was not necessarily reflective of a true relationship between variables.

### 6.4.2 Model Prediction

*Linear Regression*

Even though the preliminary dataset was imbalanced, it was worth to test the prediction capabilities of the functioned model. Linear regression is the simplest version of regression model used for predicting the results in this study. As four variables were selected for spray-coated PSC optimization, we evaluated the preliminary dataset using the multiple linear regression with the train/test split of 0.75/0.25 out of 106 data points. Figure 6-6 shows the comparison of the measured PCE by experimental versus the predicted PCE by the linear regression. The obtained evaluation metrics are shown in Table 6.2. As mentioned, that R-Squared is preferably lying close to 1; R-squared of 0.58 was obtained from the imbalanced dataset, showing that only 58% of data points were represented by the trained regression line. The data imbalance seen in **Error! Reference source not found.** could cause the model to fit to correlations between independent variables based on the collection process, not the actual data.

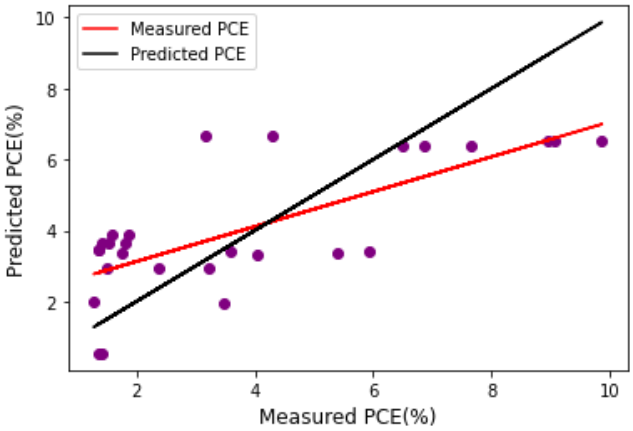


Figure 6-6. Comparison plot of measured vs predicted PCE by linear regression model

Table 6.2 Evaluation metrics for multivariate linear regression

| Evaluation Metrics | Value |
|---|---|
| R-Squared | 0.58 |
| MSE | 3.46 |
| RMSE | 1.86 |
| Standard Deviation | 0.09 |

*Polynomial Regression*

Assuming the dataset has a non-linear data pattern, polynomial regression has also been explored to capture more data points in the dataset. The polynomial functions with different degrees in Figure 6-7 show that the polynomial model tries to fit every datapoint as the polynomial degrees increase. The polynomial model with lower degree is often underfitting the data points, while higher degrees tend to overfit the data points and become an obstacle in achieving best performance of testing data [14,16].

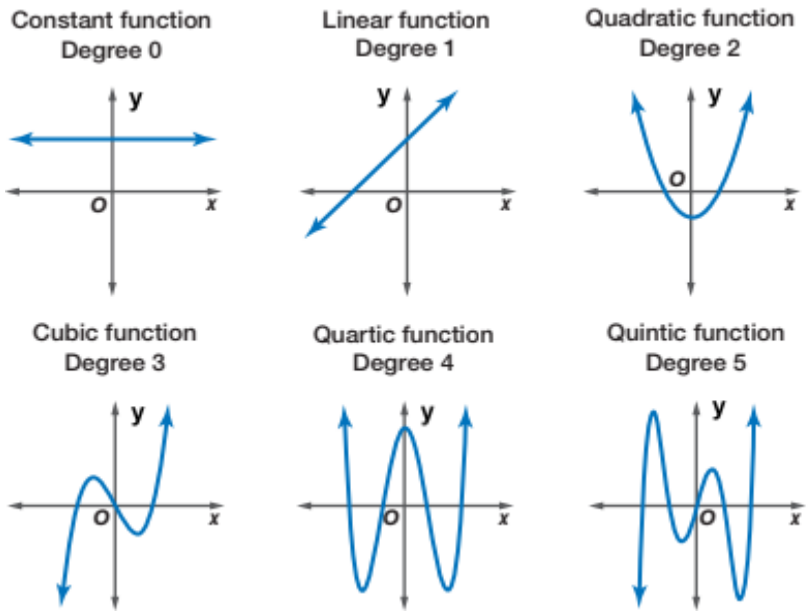

Figure 6-7. Polynomial regression of degrees 0 to 5 [24].

Figure 6-8 displays the comparison of the experimental and predicted PCE using the polynomial regression model. We evaluated error metrics on the trained polynomial regression from degree 1 to 5 and the associated values were tabulated in Table 6.3. Despite the imbalanced nature of the preliminary dataset, the trained polynomial regression model was getting very closed to actual values as the higher degree functions were used. R-Squared of trained polynomials varied from 0.44 to 0.83, while MSE and RMSE values decreased. Third-degree polynomial achieved R-squared of 0.81 and remained flat at the higher degrees. This is a promising result as the model still achieved high accuracy within with the ranges of trained values. However, further evaluation is needed to see if the polynomial functions overfit the dataset.

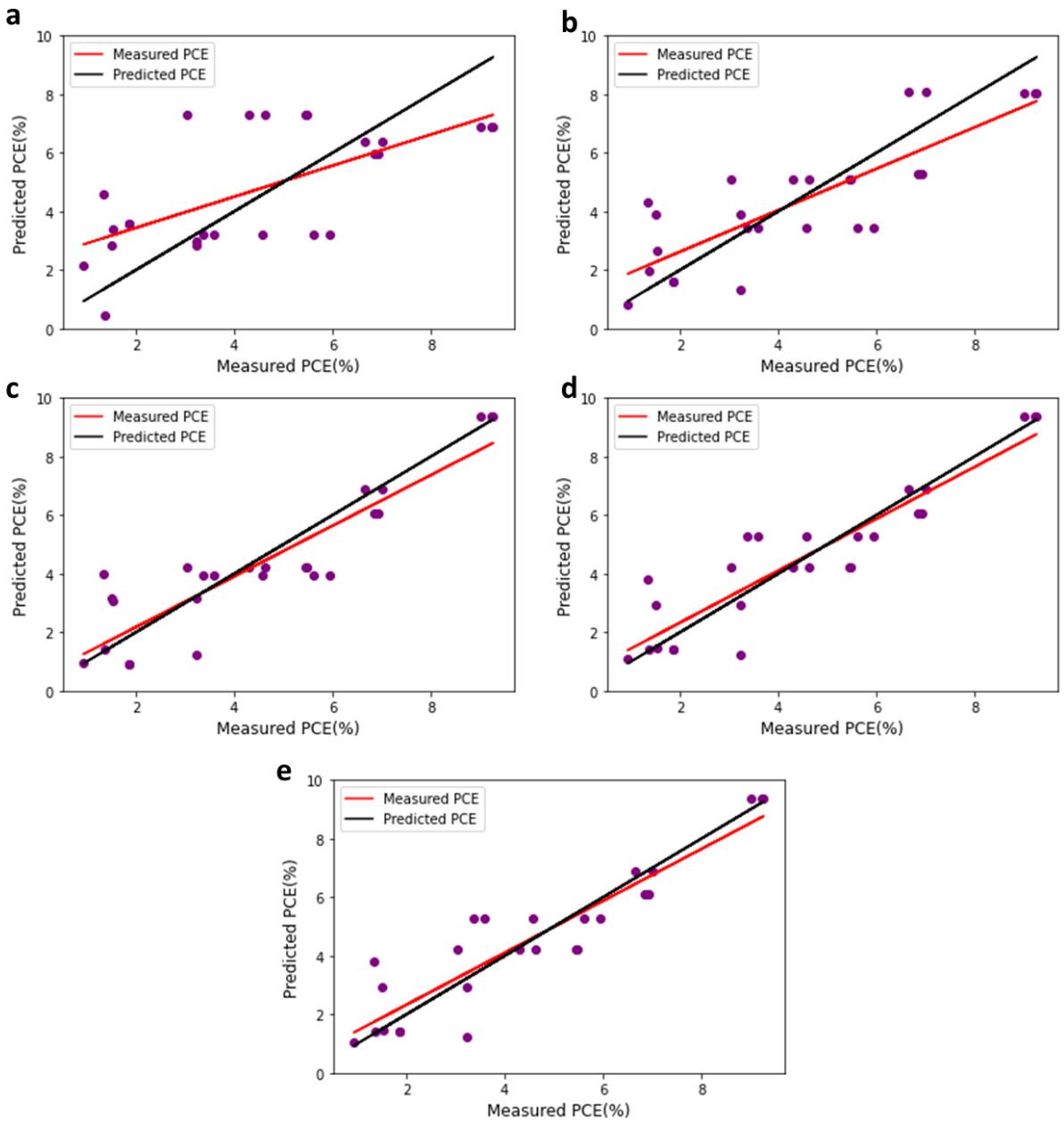


Figure 6-8 Comparison of measured vs predicted PCE by polynomial regression model from degree (a) 1, (b) 2, (c) 3, (d) 4, and (e) 5

Table 6.3 Evaluation metrics and the highest predicted efficiency based on polynomial regression

| Degree | R-Squared Value | MSE | RMSE | Highest Predicted Efficiency (%) |
|---|---|---|---|---|
| 1 | 0.44 | 3.65 | 1.91 | 7.94 |
| 2 | 0.69 | 1.97 | 1.40 | 14.41 |
| 3 | 0.81 | 1.20 | 1.09 | 29.00 |
| 4 | 0.84 | 1.00 | 1.00 | 90.01 |
| 5 | 0.83 | 1.00 | 1.00 | 114.94 |

### 6.4.3 Optimization

*Linear Regression*

To optimize the multiple linear regression model, all 4928 potential parameter combinations based on the selected interval in parameter ranges were plugged to the trained model to see if all combinations are acceptable in the trained model. The model predicts the efficiency of solar devices for all conditions ranging from 2.1 to 7.49 % seen in Figure 6-9. The 20 top-performer of efficiency are depicted in Table S 2 (Appendix). The highest efficiency of perovskite devices based on this model was 7.49% with conditions: temperature of 50 °C, speed of 125 mm/s, distance of 5 cm, and pressure of 10 MPa. It is obviously not a great efficiency, but it is promising because this efficiency can be obtained from an imbalanced dataset. With a balanced dataset, the highest predicted efficiency is expected to be much higher than 7.49%.

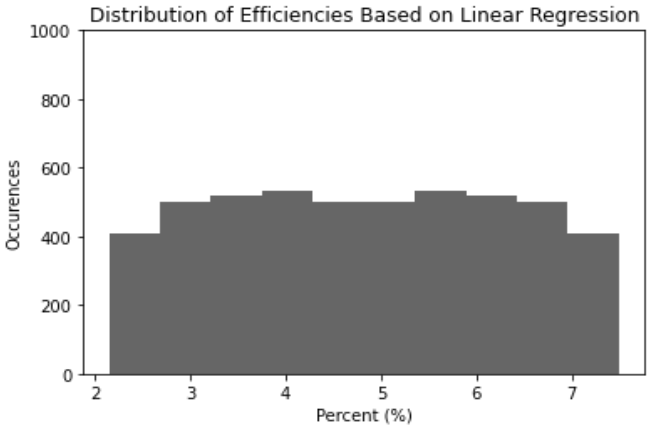

Figure 6-9 Distribution of predicted PCE by linear regression model

*Polynomial Regression*

The same systematic approach was also done for polynomial regression optimization. The predicted efficiency for 20 top-performer by polynomial model with different degree functions are depicted in Table S 3-Table S 6 (Appendix), while the highest value of predicted efficiency is listed in Table 6.3. The error metrics of R-Squared increased as polynomial degrees increasing, and the predicted efficiency has also been improved from 7.94 to 114.94 %. However, the users need to check and ensure that the model was not overfitting on the training set.

Figure 6-10 (a-e) shows the distribution of predicted efficiency of all possible conditions of spray processing based on the polynomial model degree 1 to 5. Slight overfitting was observed in the second-degree polynomial model represented by negative values of efficiency of solar cells were predicted by the model presented in Figure 6-10 (b). Those negative efficiency values were also being predicted for polynomials model with degree 3 to 5 attributed to under representative data in the preliminary collected dataset. Moreover, the overfitting phenomena can also be confirmed by the highest efficiency obtained from the training polynomial model. As the degree gets higher, the predicted efficiency of perovskite solar cells has exceeded beyond the theoretical Shockley-Quisser

limit of ~33% of photoconversion efficiencies for single-junction solar cells [25]. This overfitting obstacles was expected as the result of model inaccuracy caused by the imbalanced collected data which some ranges of independent variable values were under representative. Therefore, a new design of experiment of solar cell is needed to represent the whole search space with a reduced number of experiments to predict the optimal condition of spray-coated PSCs.

After generating prediction scores of efficiencies and sorting the highest predicted efficiency, the results of regression model optimization can be used to further guide a new design of experiments. A reduced number of data points (~50-100) out of 4928 all distinct combinations can be strategically used to predict the optimal conditions that yields high-efficiency perovskite solar devices.

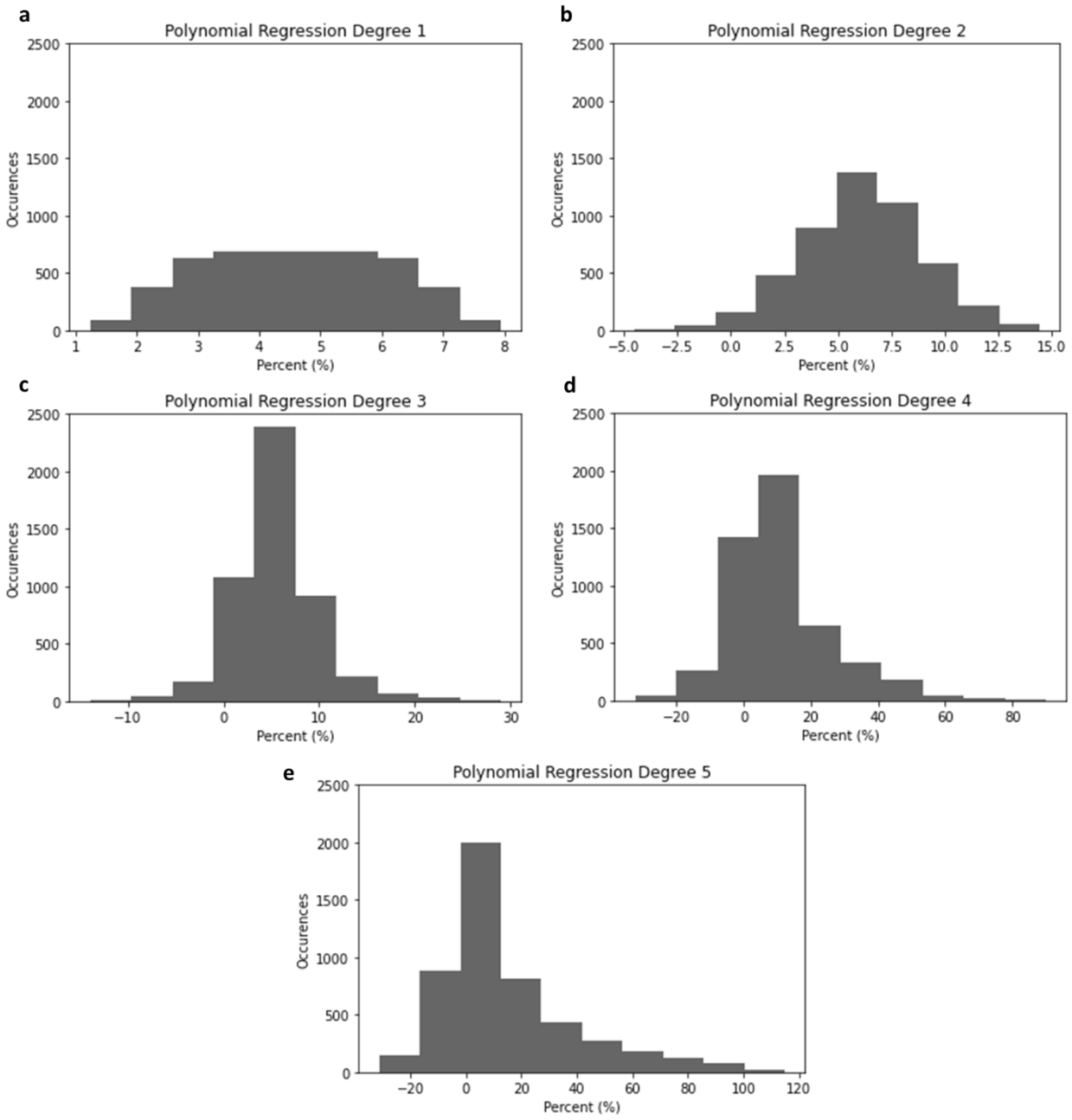


Figure 6-10 Distribution of predicted PCE by polynomial regression model of degree 1 to 5 (a-e).

### 6.4.4 Data Design for *Second-Round* Collection

Machine learning algorithms tend to produce unsatisfactory results when faced with imbalanced datasets, thus a successful ML model really relies on the use of balanced datasets

[12,26]. To improve the performance of perovskite solar cells via spray coating, researchers can strategically design of experiments with new balanced datasets, instead of exploring all 4928 possible parameter conditions of spray processing. The *second-round* dataset for laboratory collection should be balanced and cover a bigger space of parameters to achieve optimum optimization results. In this study, the range of parameter values were further narrowed based on the results from the *first-round* optimization. Table 6.1 shows the details of the selected space and its interval ranges. From 4928 possible conditions, 256 data points were iteratively collected (Table S 7) (Appendix).

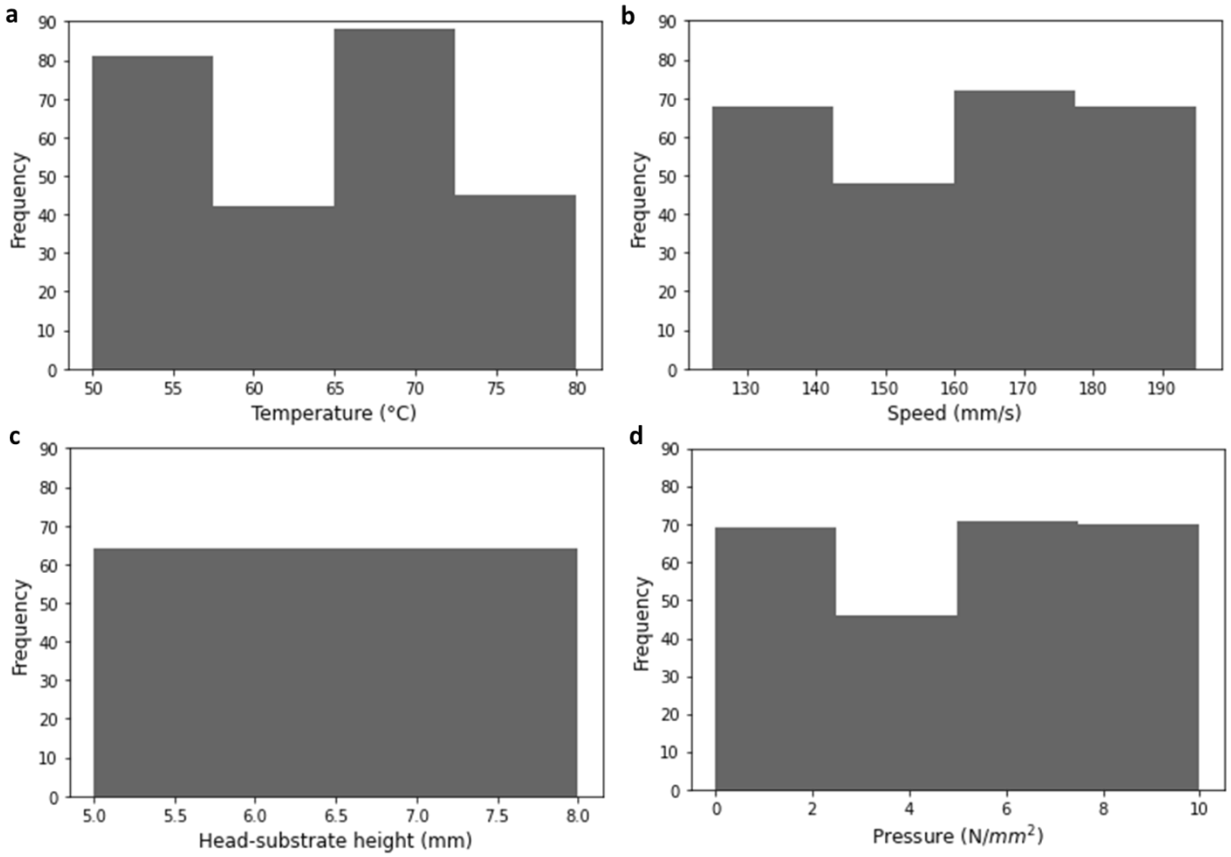


Figure 6-11 Overview of data statistics new dataset for the second-round experiment

Figure 6-11 visualizes the distribution of the new generated dataset. The new dataset optimally encompassed all ranges of parameter combinations and free of user bias. The

imbalanced frequency of the new dataset was still observed due to the nature of the total number of the selected configurations. Total configurations of each independent variables are: 7 for temperature, 16 for automated nozzle speed, 4 for head-substrate height, and 11 for applied external pressure. Substrate temperature, for instance, has 7 configurations and cannot be divided equivalently to 4 quadrants. However, this is not seen as a problem as the new dataset has fully encompassed all space of parameters. Furthermore, the new dataset was also further analyzed using a correlation matrix in Figure 6-12 that is normalized from -1 to 1. This shows that collinearity is very limited as the relationship between variables scale is close to 0. Therefore, this dataset for *second-round* experiments is more representative and expected to yield high accuracy in the interpretation of regression model.

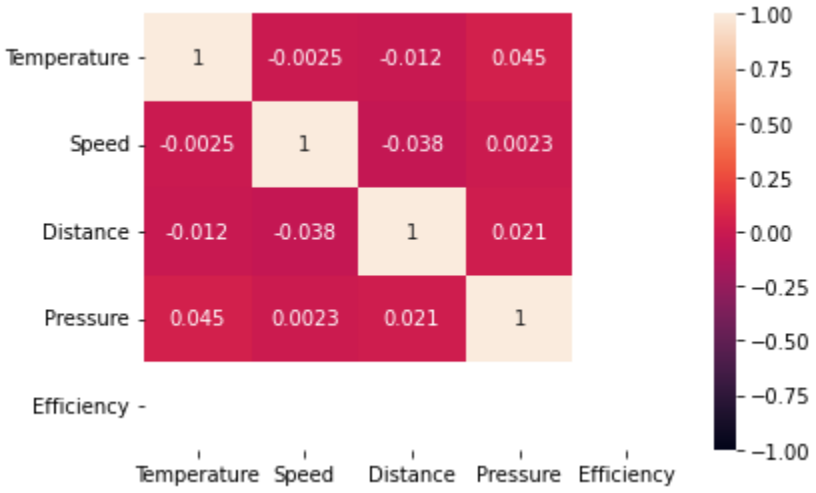


Figure 6-12 The correlation heatmap depicting the linear one-to-one correlation between variable in new dataset for second-round collection

### 4.5 Conclusion and Future Work

Regression models can help to identify the hidden relationships and analyze the impact of variables on the photoconversion efficiency of spray-assisted perovskite solar cells. With

current machine capability to fabricate 16 distinct parameters of PSCs in a day, it takes approximately a year to completely analyze every combination for only a layer of PSCs stack. ML-guided design of experiments (DOE) allows us to collect much reduced experiments that can provides us an accurate model of relationship between parameters and PSCs efficiencies. It leads to a better strategy in optimizing another deposition technique of PSC functional layers. Moreover, future work is needed to complete the work by fabricating new devices based on the new synthetic dataset and compare the predicted efficiency to actual efficiency through experiments.

**References**


[1] Zhang, M.; Xin, D.; Zheng, X.; Chen, Q.; Zhang, W.-H. Toward Greener Solution Processing of Perovskite Solar Cells. *ACS Sustain. Chem. Eng.* **2020**, *8* (35), 13126–13138. https://doi.org/10.1021/acssuschemeng.0c04289.

[2] Zhang, J. X. J.; Hoshino, K. Fundamentals of Nano/Microfabrication and Scale Effect. In *Molecular Sensors and Nanodevices*; Elsevier, 2019; pp 43–111. https://doi.org/10.1016/B978-0-12-814862-4.00002-8.

[3] Bishop, J. E.; Routledge, T. J.; Lidzey, D. G. Advances in Spray-Cast Perovskite Solar Cells. *J. Phys. Chem. Lett.* **2018**, *9* (8), 1977–1984. https://doi.org/10.1021/acs.jpclett.8b00311.

[4] Bishop, J. E.; Smith, J. A.; Lidzey, D. G. Development of Spray-Coated Perovskite Solar Cells. *ACS Appl. Mater. Interfaces* **2020**, *12* (43), 48237–48245. https://doi.org/10.1021/acsami.0c14540.

[5] Wu, W.-Q.; Wang, Q.; Fang, Y.; Shao, Y.; Tang, S.; Deng, Y.; Lu, H.; Liu, Y.; Li, T.; Yang, Z.; Gruverman, A.; Huang, J. Molecular Doping Enabled Scalable Blading of Efficient Hole-Transport-Layer-Free Perovskite Solar Cells. *Nat. Commun.* **2018**, *9* (1), 1625. https://doi.org/10.1038/s41467-018-04028-8.

[6] Whitaker, J. B.; Kim, D. H.; Larson, B. W.; Zhang, F.; Berry, J. J.; van Hest, M. F. A. M.; Zhu, K. Scalable Slot-Die Coating of High Performance Perovskite Solar Cells. *Sustain. Energy Fuels* **2018**, *2* (11), 2442–2449. https://doi.org/10.1039/C8SE00368H.

[7] Li, P.; Liang, C.; Bao, B.; Li, Y.; Hu, X.; Wang, Y.; Zhang, Y.; Li, F.; Shao, G.; Song, Y. Inkjet Manipulated Homogeneous Large Size Perovskite Grains for Efficient and Large-Area Perovskite Solar Cells. *Nano Energy* **2018**, *46*, 203–211. https://doi.org/10.1016/j.nanoen.2018.01.049.

[8] Huang, H.; Shi, J.; Zhu, L.; Li, D.; Luo, Y.; Meng, Q. Two-Step Ultrasonic Spray Deposition of CH3NH3PbI3 for Efficient and Large-Area Perovskite Solar Cell. *Nano Energy* **2016**, *27*, 352–358. https://doi.org/10.1016/j.nanoen.2016.07.026.

[9] Paulson, N. H.; Libera, J. A.; Stan, M. Flame Spray Pyrolysis Optimization via Statistics and Machine Learning. *Mater. Des.* **2020**, *196*, 108972. https://doi.org/10.1016/j.matdes.2020.108972.

[10] Wei, L.; Xu, X.; Gurudayal; Bullock, J.; Ager, J. W. Machine Learning Optimization of P-Type Transparent Conducting Films. *Chem. Mater.* **2019**, *31* (18), 7340–7350. https://doi.org/10.1021/acs.chemmater.9b01953.

[11] Ling, J.; Hutchinson, M.; Antono, E.; Paradiso, S.; Meredig, B. High-Dimensional Materials and Process Optimization Using Data-Driven Experimental Design with Well-Calibrated Uncertainty Estimates. *Integr. Mater. Manuf. Innov.* **2017**, *6* (3), 207–217. https://doi.org/10.1007/s40192-017-0098-z.

[12] Dhankhad, S.; Mohammed, E.; Far, B. Supervised Machine Learning Algorithms for Credit Card Fraudulent Transaction Detection: A Comparative Study. In *2018 IEEE International Conference on Information Reuse and Integration (IRI)*; IEEE, 2018; pp 122–125. https://doi.org/10.1109/IRI.2018.00025.

[13] Zhang, H.; Moon, S. K. Reviews on Machine Learning Approaches for Process Optimization in Noncontact Direct Ink Writing. *ACS Appl. Mater. Interfaces* **2021**, *13* (45), 53323–53345. https://doi.org/10.1021/acsami.1c04544.

[14] Acharya, M. S.; Armaan, A.; Antony, A. S. A Comparison of Regression Models for Prediction of Graduate Admissions. In *2019 International Conference on Computational Intelligence in Data Science (ICCIDS)*; IEEE, 2019; pp 1–5. https://doi.org/10.1109/ICCIDS.2019.8862140.

[15] Bingham, N. H.; Fry, J. M. *Regression*; Springer Undergraduate Mathematics Series; Springer London: London, 2010. https://doi.org/10.1007/978-1-84882-969-5.

[16] James, G.; Witten, D.; Hastie, T.; Tibshirani, R. *An Introduction to Statistical Learning*; Springer Texts in Statistics; Springer New York: New York, NY, 2013; Vol. 103. https://doi.org/10.1007/978-1-4614-7138-7.

[17] Ichwani, R.; Koech, R.; Oyewole, O. K.; Huda, A.; Oyewole, D. O.; Cromwell, J.; Martin,

J. L.; Grimm, R. L.; Soboyejo, W. O. Interfacial Fracture of Hybrid Organic–Inorganic Perovskite Solar Cells. *Extrem. Mech. Lett.* **2022**, *50*, 101515. https://doi.org/10.1016/j.eml.2021.101515.

[18] Oyelade, O. V.; Oyewole, O. K.; Olanrewaju, Y. A.; Ichwani, R.; Koech, R.; Oyewole, D. O.; Adeniji, S. A.; Sanni, D. M.; Cromwell, J.; Ahmed, R. A.; Orisekeh, K.; Anye, V. C.; Soboyejo, W. O. Understanding the Effects of Annealing Temperature on the Mechanical Properties of Layers in FAI-Rich Perovskite Solar Cells. *AIP Adv.* **2022**, *12* (2), 025104. https://doi.org/10.1063/5.0078558.

[19] Oyelade, O. V.; Oyewole, O. K.; Oyewole, D. O.; Adeniji, S. A.; Ichwani, R.; Sanni, D. M.; Soboyejo, W. O. Pressure-Assisted Fabrication of Perovskite Solar Cells. *Sci. Rep.* **2020**, *10* (1), 1–11. https://doi.org/10.1038/s41598-020-64090-5.

[20] Tadeson, G.; Sabat, R. G. Enhancement of the Power Conversion Efficiency of Organic Solar Cells by Surface Patterning of Azobenzene Thin Films. *ACS Omega* **2019**, *4* (26), 21862–21872. https://doi.org/10.1021/acsomega.9b02844.

[21] Suresh, K. An Overview of Randomization Techniques: An Unbiased Assessment of Outcome in Clinical Research. *J. Hum. Reprod. Sci.* **2011**, *4* (1), 8. https://doi.org/10.4103/0974-1208.82352.

[22] Wulff, S. S. A First Course in Design and Analysis of Experiments. *Am. Stat.* **2003**, *57* (1), 66–67. https://doi.org/10.1198/tas.2003.s210.

[23] Tu, Y.-K.; Clerehugh, V.; Gilthorpe, M. S. Collinearity in Linear Regression Is a Serious Problem in Oral Health Research. *Eur. J. Oral Sci.* **2004**, *112* (5), 389–397. https://doi.org/10.1111/j.1600-0722.2004.00160.x.

[24] Jaroslaw, H.; Teixeira-Pinto Armando. *Machine Learning for Biostatistics*; 2021.

[25] Ehrler, B.; Alarcón-Lladó, E.; Tabernig, S. W.; Veeken, T.; Garnett, E. C.; Polman, A. Photovoltaics Reaching for the Shockley–Queisser Limit. *ACS Energy Lett.* **2020**, *5* (9), 3029–3033. https://doi.org/10.1021/acsenergylett.0c01790.

[26] de la Fuente Garcia, S.; Ritchie, C. W.; Luz, S. Artificial Intelligence, Speech, and

Language Processing Approaches to Monitoring Alzheimer's Disease: A Systematic Review. *J. Alzheimer's Dis.* **2020**, *78* (4), 1547–1574. https://doi.org/10.3233/JAD-200888.

# Chapter 7

# Conclusions and Outlook

### 7.1 Summary of key results

This dissertation has been focused on the viability of perovskites as the commercialized solar technology. Perovskite PV technology that is solution-processed material at low temperature holds promise in dramatically reducing cost of solar cell technology compared the previous generation of solar technologies. However, high-efficiency PSCs have not necessarily being paired with viable stability and scalability, limiting the path of this technology towards market commercialization.

Th fundamental interfacial properties such as adhesion and fracture energy are very important to investigate the mechanical integrity of each interface in multilayer stack PSCs. This dissertation investigated that the adhesion of the constituent layers in the multilayer structures are strongly related to the roughness of perovskite surface, processing conditions, as well as series and charge transfer resistances in PSCs. The results of the study inform a design criteria of robust PSCs with a balance between device efficiencies and mechanical reliability of perovskite PV technology. The dissertation also presents that atomic force microscopy technique can be used as a simple approach to understand the interfacial interactions to rank the robustness of interfaces between layers in PSCs. These rankings provide insights in the selection of appropriate functional layers and processing techniques for the PSCs improvement in future.

The dissertation also investigated the robustness of interfaces of PSCs using *Brazilian disk* fracture specimen that can be easily oriented to measure the interfacial fracture toughness over ranges of mode mixities. Towards perovskite PV technology industries that

is applicable to wearable and portable devices, this study is relevant to the stretchable and flexible PSCs, in which there is a need of fracture mechanics approaches to predict failure conditions over ranges of loading conditions. Similar with adhesion, the interfacial fracture energy is also strongly related the condition of perovskite surfaces and its fabrication routes. Kinking in-and-out and crack bridging are considered as the main toughening mechanism in each interface based on the zone model prediction and the underlying specimens characterized by SEM and XPS.

After understanding of fundamental properties of multilayer structures PSCs, this dissertation has focused with the development of scalable and manufacturable spray coating. An optimization towards compact and pinhole free structures of perovskites has been done together with the interfacial properties to establish the connections between scalable technique and the improved charge transfer to the electrodes. The study also continues to learn the effect of pressure application in the photoconversion efficiencies of PSCs. This was attributed to the closure of interfacial defects and compaction of PSCs mesoscopic structures with moderate pressure of 7 MPa.

Finally, this dissertation introduces the use of machine learning (ML) approach to leverage the understanding between high-dimensional variables of spray systems and the perovskite solar cells performances. ML-model help to identify the hidden relationship and analyze the impact on the photoconversion efficiency of perovskite solar cells via spray coating of functional parameters such as substrate temperature, nozzle moving speed, spray distance, and pressure added on spray-assisted PSCs. This study provides a ML-guided design of experiment (DOE) with balanced data design and no repetitions as an effort to exceed the obtained PSCs performances, leading to a better strategy in optimizing not only perovskite fabrication, but also the processing of other functional layers in PSCs.

### 7.2 Future Work for PSCs

Future works can be done in several ways:

1. First, efforts in enhancing the fracture energy at interfaces of PSCs multilayers structures can be done based on the resulted rank of adhesion and fracture energy. This enhancement can be achieved in a sense of gluing one interfaces to other interfaces by adding interfacial layers, scaffolding, adding additives, providing molecular glues at interfaces.
2. Since this dissertation is limited to the design of experiment (DOE) of spray-assisted PSCs, in the future it will be interesting to the see an effort moving forward to the realization of this ML-guided DOE to the real experiments. The study would prove whether ML-guided design is successfully applicable in PSCs optimization as the lifetime of perovskites absorbers are strongly affected by the integral effects of environmental factors such as humidity, light, bias, temperature that is very hard to be quantified in different seasons.
3. Another approach of machine learning technique, such as computer vision, can also be integrated in the spray-assisted perovskite PSCs. To fully exploit the potentials of perovskite PV technology, identifying and classifying the present structural deformations in the spray-assisted PSCs could leverage our understanding towards the correlation between defects and device performances. We have initiated a convolutional neural network (CNN) model (Figure 7-1) which enable us to identify and classify the deformations within the PSCs structures though cross-sectional SEM images. This identification of multi-types of defects in PSCs structures can be incorporated as an intermediary step into regression model to further guide us in designing the experiments. Therefore, this effort will ultimately lead us to increase the robustness and the performances of PSCs at the same time.

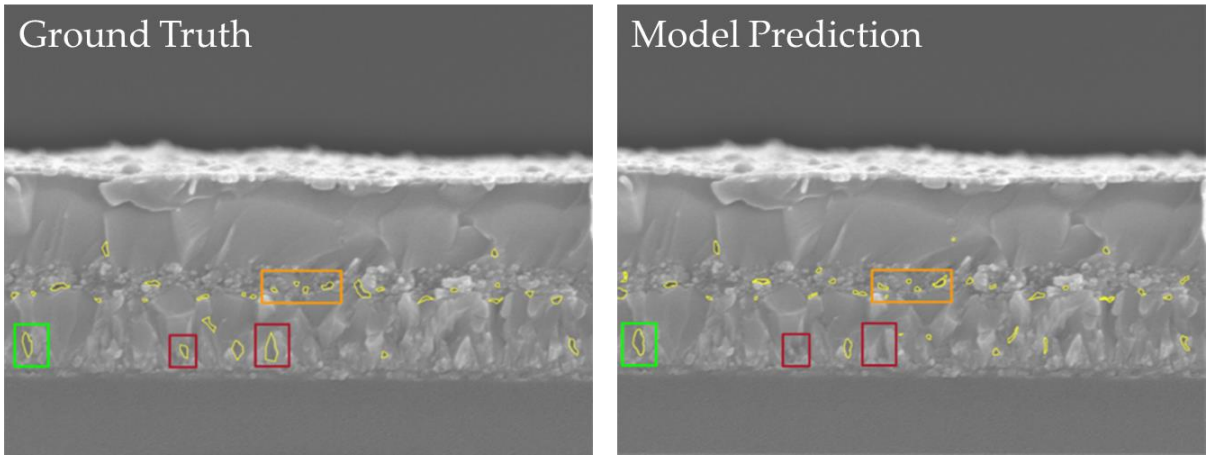


Figure 7-1 The comparison of the multi-deformation detections in the cross-sectional SEM images annotated by human (ground truth, left) and CNN model prediction (right)

# Appendix

Table S 1 All experimental condition and the resulted efficiency of perovskite solar cells

| Devices | Substrate Temperature (°C) | Speed (mm/s) | Head-substrate distance (cm) | Pressure (MPa) | Efficiency (%) |
|---|---|---|---|---|---|
| 1 | 70 | 100 | 7 | 0 | 1.34 |
| 2 | 70 | 100 | 7 | 0 | 1.8 |
| 3 | 70 | 100 | 7 | 0 | 1.86 |
| 4 | 70 | 100 | 7 | 0 | 1.58 |
| 5 | 70 | 100 | 7 | 0 | 1.01 |
| 6 | 70 | 100 | 7 | 0 | 1.86 |
| 7 | 70 | 125 | 7 | 0 | 1.54 |
| 8 | 70 | 125 | 7 | 0 | 1.82 |
| 9 | 70 | 125 | 7 | 0 | 1.43 |
| 10 | 70 | 125 | 7 | 0 | 1.09 |
| 11 | 70 | 125 | 7 | 0 | 1.54 |
| 12 | 70 | 150 | 7 | 0 | 5.28 |
| 13 | 70 | 150 | 7 | 0 | 5.43 |
| 14 | 70 | 150 | 7 | 0 | 5.93 |
| 15 | 70 | 150 | 7 | 0 | 5.61 |
| 16 | 70 | 150 | 7 | 0 | 5.45 |
| 17 | 70 | 150 | 7 | 0 | 3.59 |
| 18 | 70 | 150 | 7 | 0 | 5.34 |
| 19 | 70 | 150 | 7 | 0 | 4.83 |
| 20 | 70 | 150 | 7 | 0 | 3.37 |
| 21 | 70 | 150 | 7 | 0 | 4.56 |

| | | | | | |
|---|---|---|---|---|---|
| 22 | 70 | 200 | 7 | 0 | 3.76 |
| 23 | 70 | 200 | 7 | 0 | 2.37 |
| 24 | 70 | 200 | 7 | 0 | 2.09 |
| 25 | 70 | 200 | 7 | 0 | 1.51 |
| 26 | 70 | 200 | 7 | 0 | 1.38 |
| 27 | 70 | 200 | 7 | 0 | 3.23 |
| 28 | 70 | 200 | 7 | 0 | 4.20 |
| 29 | 70 | 200 | 7 | 0 | 3.89 |
| 30 | 70 | 300 | 7 | 0 | 0.93 |
| 31 | 70 | 300 | 7 | 0 | 0.58 |
| 32 | 70 | 300 | 7 | 0 | 1.03 |
| 33 | 70 | 300 | 7 | 0 | 1.31 |
| 34 | 70 | 300 | 7 | 0 | 1.28 |
| 35 | 50 | 150 | 7 | 0 | 6.00 |
| 36 | 50 | 150 | 7 | 0 | 4.94 |
| 37 | 50 | 150 | 7 | 0 | 6.11 |
| 38 | 50 | 150 | 7 | 0 | 6.85 |
| 39 | 50 | 150 | 7 | 0 | 5.24 |
| 40 | 50 | 150 | 7 | 0 | 6.70 |
| 41 | 50 | 150 | 7 | 0 | 6.71 |
| 42 | 50 | 150 | 7 | 0 | 6.92 |
| 43 | 50 | 150 | 7 | 0 | 6.90 |
| 44 | 50 | 150 | 7 | 0 | 6.91 |
| 45 | 50 | 150 | 7 | 3 | 6.90 |
| 46 | 50 | 150 | 7 | 3 | 7.66 |
| 47 | 50 | 150 | 7 | 3 | 7.69 |

| | | | | | |
|---|---|---|---|---|---|
| 48 | 50 | 150 | 7 | 3 | 6.65 |
| 49 | 50 | 150 | 7 | 3 | 7.15 |
| 50 | 50 | 150 | 7 | 3 | 6.44 |
| 51 | 50 | 150 | 7 | 3 | 6.30 |
| 52 | 50 | 150 | 7 | 3 | 6.48 |
| 53 | 50 | 150 | 7 | 3 | 6.50 |
| 54 | 50 | 150 | 7 | 3 | 7.00 |
| 55 | 50 | 150 | 7 | 3 | 6.87 |
| 56 | 60 | 150 | 7 | 0 | 5.62 |
| 57 | 60 | 150 | 7 | 0 | 1.24 |
| 58 | 60 | 150 | 7 | 0 | 5.57 |
| 59 | 60 | 150 | 7 | 0 | 2.88 |
| 60 | 60 | 150 | 7 | 0 | 1.33 |
| 61 | 80 | 150 | 7 | 0 | 3.47 |
| 62 | 80 | 150 | 7 | 0 | 3.02 |
| 63 | 80 | 150 | 7 | 0 | 3.48 |
| 64 | 80 | 150 | 7 | 0 | 2.81 |
| 65 | 80 | 150 | 7 | 0 | 5.35 |
| 66 | 90 | 150 | 7 | 0 | 1.56 |
| 67 | 90 | 150 | 7 | 0 | 1.41 |
| 68 | 90 | 150 | 7 | 0 | 1.01 |
| 69 | 90 | 150 | 7 | 0 | 1.36 |
| 70 | 90 | 150 | 7 | 0 | 1.73 |
| 71 | 50 | 150 | 7 | 7 | 9.61 |
| 72 | 50 | 150 | 7 | 7 | 9.27 |
| 73 | 50 | 150 | 7 | 7 | 9.31 |

| | | | | | |
|---|---|---|---|---|---|
| 74 | 50 | 150 | 7 | 7 | 9.07 |
| 75 | 50 | 150 | 7 | 7 | 9.01 |
| 76 | 50 | 150 | 7 | 7 | 8.96 |
| 77 | 50 | 150 | 7 | 7 | 9.86 |
| 78 | 50 | 150 | 7 | 7 | 9.73 |
| 79 | 50 | 150 | 7 | 7 | 9.66 |
| 80 | 50 | 150 | 7 | 7 | 8.84 |
| 81 | 50 | 150 | 7 | 7 | 9.23 |
| 82 | 50 | 150 | 7 | 10 | 5.47 |
| 83 | 50 | 150 | 7 | 10 | 3.05 |
| 84 | 50 | 150 | 7 | 10 | 3.24 |
| 85 | 50 | 150 | 7 | 10 | 3.16 |
| 86 | 50 | 150 | 7 | 10 | 4.29 |
| 87 | 50 | 150 | 7 | 10 | 5.46 |
| 88 | 50 | 150 | 7 | 10 | 4.94 |
| 89 | 50 | 150 | 7 | 10 | 5.07 |
| 90 | 50 | 150 | 7 | 10 | 4.8 |
| 91 | 50 | 150 | 7 | 10 | 4.62 |
| 92 | 70 | 150 | 5 | 0 | 4.03 |
| 93 | 70 | 150 | 5 | 0 | 3.67 |
| 94 | 70 | 150 | 5 | 0 | 0.73 |
| 95 | 70 | 150 | 5 | 0 | 1.73 |
| 96 | 70 | 150 | 5 | 0 | 4.17 |
| 97 | 70 | 150 | 6 | 0 | 7 |
| 98 | 70 | 150 | 6 | 0 | 2.87 |
| 99 | 70 | 150 | 6 | 0 | 5.4 |

| | | | | | |
|---|---|---|---|---|---|
| 100 | 70 | 150 | 6 | 0 | 1.77 |
| 101 | 70 | 150 | 6 | 0 | 1.33 |
| 102 | 70 | 150 | 8 | 0 | 1.36 |
| 103 | 70 | 150 | 8 | 0 | 3.23 |
| 104 | 70 | 150 | 8 | 0 | 1.13 |
| 105 | 70 | 150 | 8 | 0 | 1.04 |
| 106 | 70 | 150 | 8 | 0 | 1.37 |

Table S 2 The listing of top 20 parameter combinations by linear regression

```
Top 20 Combinations of Paramaters
Order is as follows:
Efficiency,              Temperature, Speed, Distance, Pressure
-----------------------------------
7.493074274855996        [ 50. 125.   5.  10.]
7.481879240759877        [ 50. 125.   6.  10.]
7.470684206663758        [ 50. 125.   7.  10.]
7.464394273991413        [ 50. 125.   5.   9.]
7.45948917256764         [ 50. 125.   8.  10.]
7.453199239895294        [ 50. 125.   6.   9.]
7.450540463497465        [ 50. 130.   5.  10.]
7.442004205799176        [ 50. 125.   7.   9.]
7.439345429401346        [ 50. 130.   6.  10.]
7.43571427312683         [ 50. 125.   5.   8.]
7.430809171703057        [ 50. 125.   8.   9.]
7.428150395305227        [ 50. 130.   7.  10.]
7.424519239030712        [ 50. 125.   6.   8.]
7.421860462632882        [ 50. 130.   5.   9.]
7.416955361209109        [ 50. 130.   8.  10.]
7.413324204934593        [ 50. 125.   7.   8.]
7.410665428536763        [ 50. 130.   6.   9.]
7.408006652138933        [ 50. 135.   5.  10.]
7.407034272262248        [ 50. 125.   5.   7.]
7.402129170838474        [ 50. 125.   8.   8.]
```

Table S 3 The listing of top 20 parameter combinations by polynomial regression degree 1

```
Top 20 Combinations of Paramaters
Order is as follows:
Efficiency,              Temperature, Speed, Distance, Pressure
-----------------------------------
7.943466142092187        [ 50. 125.   5.  10.]
7.90739938418361         [ 50. 130.   5.  10.]
7.871332626275033        [ 50. 135.   5.  10.]
7.835265868366457        [ 50. 140.   5.  10.]
7.811749855215397        [ 50. 125.   5.   9.]
7.79919911045788         [ 50. 145.   5.  10.]
7.77568309730682         [ 50. 130.   5.   9.]
7.763132352549303        [ 50. 150.   5.  10.]
7.739616339398244        [ 50. 135.   5.   9.]
7.7270655946407265       [ 50. 155.   5.  10.]
7.709917689182249        [ 50. 125.   6.  10.]
7.703549581489667        [ 50. 140.   5.   9.]
7.69099883673215         [ 50. 160.   5.  10.]
7.680033568338607        [ 50. 125.   5.   8.]
7.673850931273672        [ 50. 130.   6.  10.]
7.66748282358109         [ 50. 145.   5.   9.]
7.654932078823573        [ 50. 165.   5.  10.]
7.6439668104300305       [ 50. 130.   5.   8.]
7.6377841733650955       [ 50. 135.   6.  10.]
7.631416065672513        [ 50. 150.   5.   9.]
```

Table S 4 The listing of top 20 parameter combinations by polynomial regression degree 2

```
Top 20 Combinations of Paramaters
Order is as follows:
Efficiency,              Temperature, Speed, Distance, Pressure
-----------------------------------
14.417319942607785       [ 50. 200.   7.   6.]
14.394703556856436       [ 50. 200.   7.   7.]
14.16702470916748        [ 50. 200.   7.   5.]
14.099175551913413       [ 50. 200.   7.   8.]
13.880720936626853       [ 50. 195.   7.   6.]
13.817751805737382       [ 50. 195.   7.   7.]
13.739956561697662       [ 50. 200.   8.   6.]
13.7177168015676         [ 50. 200.   8.   7.]
13.670778448324663       [ 50. 195.   7.   5.]
13.6438178565355         [ 50. 200.   7.   4.]
13.530735927778744       [ 50. 200.   7.   9.]
13.489284702636064       [ 50. 200.   8.   5.]
13.487376357937679       [ 50. 200.   6.   6.]
13.481871055656244       [ 50. 195.   7.   8.]
13.464383346565038       [ 50. 200.   6.   7.]
13.422565422245883       [ 50. 200.   8.   8.]
13.330785834597885       [ 50. 190.   7.   6.]
13.23745775011866        [ 50. 200.   6.   5.]
13.228895924136404       [ 55. 200.   7.   6.]
13.227463958570299       [ 50. 190.   7.   7.]
```

Table S 5 The listing of top 20 parameter combinations by polynomial regression degree 3

```
Top 20 Combinations of Paramaters
Order is as follows:
Efficiency,              Temperature, Speed, Distance, Pressure
-----------------------------------
29.008102952037934       [ 50. 200.   8.   9.]
28.930014715355355       [ 50. 200.   8.   8.]
28.141701672864002       [ 50. 200.   8.  10.]
28.137414066477206       [ 50. 200.   8.   7.]
26.860278109064367       [ 50. 200.   8.   6.]
26.792022102544735       [ 50. 195.   8.   8.]
26.7049078091806         [ 50. 195.   8.   9.]
26.138700885368323       [ 50. 195.   8.   7.]
25.647380901614866       [ 50. 195.   8.  10.]
25.328583946777982       [ 50. 200.   8.   5.]
24.974921261312247       [ 50. 195.   8.   6.]
24.623521261469534       [ 50. 190.   8.   8.]
24.369866147754284       [ 50. 190.   8.   9.]
24.11081776629912        [ 50. 190.   8.   7.]
23.77230868327908        [ 50. 200.   8.   4.]
23.530660334037478       [ 50. 195.   8.   5.]
23.143133827294537       [ 55. 200.   8.   9.]
23.119875321492458       [ 50. 190.   8.  10.]
23.061732765903983       [ 50. 190.   8.   6.]
23.002097037709973       [ 55. 200.   8.   8.]
```

Table S 6 The listing of top 20 parameter combinations by polynomial regression degree 4

```
Top 20 Combinations of Paramaters
Order is as follows:
Efficiency,              Temperature, Speed, Distance, Pressure
-----------------------------------
90.01411736738442        [ 50. 200.   8.   9.]
89.68262709204413        [ 50. 200.   8.   8.]
89.1490995712403         [ 50. 200.   8.  10.]
88.45591234479983        [ 50. 200.   8.   7.]
86.63452939449289        [ 50. 200.   8.   6.]
84.51830717923309        [ 50. 200.   8.   5.]
82.40634730639033        [ 50. 200.   8.   4.]
80.59702405259401        [ 50. 200.   8.   3.]
79.9577068107981         [ 50. 200.   8.   0.]
79.38798436374626        [ 50. 200.   8.   2.]
79.07614785500775        [ 50. 200.   8.   1.]
77.34283559447954        [ 50. 195.   8.   9.]
77.25037609507302        [ 50. 195.   8.   8.]
76.24687160119745        [ 50. 195.   8.   7.]
76.22976460673328        [ 50. 195.   8.  10.]
74.62608027479914        [ 50. 195.   8.   6.]
72.68103294708914        [ 50. 195.   8.   5.]
70.70403311854136        [ 50. 195.   8.   4.]
69.56008836587952        [ 50. 200.   7.   9.]
69.22887326328365        [ 50. 200.   7.   8.]
```

Table S 7 Random dataset generated from the selected ranges of variables in spray processed perovskite solar cells

| Trial | Substrate Temperature (°C) | Speed (mm/s) | Head-substrate distance (cm) | Pressure (MPa) | Efficiency (%) |
|---|---|---|---|---|---|
| 0 | 55 | 140 | 5 | 1 | 0 |
| 1 | 50 | 145 | 5 | 3 | 0 |
| 2 | 50 | 145 | 5 | 8 | 0 |
| 3 | 55 | 140 | 5 | 9 | 0 |
| 4 | 55 | 135 | 6 | 0 | 0 |
| 5 | 50 | 135 | 6 | 3 | 0 |
| 6 | 55 | 130 | 6 | 7 | 0 |
| 7 | 55 | 135 | 6 | 9 | 0 |
| 8 | 50 | 125 | 7 | 2 | 0 |
| 9 | 50 | 140 | 7 | 4 | 0 |
| 10 | 50 | 125 | 7 | 7 | 0 |
| 11 | 55 | 135 | 7 | 10 | 0 |
| 12 | 55 | 125 | 8 | 0 | 0 |
| 13 | 55 | 130 | 8 | 4 | 0 |
| 14 | 50 | 130 | 8 | 8 | 0 |
| 15 | 55 | 125 | 8 | 9 | 0 |
| 16 | 50 | 145 | 5 | 0 | 0 |
| 17 | 50 | 150 | 5 | 5 | 0 |
| 18 | 55 | 145 | 5 | 5 | 0 |
| 19 | 50 | 150 | 5 | 10 | 0 |

| | | | | | |
|---|---|---|---|---|---|
| 20 | 50 | 155 | 6 | 0 | 0 |
| 21 | 55 | 150 | 6 | 4 | 0 |
| 22 | 55 | 155 | 6 | 7 | 0 |
| 23 | 55 | 160 | 6 | 9 | 0 |
| 24 | 55 | 145 | 7 | 1 | 0 |
| 25 | 55 | 155 | 7 | 5 | 0 |
| 26 | 55 | 150 | 7 | 5 | 0 |
| 27 | 50 | 145 | 7 | 9 | 0 |
| 28 | 50 | 150 | 8 | 2 | 0 |
| 29 | 55 | 155 | 8 | 3 | 0 |
| 30 | 50 | 160 | 8 | 6 | 0 |
| 31 | 50 | 150 | 8 | 9 | 0 |
| 32 | 50 | 180 | 5 | 1 | 0 |
| 33 | 55 | 175 | 5 | 3 | 0 |
| 34 | 55 | 160 | 5 | 6 | 0 |
| 35 | 55 | 170 | 5 | 9 | 0 |
| 36 | 50 | 170 | 6 | 0 | 0 |
| 37 | 50 | 175 | 6 | 3 | 0 |
| 38 | 50 | 165 | 6 | 7 | 0 |
| 39 | 50 | 165 | 6 | 10 | 0 |
| 40 | 50 | 165 | 7 | 2 | 0 |
| 41 | 50 | 175 | 7 | 3 | 0 |
| 42 | 55 | 165 | 7 | 6 | 0 |
| 43 | 50 | 170 | 7 | 9 | 0 |
| 44 | 50 | 165 | 8 | 0 | 0 |
| 45 | 50 | 160 | 8 | 3 | 0 |

| | | | | | |
|---|---|---|---|---|---|
| 46 | 50 | 165 | 8 | 6 | 0 |
| 47 | 50 | 170 | 8 | 9 | 0 |
| 48 | 50 | 195 | 5 | 1 | 0 |
| 49 | 50 | 190 | 5 | 3 | 0 |
| 50 | 50 | 185 | 5 | 8 | 0 |
| 51 | 55 | 190 | 5 | 8 | 0 |
| 52 | 50 | 180 | 6 | 2 | 0 |
| 53 | 50 | 185 | 6 | 4 | 0 |
| 54 | 55 | 195 | 6 | 5 | 0 |
| 55 | 50 | 180 | 6 | 8 | 0 |
| 56 | 50 | 195 | 7 | 2 | 0 |
| 57 | 50 | 180 | 7 | 4 | 0 |
| 58 | 50 | 195 | 7 | 6 | 0 |
| 59 | 55 | 195 | 7 | 9 | 0 |
| 60 | 55 | 180 | 8 | 2 | 0 |
| 61 | 50 | 185 | 8 | 4 | 0 |
| 62 | 50 | 190 | 8 | 6 | 0 |
| 63 | 50 | 180 | 8 | 9 | 0 |
| 64 | 60 | 125 | 5 | 1 | 0 |
| 65 | 60 | 140 | 5 | 4 | 0 |
| 66 | 60 | 125 | 5 | 7 | 0 |
| 67 | 60 | 135 | 5 | 8 | 0 |
| 68 | 65 | 130 | 6 | 0 | 0 |
| 69 | 60 | 130 | 6 | 3 | 0 |
| 70 | 65 | 135 | 6 | 5 | 0 |
| 71 | 60 | 140 | 6 | 10 | 0 |

| | | | | | |
|---|---|---|---|---|---|
| 72 | 65 | 125 | 7 | 1 | 0 |
| 73 | 60 | 135 | 7 | 3 | 0 |
| 74 | 60 | 135 | 7 | 6 | 0 |
| 75 | 60 | 125 | 7 | 8 | 0 |
| 76 | 60 | 135 | 8 | 0 | 0 |
| 77 | 60 | 130 | 8 | 3 | 0 |
| 78 | 65 | 125 | 8 | 6 | 0 |
| 79 | 60 | 135 | 8 | 9 | 0 |
| 80 | 60 | 150 | 5 | 0 | 0 |
| 81 | 60 | 145 | 5 | 4 | 0 |
| 82 | 60 | 140 | 5 | 7 | 0 |
| 83 | 60 | 150 | 5 | 9 | 0 |
| 84 | 60 | 145 | 6 | 0 | 0 |
| 85 | 65 | 145 | 6 | 5 | 0 |
| 86 | 60 | 150 | 6 | 6 | 0 |
| 87 | 60 | 145 | 6 | 8 | 0 |
| 88 | 60 | 140 | 7 | 2 | 0 |
| 89 | 60 | 145 | 7 | 2 | 0 |
| 90 | 60 | 160 | 7 | 6 | 0 |
| 91 | 60 | 145 | 7 | 9 | 0 |
| 92 | 55 | 145 | 8 | 0 | 0 |
| 93 | 60 | 160 | 8 | 4 | 0 |
| 94 | 60 | 145 | 8 | 7 | 0 |
| 95 | 55 | 160 | 8 | 8 | 0 |
| 96 | 55 | 160 | 5 | 1 | 0 |
| 97 | 55 | 170 | 5 | 4 | 0 |

| | | | | | |
|---|---|---|---|---|---|
| 98 | 60 | 175 | 5 | 6 | 0 |
| 99 | 60 | 170 | 5 | 9 | 0 |
| 100 | 65 | 175 | 6 | 1 | 0 |
| 101 | 65 | 165 | 6 | 3 | 0 |
| 102 | 60 | 165 | 6 | 6 | 0 |
| 103 | 55 | 175 | 6 | 9 | 0 |
| 104 | 60 | 165 | 7 | 1 | 0 |
| 105 | 60 | 170 | 7 | 3 | 0 |
| 106 | 55 | 175 | 7 | 5 | 0 |
| 107 | 55 | 165 | 7 | 8 | 0 |
| 108 | 60 | 165 | 8 | 2 | 0 |
| 109 | 60 | 175 | 8 | 3 | 0 |
| 110 | 55 | 175 | 8 | 8 | 0 |
| 111 | 60 | 175 | 8 | 8 | 0 |
| 112 | 60 | 180 | 5 | 0 | 0 |
| 113 | 60 | 185 | 5 | 3 | 0 |
| 114 | 60 | 180 | 5 | 7 | 0 |
| 115 | 65 | 190 | 5 | 8 | 0 |
| 116 | 60 | 185 | 6 | 1 | 0 |
| 117 | 60 | 190 | 6 | 4 | 0 |
| 118 | 55 | 185 | 6 | 5 | 0 |
| 119 | 55 | 180 | 6 | 9 | 0 |
| 120 | 60 | 195 | 7 | 1 | 0 |
| 121 | 55 | 195 | 7 | 2 | 0 |
| 122 | 60 | 190 | 7 | 7 | 0 |
| 123 | 60 | 185 | 7 | 10 | 0 |

| | | | | | |
|---|---|---|---|---|---|
| 124 | 60 | 185 | 8 | 0 | 0 |
| 125 | 60 | 180 | 8 | 3 | 0 |
| 126 | 55 | 180 | 8 | 7 | 0 |
| 127 | 60 | 180 | 8 | 10 | 0 |
| 128 | 65 | 140 | 5 | 0 | 0 |
| 129 | 65 | 130 | 5 | 5 | 0 |
| 130 | 70 | 135 | 5 | 7 | 0 |
| 131 | 65 | 130 | 5 | 9 | 0 |
| 132 | 70 | 135 | 6 | 0 | 0 |
| 133 | 65 | 140 | 6 | 4 | 0 |
| 134 | 70 | 135 | 6 | 6 | 0 |
| 135 | 65 | 125 | 6 | 9 | 0 |
| 136 | 65 | 135 | 7 | 0 | 0 |
| 137 | 70 | 140 | 7 | 3 | 0 |
| 138 | 70 | 135 | 7 | 5 | 0 |
| 139 | 70 | 135 | 7 | 9 | 0 |
| 140 | 70 | 140 | 8 | 0 | 0 |
| 141 | 65 | 130 | 8 | 2 | 0 |
| 142 | 65 | 125 | 8 | 7 | 0 |
| 143 | 65 | 130 | 8 | 9 | 0 |
| 144 | 65 | 150 | 5 | 0 | 0 |
| 145 | 65 | 155 | 5 | 3 | 0 |
| 146 | 65 | 145 | 5 | 5 | 0 |
| 147 | 70 | 150 | 5 | 9 | 0 |
| 148 | 65 | 145 | 6 | 1 | 0 |
| 149 | 65 | 155 | 6 | 3 | 0 |

| | | | | | |
|---|---|---|---|---|---|
| 150 | 65 | 150 | 6 | 7 | 0 |
| 151 | 70 | 150 | 6 | 10 | 0 |
| 152 | 70 | 160 | 7 | 0 | 0 |
| 153 | 70 | 150 | 7 | 3 | 0 |
| 154 | 65 | 145 | 7 | 7 | 0 |
| 155 | 65 | 155 | 7 | 9 | 0 |
| 156 | 65 | 145 | 8 | 2 | 0 |
| 157 | 70 | 150 | 8 | 3 | 0 |
| 158 | 65 | 155 | 8 | 7 | 0 |
| 159 | 70 | 150 | 8 | 8 | 0 |
| 160 | 65 | 165 | 5 | 2 | 0 |
| 161 | 65 | 175 | 5 | 4 | 0 |
| 162 | 65 | 170 | 5 | 6 | 0 |
| 163 | 65 | 160 | 5 | 9 | 0 |
| 164 | 65 | 165 | 6 | 0 | 0 |
| 165 | 65 | 170 | 6 | 5 | 0 |
| 166 | 65 | 170 | 6 | 7 | 0 |
| 167 | 70 | 175 | 6 | 8 | 0 |
| 168 | 65 | 165 | 7 | 2 | 0 |
| 169 | 65 | 165 | 7 | 5 | 0 |
| 170 | 65 | 175 | 7 | 6 | 0 |
| 171 | 70 | 165 | 7 | 10 | 0 |
| 172 | 65 | 170 | 8 | 1 | 0 |
| 173 | 65 | 165 | 8 | 3 | 0 |
| 174 | 65 | 165 | 8 | 6 | 0 |
| 175 | 65 | 175 | 8 | 9 | 0 |

| | | | | | |
|---|---|---|---|---|---|
| 176 | 70 | 185 | 5 | 0 | 0 |
| 177 | 70 | 180 | 5 | 3 | 0 |
| 178 | 70 | 180 | 5 | 8 | 0 |
| 179 | 70 | 185 | 5 | 9 | 0 |
| 180 | 70 | 185 | 6 | 0 | 0 |
| 181 | 70 | 180 | 6 | 5 | 0 |
| 182 | 75 | 185 | 6 | 6 | 0 |
| 183 | 70 | 190 | 6 | 9 | 0 |
| 184 | 75 | 180 | 7 | 2 | 0 |
| 185 | 70 | 190 | 7 | 3 | 0 |
| 186 | 65 | 190 | 7 | 6 | 0 |
| 187 | 70 | 180 | 7 | 10 | 0 |
| 188 | 65 | 195 | 8 | 2 | 0 |
| 189 | 65 | 195 | 8 | 3 | 0 |
| 190 | 65 | 180 | 8 | 5 | 0 |
| 191 | 65 | 190 | 8 | 9 | 0 |
| 192 | 80 | 130 | 5 | 1 | 0 |
| 193 | 70 | 125 | 5 | 4 | 0 |
| 194 | 75 | 125 | 5 | 8 | 0 |
| 195 | 75 | 140 | 5 | 8 | 0 |
| 196 | 70 | 130 | 6 | 0 | 0 |
| 197 | 70 | 125 | 6 | 4 | 0 |
| 198 | 75 | 135 | 6 | 6 | 0 |
| 199 | 75 | 135 | 6 | 8 | 0 |
| 200 | 70 | 140 | 7 | 1 | 0 |
| 201 | 75 | 130 | 7 | 4 | 0 |

| | | | | | |
|---|---|---|---|---|---|
| 202 | 70 | 140 | 7 | 5 | 0 |
| 203 | 75 | 125 | 7 | 9 | 0 |
| 204 | 70 | 125 | 8 | 1 | 0 |
| 205 | 75 | 140 | 8 | 5 | 0 |
| 206 | 70 | 130 | 8 | 6 | 0 |
| 207 | 75 | 125 | 8 | 9 | 0 |
| 208 | 75 | 155 | 5 | 0 | 0 |
| 209 | 75 | 150 | 5 | 4 | 0 |
| 210 | 75 | 155 | 5 | 6 | 0 |
| 211 | 75 | 150 | 5 | 10 | 0 |
| 212 | 75 | 150 | 6 | 2 | 0 |
| 213 | 70 | 145 | 6 | 4 | 0 |
| 214 | 75 | 150 | 6 | 8 | 0 |
| 215 | 70 | 145 | 6 | 10 | 0 |
| 216 | 75 | 145 | 7 | 2 | 0 |
| 217 | 70 | 150 | 7 | 4 | 0 |
| 218 | 75 | 150 | 7 | 7 | 0 |
| 219 | 75 | 140 | 7 | 9 | 0 |
| 220 | 75 | 155 | 8 | 1 | 0 |
| 221 | 75 | 140 | 8 | 5 | 0 |
| 222 | 75 | 145 | 8 | 7 | 0 |
| 223 | 75 | 145 | 8 | 9 | 0 |
| 224 | 75 | 170 | 5 | 1 | 0 |
| 225 | 75 | 165 | 5 | 3 | 0 |
| 226 | 75 | 160 | 5 | 7 | 0 |
| 227 | 80 | 170 | 5 | 8 | 0 |

| | | | | | |
|---|---|---|---|---|---|
| 228 | 75 | 160 | 6 | 0 | 0 |
| 229 | 80 | 180 | 6 | 3 | 0 |
| 230 | 75 | 170 | 6 | 6 | 0 |
| 231 | 70 | 175 | 6 | 9 | 0 |
| 232 | 75 | 175 | 7 | 2 | 0 |
| 233 | 70 | 175 | 7 | 4 | 0 |
| 234 | 75 | 170 | 7 | 7 | 0 |
| 235 | 80 | 175 | 7 | 10 | 0 |
| 236 | 75 | 175 | 8 | 1 | 0 |
| 237 | 75 | 170 | 8 | 3 | 0 |
| 238 | 75 | 175 | 8 | 6 | 0 |
| 239 | 80 | 160 | 8 | 10 | 0 |
| 240 | 75 | 190 | 5 | 0 | 0 |
| 241 | 80 | 195 | 5 | 4 | 0 |
| 242 | 75 | 185 | 5 | 7 | 0 |
| 243 | 80 | 180 | 5 | 9 | 0 |
| 244 | 75 | 180 | 6 | 0 | 0 |
| 245 | 75 | 190 | 6 | 5 | 0 |
| 246 | 75 | 185 | 6 | 6 | 0 |
| 247 | 80 | 185 | 6 | 10 | 0 |
| 248 | 75 | 185 | 7 | 1 | 0 |
| 249 | 70 | 185 | 7 | 4 | 0 |
| 250 | 75 | 190 | 7 | 7 | 0 |
| 251 | 75 | 190 | 7 | 8 | 0 |
| 252 | 70 | 190 | 8 | 0 | 0 |
| 253 | 70 | 185 | 8 | 4 | 0 |

| | | | | | |
|---|---|---|---|---|---|
| 254 | 80 | 195 | 8 | 8 | 0 |
| 255 | 75 | 195 | 8 | 8 | 0 |